PRECISION GEOMETRIC METROLOGY OF REFRACTIVE MICRO-LENSES

by

Neil William Gardner

A dissertation submitted to the faculty of
The University of North Carolina at Charlotte
in partial fulfillment of the requirements
for the degree of Doctor of Philosophy in
Mechanical Engineering

Charlotte, NC

2007

Approved by:

____
Dr. Angela Davies

____
Dr. Matt Davies

____
Dr. Jimmie Miller

____
Dr. James Snyder

____
Dr. Kent Curran

©2007
Neil William Gardner
ALL RIGHTS RESERVED

ABSTRACT

NEIL GARDNER. Precision geometric metrology of refractive micro-lenses.
(Under the direction of DR. ANGELA DAVIES)

The accuracy of interferometric surface form measurements is limited by wavefront errors inherent in interference microscopes. In interferometry, self-calibration refers to separating the interferometer bias from the errors on a test surface. Using a medium grade spherical calibration artifact, the random ball test (RBT) self-calibration technique is useful for isolating systematic wavefront biases to achieve low-uncertainty surface form measurements of the test surface. Theoretical and experimental studies revealed that the calibration result changes with artifact surface quality and misalignment, and the effect worsens when calibrating for micro-optics (radii < 1 mm) measurements. The curvature of the artifact leads to retrace errors, which are aberrations caused by altered ray paths after reflection from the test artifact. A comprehensive optical ray-trace software simulation was developed to model the RBT and explore the calibration dependence to various system parameters. Translational artifact misalignment away from null along the optical axis has a direct effect on the calibration result, even when simulating a perfect spherical artifact. Reducing the artifact alignment from ½ wave to 1/10 wave reduces the required number of measurements by one third. The RBT was tested on a custom interferometer built to test the geometrical properties of refractive micro-lenses. Derivation of a new equation to model the convergence of the test to the rms system wavefront bias was accomplished. Through modeling and testing we were able to confirm the validity of the RBT, recommend an efficient method of implementation and understand the aspects impacting the calibration uncertainty.

DEDICATION

To my family

To the memory of Claude Jackson

To the memory of Vladimir Komarnitsky

To the memory of Gary Bellemare

ACKNOWLEDGEMENTS

I am extremely appreciative of the helpfulness and enthusiasm displayed by my advisor, Angela Davies. Angela, you have had a tremendous influence on advancing my career and I have greatly benefited from our numerous technical discussions. Also, I truly enjoyed working in the UNCC Optics Metrology group, alongside Amit Suratkar, Kate Medicus, Daryl Purcell, Ayman Samara, Brent Bergner, Serenity Dunn, Javaid Ikram and Solomon Gugsa. In addition, I would like to thank the University of North Carolina at Charlotte, the Department of Physics and Optical Science, and the Department of Mechanical Engineering. I am also thankful for the funding provided by the National Science Foundation (grant #0348142). I must acknowledge the DDE programming advice generously offered by Derek Griffith of CSIR and John D'Errico. Thank you also to the members of my committee, Jim Snyder, Jimmie Miller and Matt Davies, for their help and thoughtful advice. Lastly, I am especially grateful to my parents and my brother for their constant support and encouragement, and for their genuine interest in my work. To my everyday partners, Wendy and T.J., I am infinitely thankful for the joy and happiness that you bring to my life. "Whether you think you can or can't, you're right." – *Henry Ford*

TABLE OF CONTENTS

LIST OF FIGURES viii

LIST OF TABLES xiii

LIST OF ABBREVIATIONS xiv

CHAPTER 1: INTRODUCTION 1

CHAPTER 2: SURFACE METROLOGY 10

2.1 Roughness, Waviness and Form 10

2.2 Optical Interference 14

2.3 Twyman-Green Interferometry 16

2.4 Self-Calibration 21

2.5 Aberration Theory 25

CHAPTER 3: CUSTOM INTERFEROMETER 34

3.1 Micro-Optic Reflection and Transmission Interferometer (MORTI) 34

3.2 MORTI Alignment 40

CHAPTER 4: SOFTWARE MODELING 55

4.1 Retrace Error Simulation 55

4.2 Random Ball Test Simulation 59

CHAPTER 5: EXPERIMENTAL SETUP AND RESULTS 84

5.1 Retrace Error Effect on MORTI 84

5.2 Effects of Misalignment on MORTI 92

CHAPTER 6: DISCUSSION 101

CHAPTER 7: CONCLUSIONS 110

REFERENCES 116

APPENDIX 121

LIST OF FIGURES

FIGURE 1: Typical light wave having orthogonal electric and magnetic field components. 2

FIGURE 2: Three-dimensional MEMS optical switch uses a micro-lens array for focusing and collimating optical signals. 3

FIGURE 3: Processing steps for an array of lenses fabricated using proton beam writing and a thermal reflow technique. 4

FIGURE 4: Microscopic image of surface-relief refractive micro-lenses. 5

FIGURE 5: Surface-relief refractive micro-lens with a spherical surface profile. 6

FIGURE 6: Two-sphere test for absolute calibration. 8

FIGURE 7: Setup of a Twyman-Green interferometer. The deviation of the reflected beam in the test arm from a plane wave provides the information on the deviations from the sphericity of the micro-surface. 9

FIGURE 8: Various spatial wavelengths for different surface features. 11

FIGURE 9: Relationship between surface roughness, waviness and form. 12

FIGURE 10: Various measurement tools for different spatial wavelengths. 13

FIGURE 11: Stylus profiling using a coordinate measuring machine. 13

FIGURE 12: (a) Two waves in phase (bottom left) combine and interfere constructively to form a larger resultant wave (top left); (b) two waves out of phase (bottom right) interfere destructively and cancel out (top right). 16

FIGURE 13: Twyman-Green Interferometer used to test a spherical part. 17

FIGURE 14: Phase-shifting waves; by stepping the path length by a number of known phases it is possible to recover the phase of the interference signal. 19

FIGURE 15: The dependence of system resolution on the aperture objective lens. 21

FIGURE 16: Systematic and random errors. 23

FIGURE 17: Wave aberrations result from defects in the components of an optical system. 26

FIGURE 18: First ten Zernike wave aberration patterns. 27

FIGURE 19: Spherical aberration; a perfect lens (top) focuses rays to a single point, but a real lens (bottom) focuses to different points depending on the radial position of each incoming ray. 29

FIGURE 20: Rays existing in meridian and sagittal sections after being refracted by the optical system do not gather in one point due to astigmatism. 30

FIGURE 21: Coma aberration. 30

FIGURE 22: Field curvature. 31

FIGURE 23: Distortion aberration. 31

FIGURE 24: Defocus (power) aberration. 33

FIGURE 25: 4f relay system. 36

FIGURE 26: Actual imaging leg of MORTI. 36

FIGURE 27: Micro-interferometer in Twyman-Green configuration for characterization of micro-lens form errors. 37

FIGURE 28: Resolving power of objective lenses. 39

FIGURE 29: ZEMAX simulation of interferometer test arm showing how the radius of curvature (ROC) of a convex test surface must be smaller than the back focal length of the objective. 39

FIGURE 30: MORTI configuration for alignment procedure. 41

FIGURE 31: Optical flat assembly on microscope stage. 42

FIGURE 32: Sony laser scale for accurate positioning. 43

FIGURE 33: Typical heterodyne interferometer setup. 44

FIGURE 34: BB2 equipped with DMI laser source, optics and fold mirror. 46

FIGURE 35: BB2 and tripod; directs beam to MORTI. 47

FIGURE 36: Calibration curves for Sony laser scale and DMI readings. 48

FIGURE 37: FFMA mirrors; focusing. 49

FIGURE 38: Actual FFMA with reference BS and 45 degree mirrors. 50

FIGURE 39: MORTI test arm with moveable objective lens. 52

FIGURE 40: Imaging system calculations. 52

FIGURE 41: Twyman-Green setup. 53

FIGURE 42: MORTI overview. 54

FIGURE 43: ZEMAX ray trace model of an aberrated interferometer wavefront reflecting from the surface of a perfect micro-sphere with a radius comparable to that of a micro-lens. 57

FIGURE 44: Simulated retrace error data for calibration of an interferometer with a perfect sphere. 58

FIGURE 45: Example of calibration artifact misalignment from the confocal position, where a spherical beam from an objective lens ideally nests into the surface. 61

FIGURE 46: Spheres created by coding and spherical harmonic functions. 62

FIGURE 47: ZEMAX model of test arm of interferometer. 64

FIGURE 48: ZEMAX 3D model of test arm of interferometer. 64

FIGURE 49: ZEMAX data editors for prescribing variables and biases. 65

FIGURE 50: Different techniques for sending sag data to ZEMAX. 67

FIGURE 51: Map showing resulting rms values indicates the sensitivity of the simulation. 68

FIGURE 52: Map showing resulting rms values for a typical random ball test. 69

FIGURE 53: The Gauss function is bell-shaped and centered on $x = 0$; σ is the width, and is defined as the distance from the center of the curve to the point where the curvature changes sign. 70

FIGURE 54: R = 25 mm; plot of rms versus the inverse square root of the number of maps averaged (N). Plot shows resulting rms values converging to the actual system bias for various test conditions in apparent linear fashion. Each data point is the average of ten measurements. The term 'ball' implies 0.18 wv rms form error on ball, '1/2mis' implies misaligning the ball by ½ wave along the optical axis, and '1/10mis' is 1/10 wave of misalignment. 71

FIGURE 55: Chi-square minimization of mean values to the model, plotting rms RBT result versus number of maps averaged, N. The term '1/2wv def' implies misaligning the ball by max ½ wave along the optical axis, '1/10wv def' implies max 1/10 wave misalignment and 'ball' implies 0.18 waves rms surface form on the ball. 76

FIGURE 56: Chi-square minimization to the model for mean values; assuming y is ms and x is 1/N. The term '½ wv def' implies a max ball misalignment of ½ wave along the optical axis, '1/10 wv def' implies max 1/10 wave misalignment and 'ball' implies 0.18 wv rms form error on the ball. 78

FIGURE 57: RBT simulation uncertainty map for an average of 300 maps using a 0.18 wv rms ball form error and 1/10 wv of defocus misalignment. 80

FIGURE 58: Spherical aberration and defocus. 81

FIGURE 59: Plot of spherical aberration versus defocus for a systematic misalignment test for R = 25 mm. 82

FIGURE 60: Plot of the resulting rms versus defocus for alignment sensitivity test of R = 25 mm. 83

FIGURE 61: 440-steel micro-spheres; radii 0.5 – 3 mm. 85

FIGURE 62: Random ball re-orientation fixture. 86

FIGURE 63: He-Ne beam reflecting from the micro-sphere when positioned at the confocal location. 86

FIGURE 64: Fizeau fringes. 87

FIGURE 65: Phase plot obtained during PZT calibration. 88

FIGURE 66: Actual circular fringe pattern from micro-sphere surface. 88

FIGURE 67: Phase I experimental RBT system bias result using 1 mm radius micro-sphere (PV = 361 nm = 0.57 wv). 89

FIGURE 68: Phase I experimental RBT system bias result using a 0.5 mm radius micro-sphere (PV = 553 nm = 0.87 wv). 90

FIGURE 69: Experimental RBT result Zernike generation for R = 1 mm. 90

FIGURE 70: Experimental RBT result Zernike generation for R = 0.5 mm. 91

FIGURE 71: SEM photo of micro-lenses of various ROC. 92

FIGURE 72: Phase II RBT data for MORTI with 0.5 (red points) and 1 mm (blue points) radii balls. 93

FIGURE 73: Phase II RBT experimental result for R = 1 mm on MORTI (PV = 256 nm, rms = 36 nm). 95

FIGURE 74: Phase II RBT result for R = 0.5 mm on MORTI (PV = 431 nm, rms = 113 nm). 96

FIGURE 75. Phase II experimental RBT result Zernike generation for R = 1 mm. 96

FIGURE 76. Phase II experimental RBT result Zernike generation R = 0.5 mm. 97

FIGURE 77. Uncertainty map for R = 0.5 mm on MORTI. 98

FIGURE 78: Actual systematic misalignment on MORTI for 1 mm ball. 99

FIGURE 79: Actual systematic misalignment: defocus versus spherical. 100

FIGURE 80: MORTI repeatability. 104

FIGURE 81: Wyko repeatability. 105

FIGURE 82: Wyko RTI 4100 laser Fizeau interferometer. 105

FIGURE 83: Zygo scanning white light interferometer. 106

FIGURE 84: Zygo Micro-LUPI phase-shifting interferometer. 107

FIGURE 85: Result of an interferometric micro-lens height profile measurement. 111

LIST OF TABLES

TABLE 1: U of A description of Zernike aberrations. 28

TABLE 2: The first nine Zernike polynomials. The normalized pupil radius is ρ, with $0 \leq \rho \leq 1$, θ is the azimuthal angle around the pupil, with $0 \leq \theta \leq 2\pi$, and fitting coefficients a_0 through a_8 are the wavefront errors in units of wavelengths. 32

TABLE 3: Model fit variables compared with actual simulated values; chi square statistic for each case; rms values in waves. The term '½ wv def' implies a max ball misalignment of ½ wave along the optical axis, '1/10 wv def' implies max 1/10 wave misalignment and 'ball' implies 0.18 wv rms form error on the ball. The term 'sim data' refers to a predicted rms value, while 'fit' implies the (actual) resulting rms value following minimization. 77

TABLE 4: Model fit variables compared with experimental variables; chi square statistic for each case; rms values in waves. 94

LIST OF ABBREVIATIONS

OPD – optical path difference

RBT – random ball test

FFMA – focusing fold mirror assembly

MORTI – micro-optic reflection and transmission interferometer

ROC – radius of curvature

CCD – charge-coupled device

MEMS – micro-electro-mechanical systems

BS – beam splitter

BB – breadboard

DMI – distance measuring interferometer

PZT – piezo-electric transducer

OFA – optical flat assembly

NA – numerical aperture

PBS – polarizing beam splitter

PV – peak-to-valley

SWLI – scanning white light interferometer

DDE – dynamic data exchange

rms – root mean squared

CHAPTER 1: INTRODUCTION

Electromagnetic radiation, or light, is defined as a self-propagating wave in space consisting of electric and magnetic field components. Wavelength is the distance between repeating units of the oscillating wave pattern. A lens is a three-dimensional device that forces light to converge or diverge, and is typically formed from a piece of shaped glass. Miniaturization is currently a growing trend and the demand on optical component manufacturers to produce more powerful and smaller lenses with more precise tolerances has fueled the demand for precision non-contact measuring instruments. For continued advancement in precision manufacturing technology, the ability to measure optical components must surpass the ability to fabricate them.

Micro-optics is a term referring to a family of devices consisting of very small lenses that enable the collection, distribution, and modification of light on the micro-scale. These tiny focusing elements, typically 5 µm – 2 mm in diameter with a radii of curvature (ROC) of 0.25 – 2.5 mm, facilitate the imaging, focusing, branching, and transmitting of light waves. Micro-lenses have emerged as essential components in technology sectors such as optical communications, optical storage and display systems, and biomedical instruments [1]. Their ability to 'steer' and shape light depends on a few key parameters such as material homogeneity, and surface form error. Our research focuses on metrology for form error, as this dominates micro-lens performance for refractive components. Among the different types of micro-lenses, surface-relief

refractive lenses have excellent focusing characteristics because of their ideal spherical profiles.

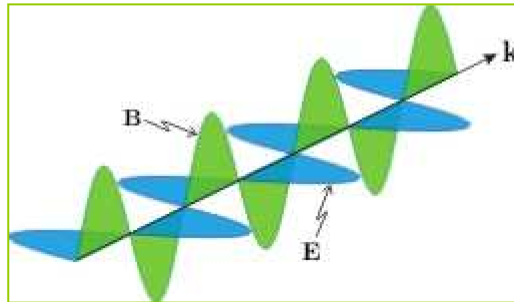

Figure 1. Typical light wave having orthogonal electric and magnetic field components [1].

The applications for micro-lenses are vast and ever-increasing. Micro-lens arrays are used to increase the optical fill factor in CCD (charge-coupled device) sensors and hence improve the sensitivity of the sensors. Sensitivity is defined as the smallest change that can be detected by a device [1]. These lens arrays aid in focusing and concentrating light onto the photodiode surface, thus diverting and collecting light that would otherwise fall on the non-photosensitive regions of the device. CCDs are used in digital cameras, optical scanners and video cameras as light-sensing devices. Micro-lens arrays are also widely used for fiber connectors and switches in optical networking for micro-electro-mechanical systems (MEMS) [2]. The use of micro-lenses is popular in optical storage technology as well, specifically where lens arrays facilitate parallel accessing of multiple tracks in a system. The telecommunications industry, for example, uses lens arrays to couple optical signals with multi-fiber connectors. In optical memory and laser disk systems, a micro-lens is used to focus a laser beam down to a 1 μm-diameter spot, permitting the reading of pulse signals to and from optical disks. Micro-lenses are used in advanced fingerprint sensors for security applications like customs clearance and automobile anti-theft systems. They are currently being used to enhance cell phone

backlighting. Micro-lenses have become an important part of daily life and are in great demand.

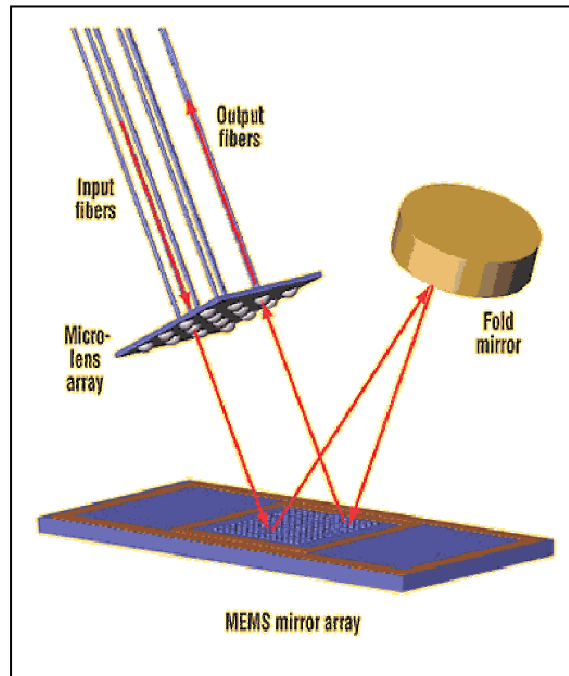

Figure 2. Three-dimensional MEMS optical switch uses a micro-lens array for focusing and collimating optical signals [3].

Refractive micro-lenses are usually fabricated by one of a number of processes, including electron beam lithography, ion exchange, electro-migration, thermal reflow, focused ion beam, chemical vapor deposition, diffusion polymerization, excimer laser irradiation, proton beam writing, and various other techniques originally introduced for fabricating optical fibers and dielectric waveguides [4]. Common micro-lens materials are sol gel glass, gallium phosphide, calcium fluoride, silicon and fused silica. The optimization of micro-lens manufacturing to achieve sub-wavelength form accuracy specifications is a well-known objective of the fabrication industry. Understandably, the measurement of micro-lens surface form errors with sub-micrometer uncertainty creates a

unique and challenging measurement task, especially when monitoring form tolerances on the production floor. However, through detailed investigation, advances in micro-lens form metrology using interferometry can be realized.

1. Expose circles into a resist that is coated on a substrate

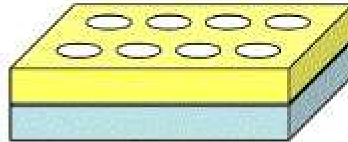

2. Develop the sample leaving behind cylinders of resist

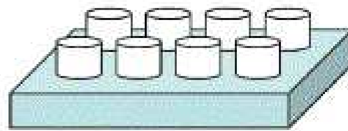

3. Heat the sample above T_g. The resist melts and surface tension forms spherical micro lenses

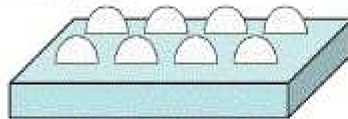

Figure 3. Processing steps for an array of lenses fabricated using proton beam writing and a thermal reflow technique [5].

Surface form error, also known as figure error, is defined as low spatial frequency dimensional error on a part. Form error can be measured both by contact and non-contact methods. Phase-shifting interferometry is a confirmed method for testing optical components and systems, and is widely used for precision surface metrology applications. Phase, is the present position in the cycle of something that changes cyclically, like a wave. A wavefront is an imaginary plane, or surface, of points in space that are reached at the same instant by a wave propagating through a medium (i.e. points with the same phase). In interferometry, two coherent wavefronts propagate one each to

a reference surface and the surface under test. Then interference between the reflected test and reference wavefronts appears as a set of bright and dark fringes and provides information related to surface form errors.

The measurement quality depends on the quality of the interferometer and the reference optic [6]. The resolution and phase contrast are limited by the illumination wavelength of the instrument. The rms (root-mean-square) value is a good single-value description of the overall quality of a wavefront, as it statistically characterizes an entire two-dimensional map. Interferometry is our chosen tool for micro-lens form metrology because one can achieve sub-wavelength measurement accuracy over large surface areas without contacting the part [7]. Contact methods damage the object surface and are time intensive. Our research focuses on using non-contact interferometric metrology to achieve low uncertainty measurements of micro-refractive lens surface form errors.

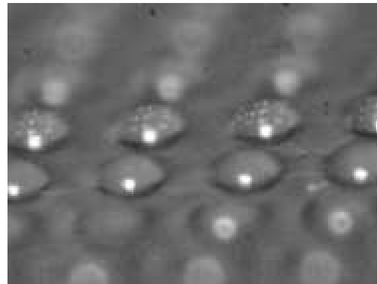

Figure 4. Microscopic image of surface-relief refractive micro-lenses [8].

Previously reserved for quality control in a laboratory environment, phase-shifting interferometry has become a necessary technology for monitoring surface form on the production floor [9]. Manufacturing tolerances for optical components such as cell-phone micro-lenses, require interferometric-level metrology in environments where low-noise testing is not viable. The reproducibility, accuracy, spatial resolution, vertical resolution, speed, and flexibility of this technology have continuously improved to

accommodate the increasing demands of the optical manufacturing industry [10]. Presently, most interferometry is carried out using a laser as the light source. This is primarily because of source brightness and the large temporal coherence. Light waves are correlated, or coherent if they come from the same source and have a narrow bandwidth. With a narrow bandwidth, the coherence length is long and the two interferometer path lengths do not need to be the same optical path length as they would if a short coherence length white light source was used.

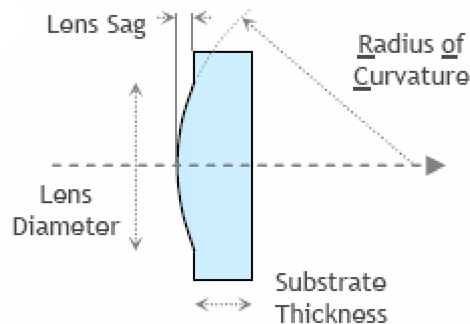

Figure 5. Surface-relief refractive micro-lens with a spherical surface profile.

It is often true in interferometric optical testing that the desired measurement uncertainty is of the same order or larger than the systematic bias of the instrument in question. Interferometric measurements are usually very repeatable, therefore measurement results can be very misleading. When measuring at such a demanding level, often a high-quality calibration artifact is not available to measure or assess the system bias – often the part to be tested is as good or better than any calibration artifact available. In this instance, one must use what are called absolute or self-calibration tests [11]. In recent years, the demand for more accurate surface metrology has increased [12, 13]; consequently much attention has been directed toward methods for calibrating interferometers.

Calibration is a mechanism for creating a controlled, traceable process that meets certification requirements and allows the measurement to be performed with well-defined and quantitative uncertainty. Moreover, instrument calibration on the factory floor in general leads to lower uncertainties and increased system utilization. In interferometry, calibration is dominated by the need to assess the interferometer bias added to each measurement. The bias dominates the measurement (as opposed to random noise or factors contributing to repeatability) and must be removed from measurements to adequately lower measurement uncertainty.

A number of methods have been developed for absolute surface testing, including the N-position, two-sphere, three-flat and random averaging tests. The basic principle is that the reference wave error remains invariant when the part is moved. As a rule, these tests require multiple parts and/or measurements at different positions [14]. For example, the two-sphere method acquires two null confocal measurements with 180º rotations between them, as well as a null point focus (cat's eye) measurement [11]. The reference and test wavefronts can then be uncovered analytically from these data files. The random ball test (RBT) self-calibration technique uses a random averaging approach. It results in a wavefront map of the interferometer bias when measuring spherical parts.

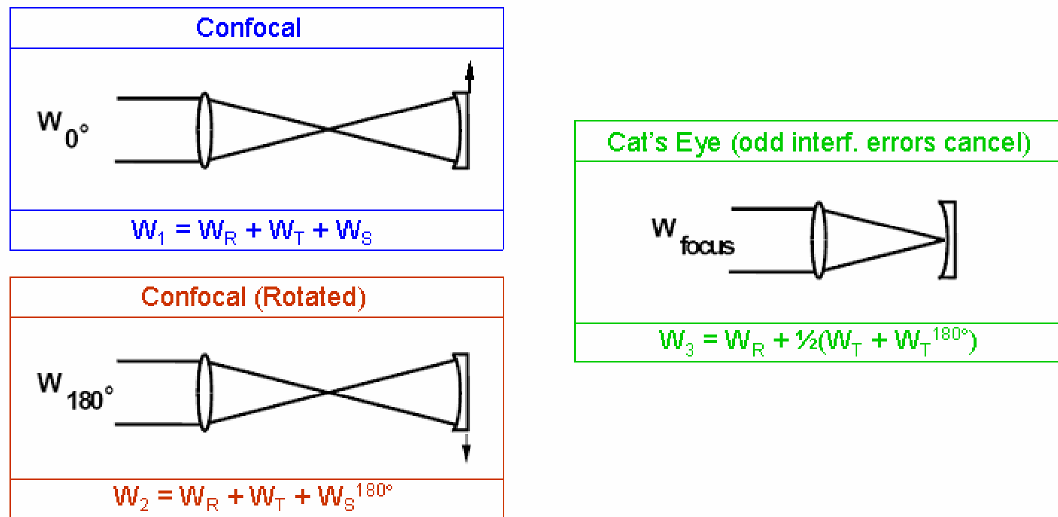

Figure 6. Two-sphere test for absolute calibration [15].

The importance of surface metrology is often neglected and is usually regarded as a necessary evil if at all. In his book *Handbook of Surface and Nanometrology*, D. J. Whitehouse states: "Surface metrology cannot be regarded as an irritant to be added to the general size measurement of a component. The smallness of its magnitude does not infer the smallness of its importance [16]." In keeping with this theme, our hope is to remove as much of the ambiguity related to micro-lens surface metrology as possible. The ultimate research objective is to confirm the validity of the RBT for micro-lens metrology calibration, determine an efficient method for carrying out the test, and understand the aspects impacting calibration uncertainty.

The following sections describe the theory behind interferometry for optical metrology and the RBT, the implementation of the RBT on an in-house micro-interferometer, and the development of a custom ray-trace software simulation to model the RBT. We will compare and contrast our results from simulation and experiment in an effort to reveal the functionality and limitations of this random averaging technique.

Finally, we will summarize the indispensable knowledge gained, namely that calibration artifact curvature and position misalignment greatly affect the interferometer wavefront bias, especially at the micro-optic level.

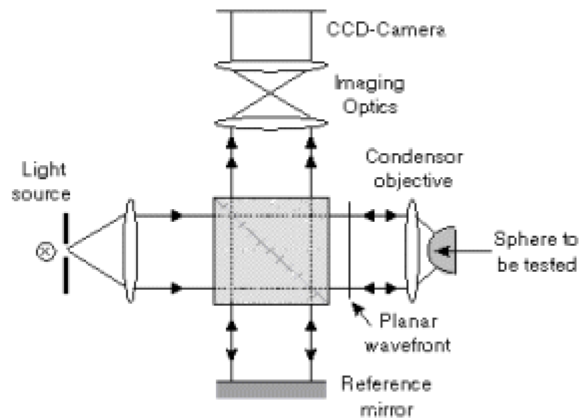

Figure 7. Setup of a Twyman-Green interferometer. The deviation of the reflected beam in the test arm from a plane wave provides the information on the deviations from the sphericity of the micro-surface [17].

CHAPTER 2: SURFACE METROLOGY

2.1 Roughness, Waviness, and Form

Geometric metrology can be defined as the study of surface shape measurements which involves measuring quantities, calibrating instruments, and determining the measurement uncertainty. Generally speaking, calibration implies the act of quantifying the accuracy of a measurement by comparison with a measurement standard. Measurement uncertainty quantitatively represents the confidence in the measured value as an estimate of the true value. All physical measurements should be reported as an estimate of the true value of a measurand plus the uncertainty associated with that estimate.

The performance of a micro-lens is usually characterized by its geometrical properties such as ROC, surface texture, transmitted wavefront and back focal length. Surface texture is particularly interesting due to its wave-like nature and the varying spatial frequency ranges that define it. Spatial frequency is a characteristic that means the property is periodic across position in space. The three main elements of surface texture (or surface errors) are roughness, waviness and form, and they are never found in isolation [18]. In this context, error refers to the difference between the true surface shape and the intended surface shape. Most surface errors are a combination of all three spatial frequencies and it is common to assess them separately. Roughness consists of the highest spatial frequencies and appears as process marks produced by the fabrication

process. The material structure can also play a role in the roughness characteristics. Waviness is the special wavelength range beyond the roughness range. Waviness is typically produced by instabilities in the fabrication process. Form, or form error, refers to the coordinate-specific shape of a surface that differs from the nominal shape or flat line. For refractive plano-convex micro-lenses (i.e. a lens used to focus a parallel beam of light traveling along the lens axis and passing through the lens to a spot on the axis), form error implies deviations from the best-fit sphere for the surface.

In general, form error encompasses long wavelength, low spatial frequency deviations from the ideal surface shape. Form deviations from the desired shape can be the consequence of several factors, including excessive part handling and over-clamping, which introduce stress patterns in the component. Roughness and waviness can limit the accuracy of a form measurement.

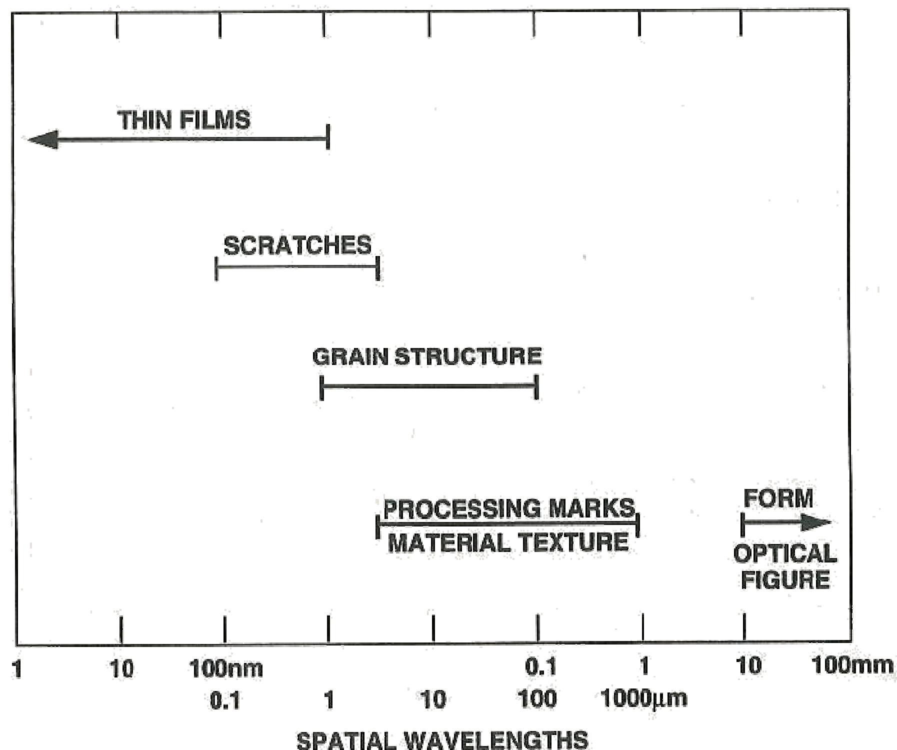

Figure 8. Various spatial wavelengths for different surface features [1].

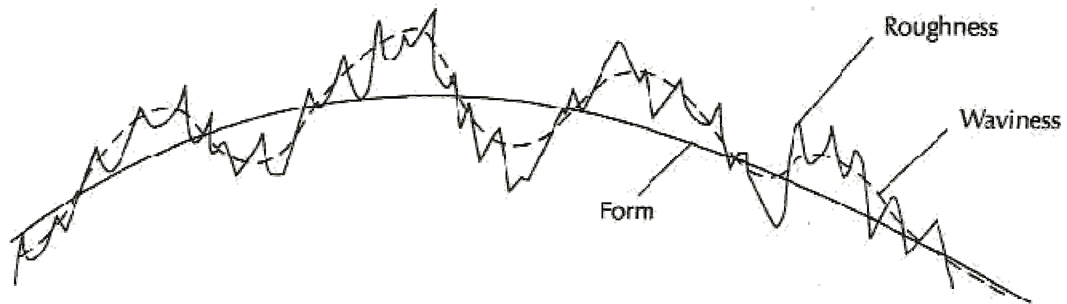

Figure 9. Relationship between surface roughness, waviness and form [19].

Refractive micro-lenses are continuous-relief spherical lenses (i.e. lenses whose surfaces have curvature) with aperture diameters on the scale of 10 μm to small fractions of a millimeter. Details of their dimensional shape strongly influence optical performance. Often, a component may have a sub-micrometer form tolerance, however surface finish might not be critical. Tolerances on low-spatial frequency dimensional surface form error for these lenses are considerably smaller than their largest dimension and often approach tens of nanometers. For that reason, optical metrology (or optical profiling) techniques are preferred to higher-uncertainty and time-consuming contact methods. Optical interference microscopes are commonly used for high-precision surface form analysis for micro-scale components [20]. Interferometry establishes a direct link to the definition of the metre, as the metre is currently defined with respect to laser radiation and is measured by metrologists to one part in 10^{12}.

Even on the shop floor for measurements of micrometer-level features, interferometers are often the instrument of choice because of their high accuracy and ease of use. Their rapid full-aperture measurement capability, ability to contour three-dimensional surfaces, and non-contact measurement nature, are of great interest for practical uses such as process control and quality assurance. Stylus profiling techniques,

like coordinate measuring machines, are the chosen tool in some cases, but have considerable drawbacks, including possible tip damage and part damage upon contacting the part. Scanning microscopes can also be an effective choice, but limitations include lower acquisition speeds and a limited maximum image size.

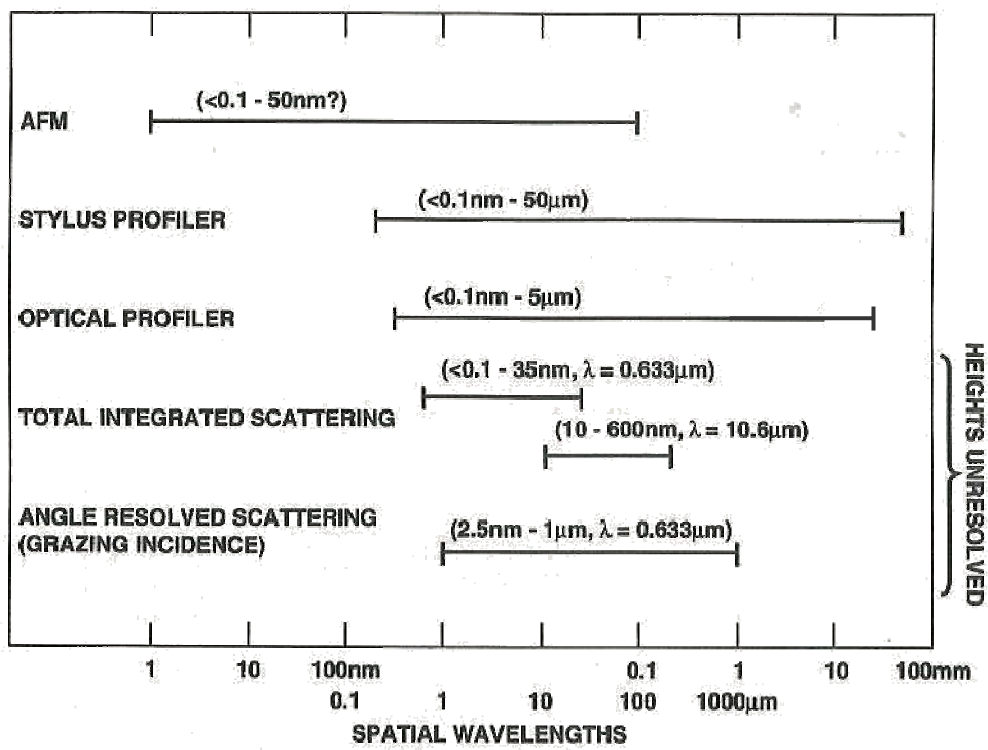

Figure 10. Various measurement tools for different spatial wavelengths [1].

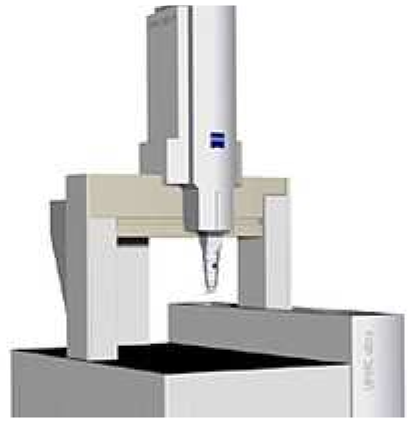

Figure 11. Stylus profiling using a coordinate measuring machine.

2.2 Optical Interference

Optical interferometry is based on the superposition principle for waves – two coinciding light waves with the same phase add constructively, while two waves with opposite phases will cancel each other out, assuming both have the same amplitude [21,22]. Given two such waves,

$$(1) \quad E_1 = E_{01}\sin(\omega t + \alpha_1) \quad \text{and} \quad E_2 = E_{02}\sin(\omega t + \alpha_2) \ ,$$

where E_0 is the amplitude, α is the phase, and the waves have identical frequencies and speed, the resultant wave is the linear addition of the waves, namely,

$$(2) \quad E = E_1 + E_2 \ .$$

Forming the sum and expanding using trigonometric identities, we obtain

$$(3) \quad E = (E_{01}\cos\alpha_1 + E_{02}\cos\alpha_2)\sin\omega t + (E_{01}\sin\alpha_1 + E_{02}\sin\alpha_2)\cos\omega t \ .$$

Since the amplitude-related quantities are constant over time, we can let

$$(4) \quad E_0\cos\alpha = E_{01}\cos\alpha_1 + E_{02}\cos\alpha_2 \quad \text{and}$$

$$(5) \quad E_0\sin\alpha = E_{01}\sin\alpha_1 + E_{02}\sin\alpha_2 \ .$$

Recalling that $\sin^2\alpha + \cos^2\alpha = 1$, we square the amplitude relations, take the sum, and obtain the resultant wave's amplitude

$$(6) \quad E_0^2 = E_{01}^2 + E_{02}^2 + 2E_{01}E_{02}\cos(\alpha_2 - \alpha_1) \ .$$

To find the resultant phase, we simply divide the amplitude relations,

$$(7) \quad \tan\alpha = \frac{E_{01}\sin\alpha_1 + E_{02}\sin\alpha_2}{E_{01}\cos\alpha_1 + E_{02}\cos\alpha_2} \ ,$$

and the resulting disturbance becomes

$$(8) \quad E = E_0\sin(\omega t + \alpha) \ .$$

The resultant wave is harmonic and has the same frequency as the individual waves, while its phase and amplitude depend on details of the two waves interfering. The phase difference between the two interfering waves is the key factor, as seen by the expression $2E_{01}E_{02}\cos(\alpha_2 - \alpha_1)$, which is known as the interference term.

A maximum amplitude is obtained when the waves are in phase, while a minimum results when they are out of phase by 180º. Assuming the waves are initially in-phase, and setting x_1, x_2 to be their respective distances from the source, we can also define the phase difference, δ, as

$$\delta = (\alpha_2 - \alpha_1) = \frac{2\pi}{\lambda_0} n(x_1 - x_2) \quad (9)$$

where λ_0 is the wavelength and n is the refractive index in the medium. The expression $n(x_1 - x_2)$ is referred to as the optical path difference (OPD), or wavefront error, of the interfering optical waves. This information is crucial to the success of an interferometric test. Comparing reference and test wavefronts provides an interferogram (contour map) of the phase differences between the two wavefronts, and enables high resolution measurements of the structure of the test surface or lens, assuming good temporal coherence. Recall that light is emitted in uncorrelated wave-trains with random phase jumps between, and the average length of a wave-train is known as the coherence length of the source. If the optical path difference between two light beams is larger than this length, then an interference pattern cannot be observed or recorded. Hence, the optical path difference between the beams must be less than the coherence length of the source in order to observe interference. For helium-neon lasers, the coherence length is typically 1 metre [1]. In optical testing with interferometry, system aberrations and reference surface

errors contribute to the OPD map and are a bias in the measurement [21]. The significance of the bias must be assessed. In optics, aberrations are defects of a lens system that cause its image to deviate from the rules of paraxial imagery. Electronic phase-measurement techniques can be used in interferometers, such as the Twyman-Green, where the phase distribution across the interferogram is measured. Phase-shifting interferometry makes use of these measurements, since it provides for rapid precise assessments of the phase distribution.

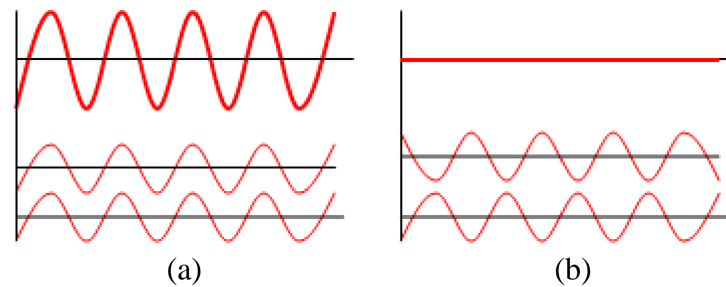

Figure 12. (a) Two waves in phase (bottom left) combine and interfere constructively to form a larger resultant wave (top left); (b) two waves out of phase (bottom right) interfere destructively and cancel out (top right) [23].

2.3 Twyman-Green Interferometry

Phase-shifting Twyman-Green interferometry is the preferred configuration for measuring refractive micro-optics [9]. The Twyman-Green is similar to the Michelson interferometer, except that it is illuminated with a point source instead of an extended source. Laser light from a point source is incident on a 50/50 beam splitter, and part of the wave is reflected while part is transmitted. Both waves have smaller amplitudes than the original wave, therefore it can be said that the Twyman-Green is an amplitude-splitting interferometer configuration. Interference between the waves reflected from the test surface and the reference mirror are detected at the detector array. In an interferometer which uses a reference surface, the measured surface heights correspond to

the difference between the test and reference surfaces, at the very least. Error sources for phase-shifting measurements include phase-step error, mechanical vibration, thermal drift, and air turbulence. All of these sources can be identified and minimized in most cases. In their paper *Vibration Insensitive Interferometry*, Millerd et al. assert that the largest limitation of phase-shifting interferometry for optical testing is the sensitivity to the environment, both vibration and air turbulence [24]. They explain that an interferometer using temporal phase-shifting is very sensitive to vibration because the various phase shifted frames of interferometric data are taken at different times and vibration causes the phase shifts between the data frames to be different from what is desired. Vibration effects can be decreased by recording all of the phase shifted frames simultaneously, while turbulence effects can be reduced by averaging many measurements. For the most precise and accurate results, instruments must be placed in a temperature-controlled space.

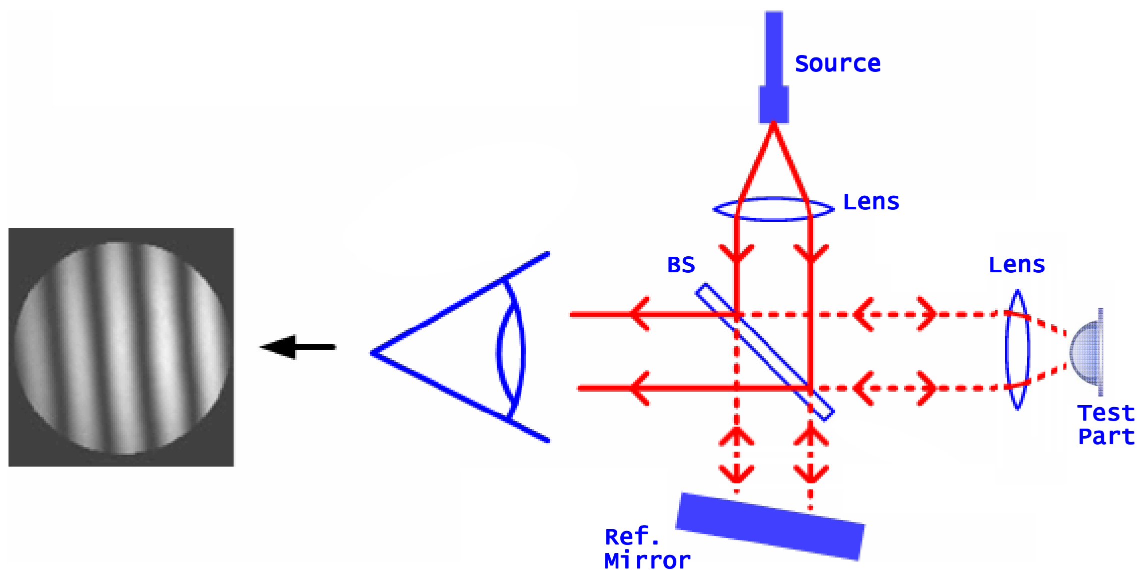

Figure 13. Twyman-Green Interferometer used to test a spherical part [22].

Phase-measurement is achieved by varying the phase of the reference wave in the interferometer in a known manner [25]. Typically, this is done by mounting the reference mirror on a piezo-electric transducer (PZT). Undesirable properties of the PZT, such as hysteresis and nonlinear motion, must be removed beforehand via calibration in optical software [26]. By changing the voltage in the transducer, the reference mirror is moved in small steps by a known amount to alter the phase of the reference wave a known amount. A detector array (CCD) detects the intensity distribution across the interference pattern. The intensity pattern is fed into a computer software program three or more times (depending on the specified algorithm), and between each intensity measurement, the phase of the reference beam is stepped a known amount. The wavefront phase is encoded in the variations in the intensity pattern of the recorded interferograms, and a point-by-point calculation recovers this phase.

Finally, the optical path difference map is obtained by unwrapping the phase profile to remove phase discontinuities and converting phase to height by multiplication of the wavelength divided by 2π. Phase unwrapping resolves the 2π phase ambiguity. In an interferometer that uses a reference surface, the optical path difference between the test and reference wavefronts nominally corresponds to the measured test surface height. Phase-shifting techniques are especially advantageous because good results are obtained even with low contrast fringes [26]. It is important to note, however, that the wavelength of the laser source affects the phase contrast and spatial resolution of the instrument.

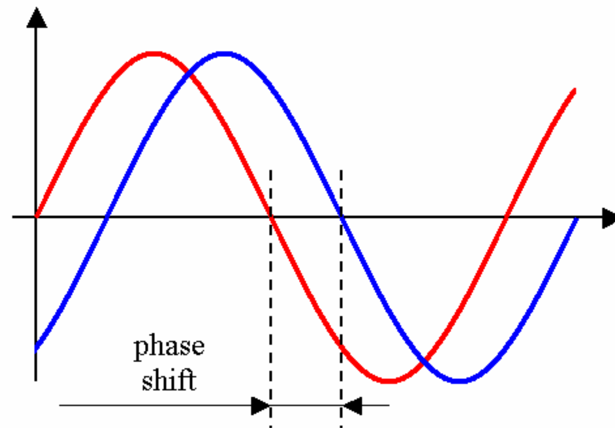

Figure 14. Phase-shifting waves; by stepping the path length by a number of known phases it is possible to recover the phase of the interference signal [27].

Most Twyman-Green interferometers utilize polarizing optics to allow for easy access to an amplitude balance between test and reference waves, and to reduce the contribution of false reflections [17]. Virtually all optical imaging systems suffer from stray light or unwanted light, i.e. light from a bright source shining into the front of the system and reaching the image as unwanted light [28]. Stray light can never be completely eliminated, and is manifested in two ways: ghost images (due to refractive optics and windows) and scattered light (from reflective surfaces). Stray light is sometimes referred to as optical noise. Typically, an anti-reflection coating is applied to each lens surface to reduce the ghosting problem. Scattered light can be minimized by eliminating straight shots in the optical system with apertures. Using a rotating piece of ground glass can also be effective in averaging out unwanted contributions by reducing the spatial coherence of the laser beam.

Aside from stray light, there are other problems with using this optical measurement method. When performing a measurement, as much as possible of the interferometer's pupil should be used in order to maximize the number of data points. An optical zoom system is key to providing pupil matching, and the resolution of the optical

measurement system is dependent upon the numerical aperture (NA – cone of light) of the objective lens, as seen in Figure 15. Magnification is another important criterion. The magnification determines the relative lateral size of the surface under test in the image plane (at the detector). However, the higher the magnifying power of the objective, the more the depth of focus is limited, and it becomes difficult in many cases to clearly image all parts of a three-dimensional object, such as a micro-lens surface [29]. The accuracy of a form measurement of a steep surface will be affected if the depth of focus is not sufficient.

A Twyman-Green interferometer set in confocal mode is useful for the measurement of the surface deviations of a micro-lens from an ideal spherical shape, as well as for the measurement of the radius of curvature of the surface. The null confocal mode is set by positioning the micro-lens where the incident spherical wavefront rays reflect from the test surface back onto themselves in coaxial fashion. In other words, the spherical test wavefront nests into the surface of the part at confocal, picking up deviations on the part, and is reflected back into the interferometer. At this position, the center of curvature of the test part is coincident with the focus of the objective lens being used. In geometrical optics, an idealized narrow beam of light, or ray, is an abstract object that is perpendicular to the wavefront. Rays are used to model light propagation through an optical system by dividing the real light field into distinct rays that can be computationally propagated through the system by a technique known as ray-tracing.

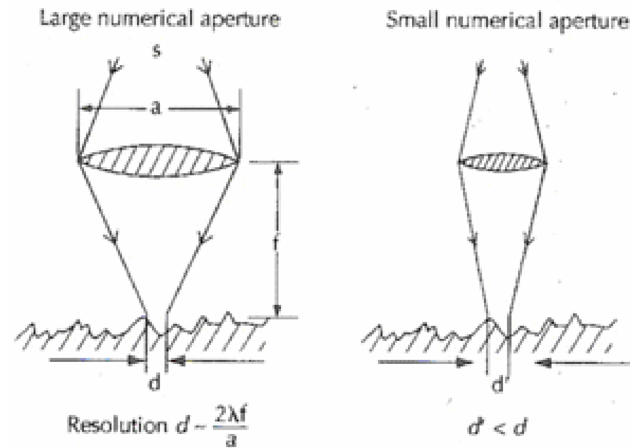

Figure 15. The dependence of system resolution on the aperture objective lens [19].

Some important limitations of phase-shifting in optical testing appear as random noise in the measurement, including the impact of environmental disturbances like vibration and air turbulence. Phase-shifted interferograms are taken at different times and vibration causes the phase shifts between the data frames to be inaccurate. Vibration effects can be counter-balanced by taking all the phase shifted frames simultaneously, while turbulence effects can be removed, to some degree, by averaging several measurements [24]. Another drawback is the technique's inability to measure optically rough surfaces. Surface roughness leads to data dropout and sharp spikes where local high surface slopes scatter light away from the detector. To decrease the effect of surface roughness, longer wavelengths should be used along with appropriate detectors. Another technique is image the interferogram onto a rotating ground glass to blur the interference fringes and filter out the higher harmonics or noise.

2.4 Self-Calibration

Using interferometry as a form error characterization tool also introduces biases (or noise) to the measurement. Random noise is an experimental uncertainty that can be

revealed by repeating a measurement and can be reduced by averaging [30]. Systematic biases, unlike random noise, are repeatable errors and cannot be revealed in this way. Repeatable errors lead to measured values that are systematically too high or too low and can be intrinsic to the instrument or introduced by human influence [31]. In many optical testing applications, the systematic instrument biases are comparable to or larger than the form errors on the lens under test, therefore a rigorous calibration method is necessary [11]. Current practice typically involves measuring a high quality part, such as a $\lambda/20$ artifact, and measured errors are equated to the instrument bias. An alternative is to use a multi-orientation self-calibration method, such as the random ball test (RBT) [13, 32]. Self-calibration is commonly used in optical testing, and in general refers to the use of an imperfectly calibrated measuring instrument and one or more imperfectly calibrated artifacts to improve the calibration of the instrument and the artifacts [33].

The random ball test is based on averaging and exploits the spherical symmetries of a sphere. Averaging techniques are often used to reduce random noise, and variations of this method have been used for self-calibration. For example, measurements of random patches of a large optical flat can be averaged together to estimate systematic biases in flatness measurements, and a similar technique using subaperture patches on a ball has been used to calibrate interferometer transmission spheres and Twyman-Green interferometers used for micro-refractive lens measurements [34]. These methods treat the errors in the calibration artifact as statistically independent noise that is reduced by averaging. The result is a calibration of the system with an uncertainty that decreases by the inverse square root of the number of random positions sampled.

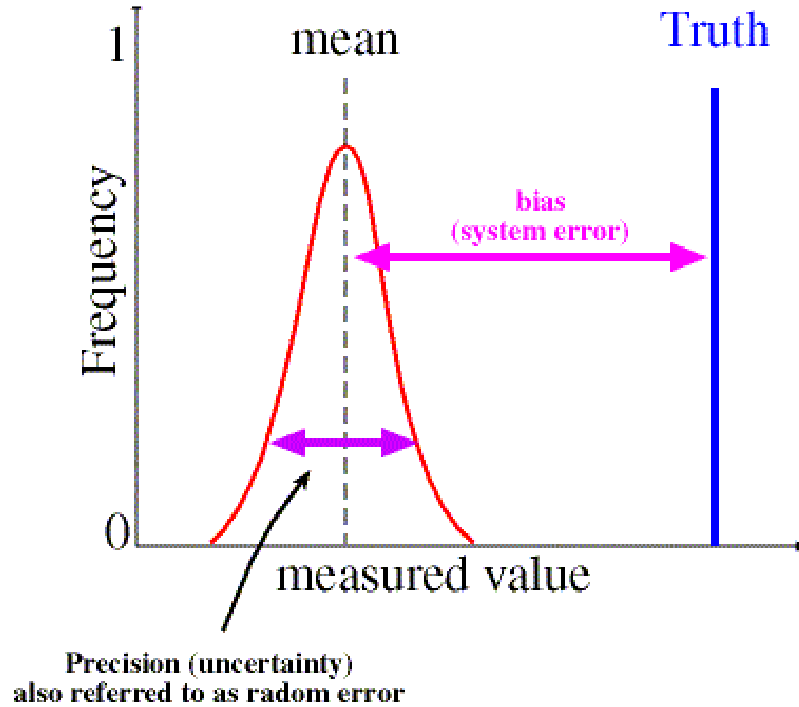

Figure 16. Systematic and random errors.

The random ball test (RBT) is an averaging technique applied to a series of sphere surface patches for the purpose of determining the bias that the interferometer itself adds to a given micro-lens form error measurement. Once determined, the bias can then be subtracted from future measurements to reduce measurement uncertainty. This technique is based on the observation that the errors on a sphere are zero on average. This is supported by the fact that the shape of a sphere can be described by a linear combination of spherical harmonics, and that the integral of each spherical harmonic over the sphere is zero (aside from the first terms which represent a constant and the base radius of the sphere) [11, 32]. When the measurements of randomly selected surface patches are averaged, the sphere form error contribution approximately drops out and the average converges to the bias introduced by the interferometer [34]. The sphere contribution to

the average identically goes to zero only in the limit of an infinite number of measurements, thus a finite number of measurements limits the uncertainty of the calibration. In previous work, we demonstrated the application of the RBT to the calibration of a scanning white light interferometer and a Twyman-Green interferometer using a 1 mm diameter steel sphere [34]. The results showed biases on the order of a few hundred nanometers peak-to-valley for both instruments.

To improve our understanding of the RBT, consider gathering a collection of measurements of the surface profile of a sphere, where the sphere is randomly repositioned between measurements. We can write each measurement (indicated by the subscript *i*) as,

$$W_i = W_{ball_i} + W_{instrument} \tag{10}$$

where the measurement is a simple sum of the form errors on a given patch of a micro-sphere and the errors introduced by the instrument itself (the instrument bias). When the measurements are averaged, the sphere surface error contribution approximately drops out and the average converges to the errors introduced by the instrument as follows,

$$\frac{\Sigma W_i}{N} = \cancelto{0}{\frac{\Sigma W_{ball_i}}{N}} + \frac{\Sigma W_{instrument}}{N} \ . \tag{11}$$

Therefore, using a random ball averaging technique enables the determination of a system bias in the instrument, namely,

$$W_{instrument} = \frac{\Sigma W_{i_i}}{N}. \tag{12}$$

This result can then be subtracted from future measurements to achieve a better estimate of surface form errors,

$$(13)\qquad W_{surface} = W_{measurement} - W_{instrument} = W_{measurement} - \frac{\Sigma W_{i_i}}{N}.$$

As previously mentioned, the random ball test is based on the fact that the errors on a ball can be described by spherical harmonics as follows,

$$(14)\qquad A(\theta,\phi) = \sum_{l,m} a_l^m Y_l^m(\theta,\phi) = \sum_{l,m} a_l^m \sqrt{\frac{2l+1}{4\pi}\frac{(l-m)!}{(l+m)!}} P_l^m(\cos\theta) e^{im\phi},$$

where $P_l^m(\cos\theta)$ are the Legendre polynomials and the coefficients, a_l^m, represent the magnitude of each term. When $A(\theta,\phi)$ is integrated over all values of θ and ϕ, only the a_0^0 (constant) coefficient survives and this reflects the radius of the ball. This shows that the departures from a best-fit sphere on a ball are zero on average. Interferometric measurements of regions on the ball surface reflect exactly this, departures from a best-fit sphere. In practice, the conditions just described are never perfectly realized though. Because an interferometer measures data over an area (or patch), the measurement areas will tend to overlap as the number of measurements grows over the surface of the sphere, which could lead to correlations in the sampling. It is also untrue that the measured area represents the form error with respect to the best-fit sphere for the whole ball surface. Actually, it only represents the departure from the local best-fit sphere. Even so, simulation suggests that this is valid in the presence of the shortcomings encountered in an experimental setting.

2.5 Aberration Theory

A perfectly corrected optical system images a point in the object plane as a point in the image plane and transforms an incident spherical wavefront into an emerging spherical wavefront. We call this a first-order paraxial, or small-angle, approximation

which is never exactly attainable. Rays that make a small angle with the optical axis and travel close to the axis are called paraxial rays. Peripheral rays interact with the edges of the components in an optical system. We can also say that deviations from the paraxial analysis provide a convenient measure of the quality of an optical device. Such departures from the ideal conditions are known as aberrations, and are embodied in five primary aberration terms, namely, spherical aberration, coma, astigmatism, field curvature and distortion.

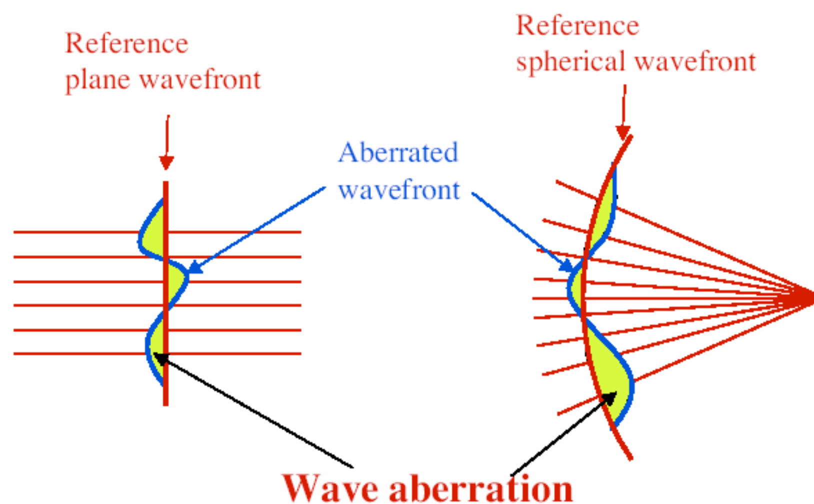

Figure 17. Wave aberrations result from defects in the components of an optical system.

Wavefront (or wave) aberrations are third-order deviations in optical path length between the actual and ideal wavefronts caused by imperfections in the components of an optical system (i.e. beam-splitter, objective lens, etc…). In the context of interferometry, aberrations can appear as a direct instrument bias in the measurement. System aberration leads to blurring of the image in a conventional imaging system, and instrument-makers must correct optical systems to compensate for aberration. Seidel polynomials are used to mathematically describe the primary aberrations. Higher-order terms also exist, and

are frequently described by Zernike polynomials, which, unlike Seidels, are orthogonal polynomials, meaning the contribution of each polynomial to the linear combination description of the wavefront is unique. In interferometry, a microscope objective lens transforms a test beam into a well-defined spherical wavefront which is useful for testing spherical surfaces and lenses.

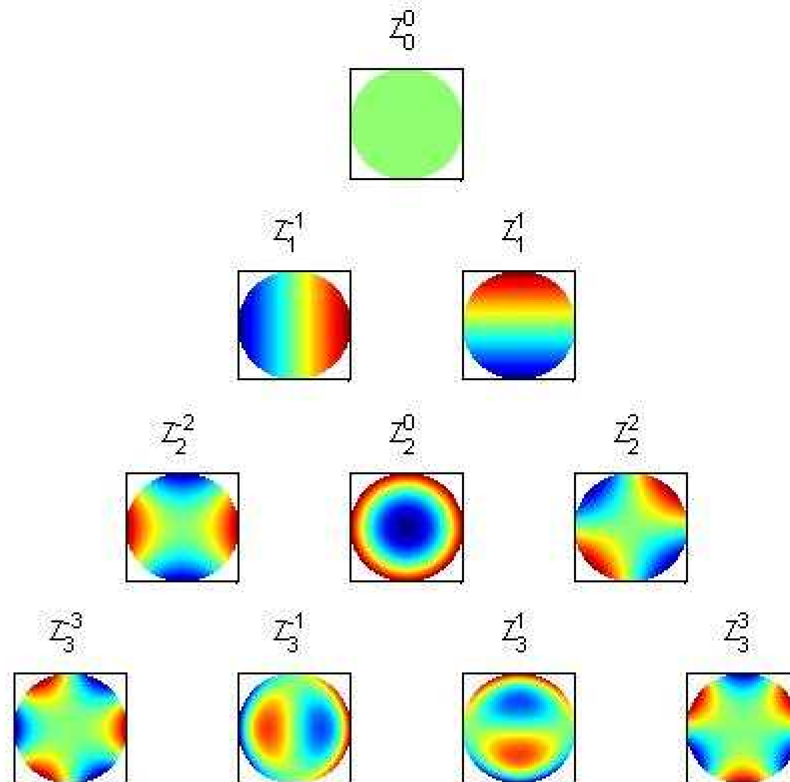

Figure 18. First ten Zernike polynomials [15].

There are two dominant naming and ordering conventions for the set of Zernike polynomials in optical testing. We follow and present here the University of Arizona's description in the form of a table of thirty-six entries. The orthogonality of the Zernike polynomials leads to several useful properties when they are used to describe a wavefront within a circular pupil. Orthogonality also simplifies the task of fitting polynomials to

the measured data points. When aberration polynomials are used to represent a wavefront, the purpose of the fit is to find the polynomial coefficients that best represent the measured data. A minor inconvenience with these polynomials, is that non-rotationally symmetric aberrations, like coma and astigmatism, are split into two components.

Polynomial	Aberration
$z0 = 1;$	Piston or Bias
$z1 = \rho\ \mathrm{Cos}[\theta];$	Tilt x
$z2 = \rho\ \mathrm{Sin}[\theta];$	Tilt y
$z3 = -1 + 2\rho^2;$	Power
$z4 = \rho^2\ \mathrm{Cos}[2\theta];$	Astig x
$z5 = \rho^2\ \mathrm{Sin}[2\theta];$	Astig y
$z6 = \rho\ (-2 + 3\rho^2)\ \mathrm{Cos}[\theta];$	Coma x
$z7 = \rho\ (-2 + 3\rho^2)\ \mathrm{Sin}[\theta];$	Coma y
$z8 = 1 - 6\rho^2 + 6\rho^4;$	Primary Spherical
$z9 = \rho^3\ \mathrm{Cos}[3\theta];$	Trefoil x
$z10 = \rho^3\ \mathrm{Sin}[3\theta];$	Trefoil y
$z11 = \rho^2\ (-3 + 4\rho^2)\ \mathrm{Cos}[2\theta];$	Secondary Astigmatism x
$z12 = \rho^2\ (-3 + 4\rho^2)\ \mathrm{Sin}[2\theta];$	Secondary Astigmatism y
$z13 = \rho\ (3 - 12\rho^2 + 10\rho^4)\ \mathrm{Cos}[\theta];$	Secondary Coma x
$z14 = \rho\ (3 - 12\rho^2 + 10\rho^4)\ \mathrm{Sin}[\theta];$	Secondary Coma y
$z15 = -1 + 12\rho^2 - 30\rho^4 + 20\rho^6;$	Secondary Spherical
$z16 = \rho^4\ \mathrm{Cos}[4\theta];$	Tetrafoil x
$z17 = \rho^4\ \mathrm{Sin}[4\theta];$	Tetrafoil y
$z18 = \rho^3\ (-4 + 5\rho^2)\ \mathrm{Cos}[3\theta];$	Secondary Trefoil x
$z19 = \rho^3\ (-4 + 5\rho^2)\ \mathrm{Sin}[3\theta];$	Secondary Trefoil y
$z20 = \rho^2\ (6 - 20\rho^2 + 15\rho^4)\ \mathrm{Cos}[2\theta];$	Tertiary Astigmatism x
$z21 = \rho^2\ (6 - 20\rho^2 + 15\rho^4)\ \mathrm{Sin}[2\theta];$	Tertiary Astigmatism y
$z22 = \rho\ (-4 + 30\rho^2 - 60\rho^4 + 35\rho^6)\ \mathrm{Cos}[\theta];$	Tertiary Coma x
$z23 = \rho\ (-4 + 30\rho^2 - 60\rho^4 + 35\rho^6)\ \mathrm{Sin}[\theta];$	Tertiary Coma y
$z24 = 1 - 20\rho^2 + 90\rho^4 - 140\rho^6 + 70\rho^8;$	Tertiary Spherical
$z25 = \rho^5\ \mathrm{Cos}[5\theta];$	Pentafoil x
$z26 = \rho^5\ \mathrm{Sin}[5\theta];$	Pentafoil y
$z27 = \rho^4\ (-5 + 6\rho^2)\ \mathrm{Cos}[4\theta];$	Secondary Tetrafoil x
$z28 = \rho^4\ (-5 + 6\rho^2)\ \mathrm{Sin}[4\theta];$	Secondary Tetrafoil y
$z29 = \rho^3\ (10 - 30\rho^2 + 21\rho^4)\ \mathrm{Cos}[3\theta];$	Tertiary Trefoil x
$z30 = \rho^3\ (10 - 30\rho^2 + 21\rho^4)\ \mathrm{Sin}[3\theta];$	Tertiary Trefoil y
$z31 = \rho^2\ (-10 + 60\rho^2 - 105\rho^4 + 56\rho^6)\ \mathrm{Cos}[2\theta];$	Quatenary Astigmatism x
$z32 = \rho^2\ (-10 + 60\rho^2 - 105\rho^4 + 56\rho^6)\ \mathrm{Sin}[2\theta];$	Quatenary Astigmatism y
$z33 = \rho\ (5 - 60\rho^2 + 210\rho^4 - 280\rho^6 + 126\rho^8)\ \mathrm{Cos}[\theta];$	Quatenary Coma x
$z34 = \rho\ (5 - 60\rho^2 + 210\rho^4 - 280\rho^6 + 126\rho^8)\ \mathrm{Sin}[\theta];$	Quatenary Coma y
$z35 = -1 + 30\rho^2 - 210\rho^4 + 560\rho^6 - 630\rho^8 + 252\rho^{10};$	Quaternary Spherical

Table 1. U of A description of Zernike aberrations [35].

Poorly-corrected objective lenses often exhibit spherical aberration which causes light passing through the periphery of the lens to focus at a different location than light passing through near the lens center. Consequently, a spherically-aberrated lens has no well-defined focus. Spherical aberration is always present for lenses with spherical surfaces. The use of symmetric doublets or aspheric lenses greatly reduces spherical aberration.

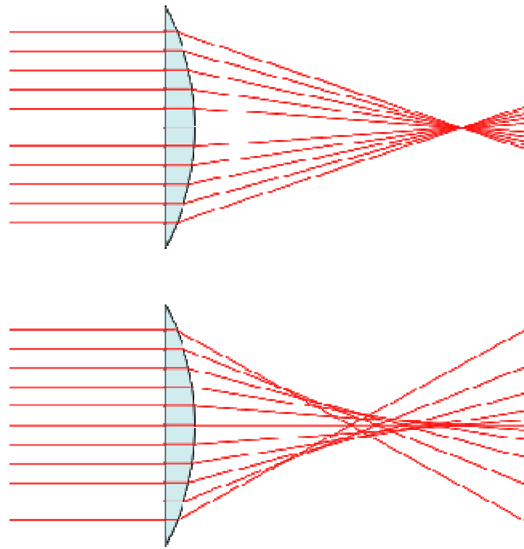

Figure 19. Spherical aberration; a perfect lens (top) focuses rays to a single point, but a real lens (bottom) focuses to different points depending on the radial position of each incoming ray [36].

Astigmatism is said to be present when an optical system has different foci for rays that propagate in two perpendicular planes. Light rays lying in the tangential and sagittal planes refract differently, which results in the different focal lengths for each plane. Astigmatism depends very strongly on the oblique angle of the light beam.

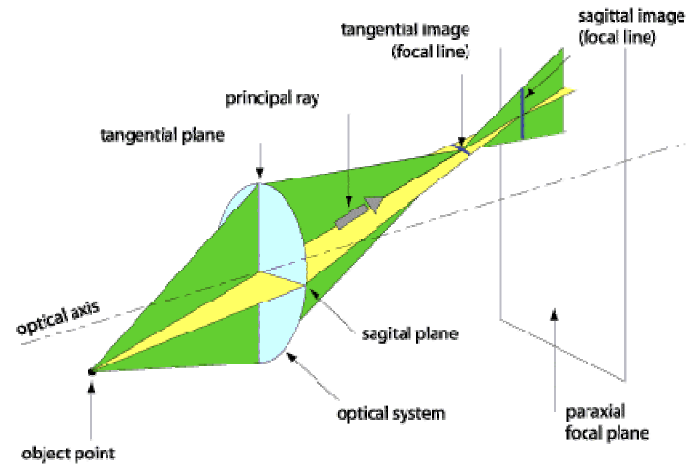

Figure 20. Rays existing in meridian and sagittal sections after being refracted by the optical system do not gather in one point due to astigmatism [37].

Coma is a result of refraction differences by light rays passing through the various lens zones as the incident light angle increases. This aberration is encountered with off-axis light and is most severe when the optical system is out-of-alignment. In other words, coma is a variation in magnification over the entrance pupil and it makes off-axis point sources appear distorted.

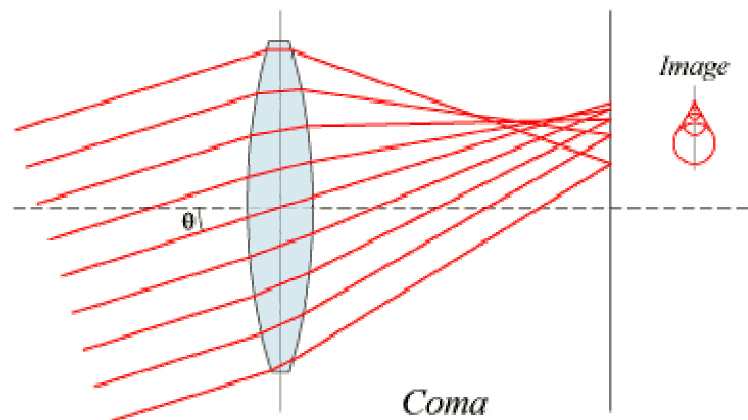

Figure 21. Coma aberration [38].

Field curvature is an aberration in which the focus changes from the center to the edge of the field of view. This aberration causes a flat object to be imaged onto a curved surface rather than a plane.

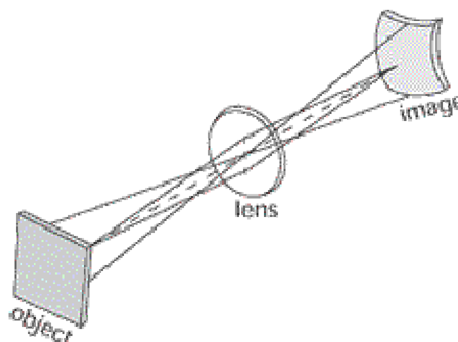

Figure 22. Field curvature [39].

When an image differs geometrically from its object, distortion is said to be present. There are two types of distortion, positive and negative, and both are caused by variations in the magnification of the optical system. A common cause of distortion is the use of a stop, or aperture, to reduce spherical aberration or astigmatism. As distortion increases, the image appears in focus over the entire field, but the image size differs at the center compared to the periphery of the field of view.

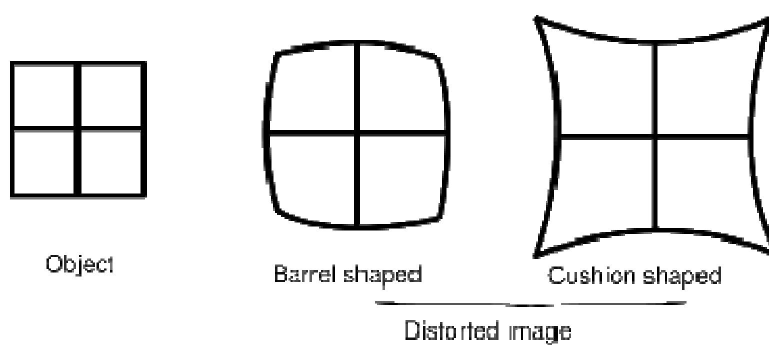

Figure 23. Distortion aberration [40].

As previously mentioned, aberrated wavefronts can be represented mathematically using the set of Zernike polynomials. The Zernike representation of the

wavefront is then a set of best-fit coefficients that each embody the fundamental aberrations [40]. Even and odd Zernike terms exist. The odd polynomials are defined as

$$(15) \quad Z_n^m(\rho,\phi) = R_n^m(\rho)\cos(m\phi) \ ,$$

and the even Zernike polynomials as

$$(16) \quad Z_n^{-m}(\rho,\phi) = R_n^m(\rho)\sin(m\phi) \ .$$

The m and n are nonnegative integers ($n \geq m$), ϕ is the azimuthal angle in radians, and ρ is the normalized radial distance. The radial polynomials R_n^m have no azimuthal dependence, and are defined as

$$(17) \quad R_n^m(\rho) = \sum_{k=0}^{(n-m)/2} \frac{(-1)^k (n-k)!}{k!((n+m)/2-k)!((n-m)/2-k)!} \rho^{n-2k}$$

if n-m is even, and,

$$(18) \quad R_n^m(\rho) = 0$$

if n – m is odd. A pre-defined set of thirty-seven Zernikes is commonly used to describe typical wavefront aberration.

a_0	"Piston", equal to the mean (or constant) value of the wavefront
$a_1 \times \rho\cos(\theta)$	"X-Tilt", the deviation of the overall beam in the sagittal direction
$a_2 \times \rho\sin(\theta)$	"Y-Tilt", the deviation of the overall beam in the tangential direction
$a_3 \times (2\rho^2 - 1)$	"Defocus", a parabolic wavefront resulting from being out of focus

$a_4 \times \rho^2 \cos(2\theta)$	"X-Astigmatism", a horizontally oriented cylindrical shape
$a_5 \times \rho^2 \sin(2\theta)$	"Y-Astigmatism", a vertically oriented cylindrical shape
$a_6 \times (3\rho^2 - 2)\rho \cos(\theta)$	"X-Coma", comatic image flaring in the horizontal direction
$a_7 \times (3\rho^2 - 2)\rho \sin(\theta)$	"Y-Coma", comatic image flaring in the vertical direction
$a_8 \times (6\rho^4 - 6\rho^2 + 1)$	"Third order spherical aberration"

Table 2. The first nine Zernike polynomials. The normalized pupil radius is ρ, with $0 \leq \rho \leq 1$, θ is the azimuthal angle around the pupil, with $0 \leq \theta \leq 2\pi$, and fitting coefficients a_0 through a_8 are the wavefront errors in units of wavelengths [40].

Defocus, or wavefront curvature, is represented in the Zernike description with the polynomial $2\rho^2 - 1$ and the coefficient for defocus is labeled a_3. The parameter a_3 has units of length but is commonly reported in waves which is a dimensionless number that is the number of wavelengths of light. Defocus corresponds to the parabola-shaped optical path difference between two spherical wavefronts that are tangent at their vertices and have different radii of curvature. Defocus refers to a translation along the optical axis away from the plane or surface of best focus. Defocus typically reduces the sharpness and contrast of an image, and sharp high-contrast edges become gradual transitions. Almost all optical devices utilize some form of focus adjustment to minimize defocus and maximize image quality. Defocus is also commonly referred to as power.

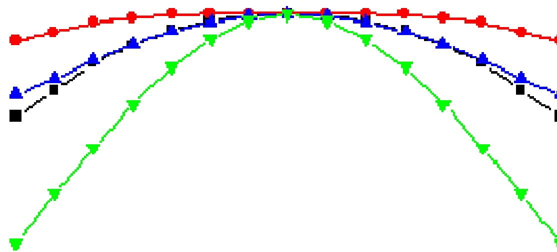

Figure 24. Defocus (power) aberration.

CHAPTER 3: CUSTOM INTERFEROMETER

3.1 Micro-Optic Reflection and Transmission Interferometer (MORTI)

We have developed a flexible and compact micro-interferometer that can be used to measure micro-lens form and transmitted wavefront errors, as well as radius of curvature and back focal length. MORTI is constructed on a Mitutoyo® microscope body and operates with a 633 nm helium-neon laser fiber input as the light source.

For form measurements, MORTI is designed to work in reflection in a Twyman-Green configuration. The input arm contains a collimating element and a pair of lenses arranged in an afocal configuration to expand the beam diameter. One of a series of high quality Mitutoyo microscope objectives (0.28 < NA < 0.9) is used as a diverging element in the test arm of the interferometer. The reference beam is reflected from a mirror mounted on a piezo-electric transducer (PZT) for phase-shifting. Interference of the recombined beams is analyzed on a CCD camera via a system of 4f relay lenses.

The instrument has the capability to measure micro-lenses with radii of curvature between 150 µm and 3 mm. Surface data is acquired and analyzed using Intelliwave™ data acquisition software made by *Engineering Synthesis Design, Inc*. Figure 27 shows all the components of the interferometer installed on the microscope body. MORTI is unique from other commercial interferometers for a few reasons, including the fact that it can measure multiple properties of refractive and diffractive lenses. Furthermore, the optical setup is fiber-based and makes use of a laser-to-fiber coupler,

whose internal surfaces are angle polished and coated to minimize back reflections. Also, it is well-known that association of the measured wavefront with the surface errors of the part requires that the phase of the wavefront at the detector (CCD array) be the same as the phase profile at the test surface. The unique focusing ability of the instrument can account for this issue, by varying the distance between the two afocal systems that make up the 4f imaging leg, via a focusing-fold-mirror-assembly (FFMA). In addition, diffraction effects stemming from double-pass configurations may be remedied by imaging the optical pupil onto the CCD. The term diffraction, implies diverse phenomena related to wave propagation, such as the bending, spreading and interference of waves emerging from an aperture. Diffraction can also be thought of as the breaking up of light as it passes around an object or through a hole.

While diffraction is always said to be present, its impact is typically only observable for waves where the wavelength is on the order of the feature size of the diffracting objects or apertures. Due to diffraction effects, a lens cannot take a point object and image it as a perfect point image, but only as a pattern of concentric rings. Consequently, there is a diffraction limit on the minimum separation of two adjacent points that even a perfect optical system can resolve, and there is little need for designing or testing an optical system to better than this limit. Rayleigh has shown that for a wavefront to be diffraction-limited, it must not deviate from a true sphere by more than a quarter of a wavelength [1].

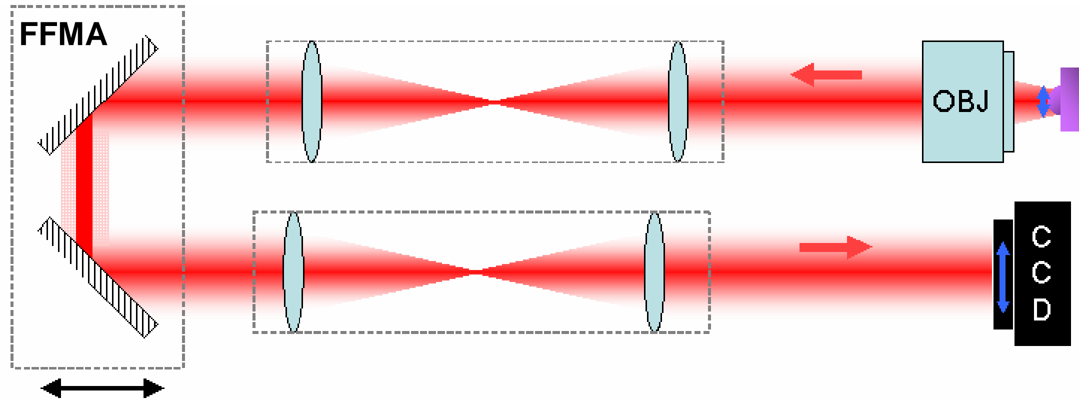

Figure 25. 4f relay system

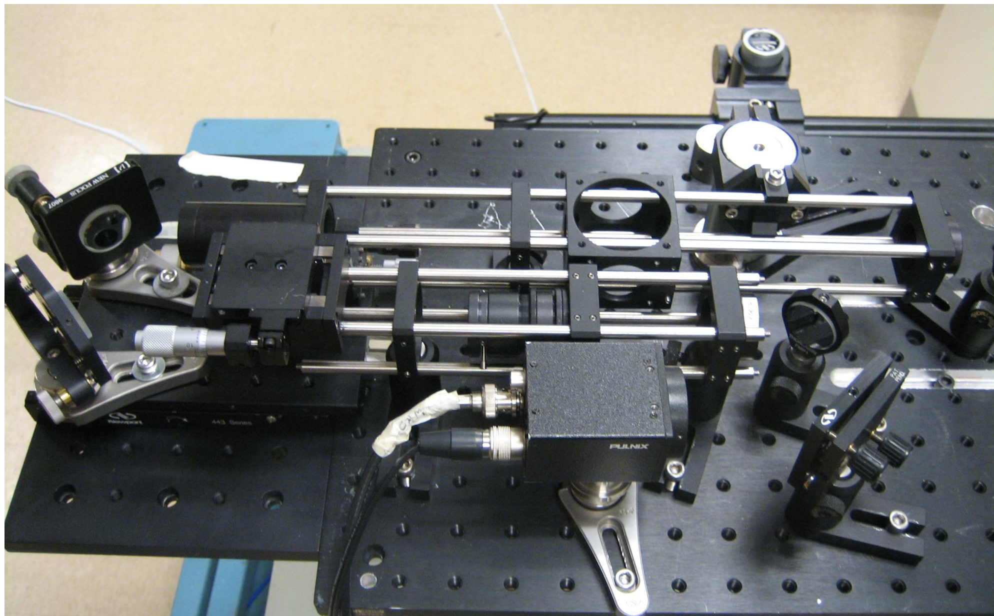

Figure 26. Actual imaging leg of MORTI.

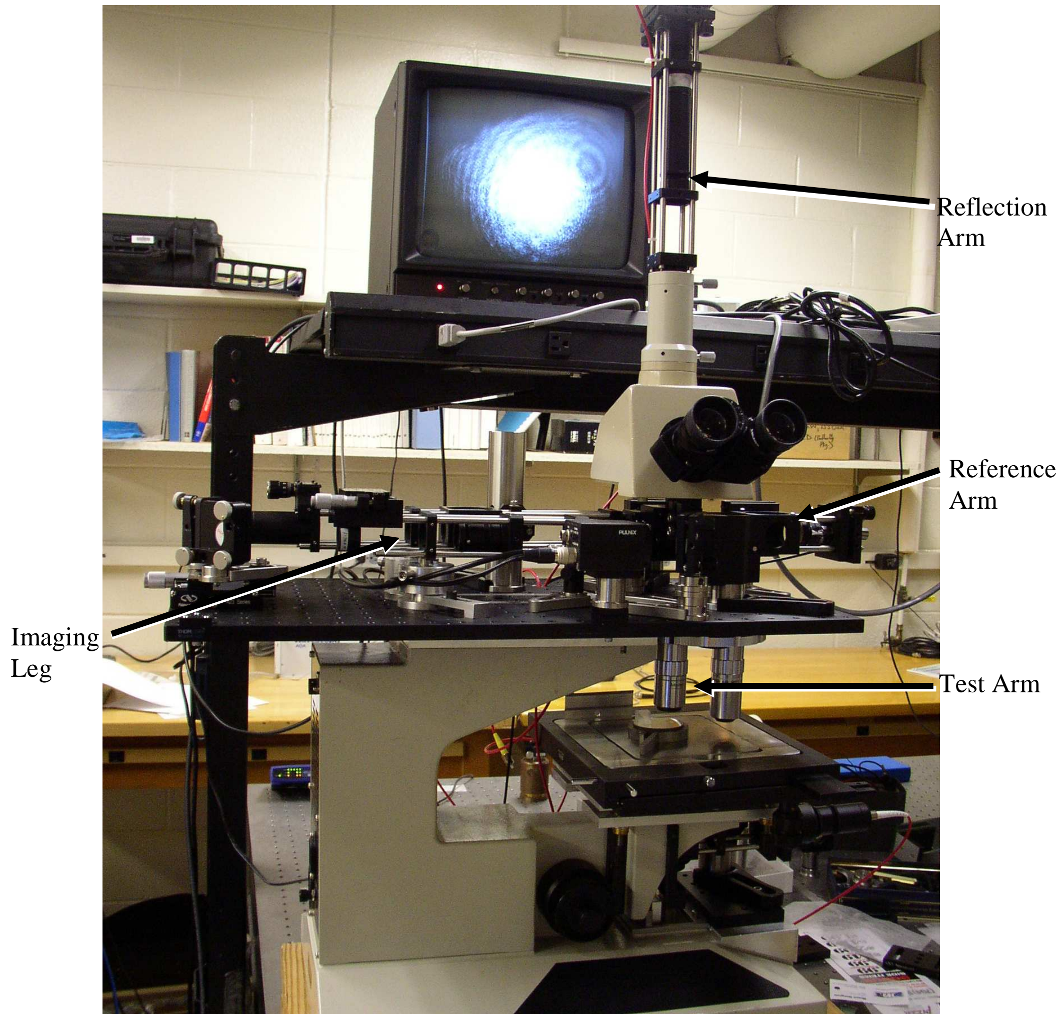

Figure 27. Micro-interferometer in Twyman-Green configuration for characterization of micro-lens form errors.

Choosing the proper microscope objective for our interferometer can have a beneficial effect on the measurement result. The numerical aperture (NA) is a dimensionless measure of the diameter of a lens aperture compared with its focal length and is one of the main factors that affect the performance of a microscope objective. Numerical aperture is an important quantity because it reveals the resolving power of a lens. The larger the cone of light that can be brought into the lens, the higher its numerical aperture. As previously mentioned, the bigger the NA of a lens, the better the resolution of a specimen will be. The size of the smallest resolvable detail is proportional

to λ/NA, where λ is the wavelength of the light. A lens with a larger NA can detect finer details than a lens with a smaller NA. Also, lenses with larger NAs collect more light and typically yield brighter images. The equation for calculating NA is the following:

$$(19) \qquad NA = n \sin\theta \ ,$$

where n is the index of refraction, and the angle θ (or μ) is half the angular aperture, A.

In selecting the best objective lens to measure a given part using MORTI, two criteria needed to be met. First, the radius of curvature (ROC) of a convex test surface must be smaller than the working distance of the objective. Second, the ROC of the test surface divided by the clear aperture should be greater than the f/# of the objective. The f/# of a lens is the ratio of its focal length to the aperture diameter. For very low numerical aperture lenses, the f/# is equal to the inverse of twice the NA. Low f/# lenses are quite sensitive to defocus and have very short depths of focus, while high f/# lenses are very tolerant of defocus, and thus have large depths of focus.

Given the vertical translation range of our microscope stage and the size of the parts we wanted to measure, we selected a Mitutoyo® M Plan Apo objective with a NA of 0.42 based on all of the factors outlined above. The objective has a magnification of 20X, a resolving power (or angular resolution) of 0.7 µm, a depth of focus equal to 1.6 µm and a 20 mm working distance. Microscope objectives are usually designed with a short working distance, which is the distance from the front lens element of the objective to the closest surface of the coverslip when the specimen is in sharp focus. In general, the objective working distance decreases as the magnification and numerical aperture both increase.

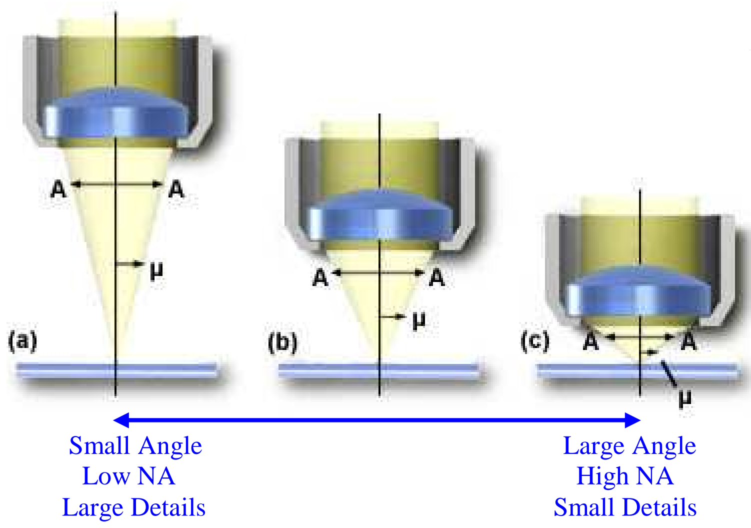

Figure 28. Resolving power of objective lenses.

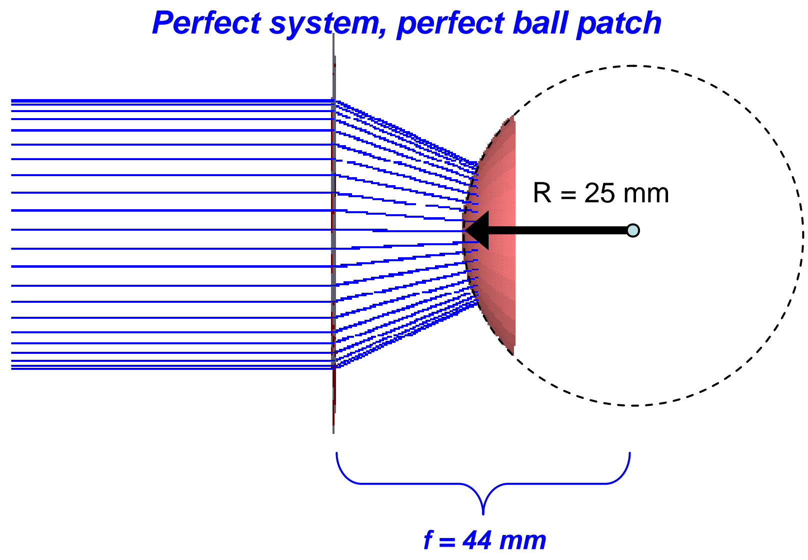

Figure 29. ZEMAX simulation of interferometer test arm showing how the radius of curvature (ROC) of a convex test surface must be smaller than the back focal length of the objective.

Most interferometer configurations are oriented with the optical axis horizontal and mounted on a vibration isolation optical table. MORTI however, was built on a

microscope frame with the interferometer's test arm oriented vertically. This unique setup allows for ergonomic, repeatable and fast changes of test pieces via mechanical cage assemblies and tubes (rigid construction), and uses less space than a horizontal interferometer setup. Also, it allows for quick changes between a reflection Twyman-Green setup, and a Mach-Zehnder transmission setup for transmitted wavefront measurements. MORTI also takes advantage of a robust vertical translation stage for positioning the test part along the optical axis, and a Sony® BS-77 optical displacement gage (or laser scale) to monitor the vertical motion of the stage. Fixtures were kept as rigid as possible to minimize vibration.

3.2 MORTI Alignment

We have found that a well-calibrated Twyman-Green phase-shifting interferometer is useful in measuring the form error of refractive micro-lenses (ROC > 400μm) with 10's nm uncertainty. Following optical alignment of all components, the instrument is calibrated using a random averaging technique called the random ball test (RBT). But first, setup of the Twyman-Green interferometer on the microscope body on a vibration isolation table must be done carefully with high attention to detail. This includes positioning all lenses and mirrored components on the main breadboard (BB1), angular alignment of the laser beams, and the alignment of the optical axis to the vertical motion axis of the stage. Some of the alignment steps are not intuitive and require practice and repetition for proper implementation.

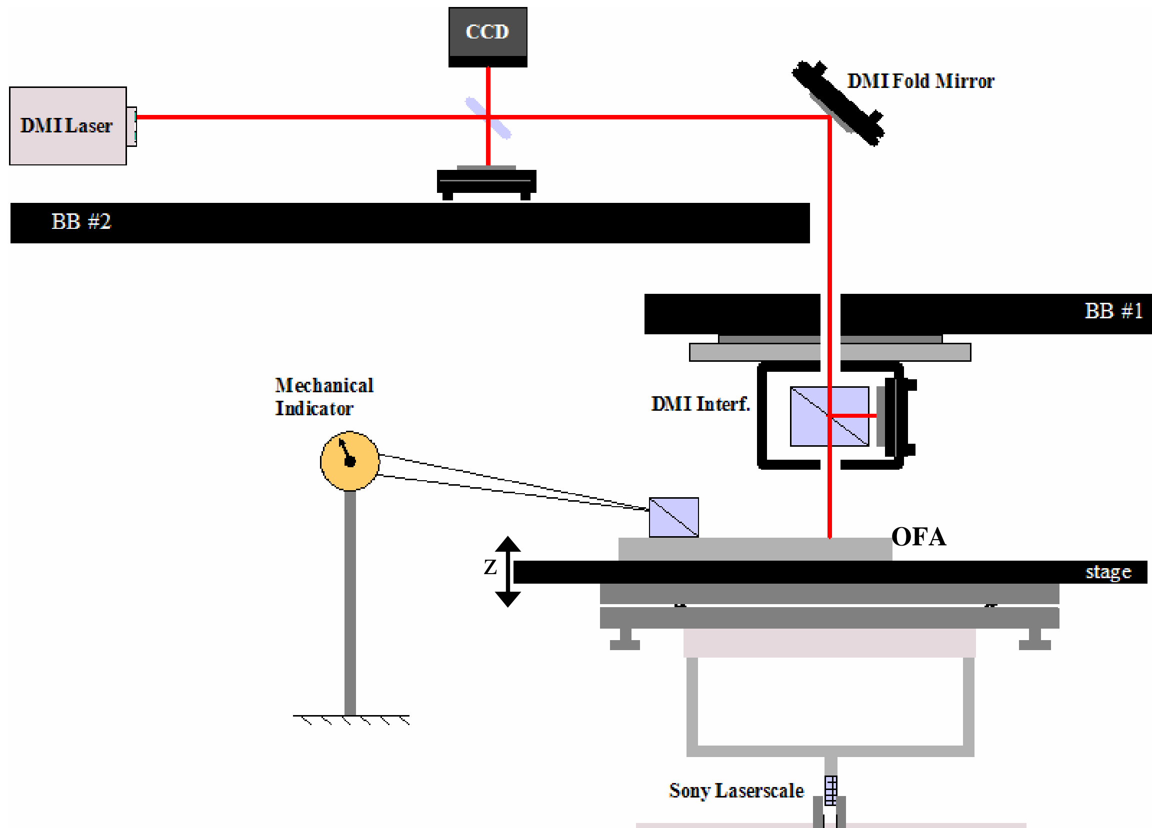

Figure 30. MORTI configuration for alignment procedure.

The main breadboard (BB1) holds the microscope's trinocular head, as well as the laser input, test, reference and imaging arms of the interferometer. A turret with multiple objective lens slots is mounted below BB1. The sample stage sits below BB1 and includes a large custom tip/tilt mount below the standard microscope translation stage, allowing for small angle and position adjustments. These degrees of freedom are important when measuring components and are also critical for the initial alignment process to align the optical axis to the vertical motion axis of the stage.

Figure 31. Optical flat assembly on microscope stage.

For the first stage of the alignment, a part known as the optical flat assembly (OFA) is positioned on the stage. The OFA consists of an optical flat mounted in a vise-like apparatus with kinematic positioners to allow for repeatable and fine rotational adjustments. A mechanical beam-splitter sits flush on the surface of the flat, secured with glue. Also, a small piece of paper with a crosshair drawn on it, is affixed to the flat. Just below the stage, the Sony laser scale is mounted. Once calibrated, the laser scale (resolution = 0.1 μm) offers highly repeatable measurements of the stage displacement in z.

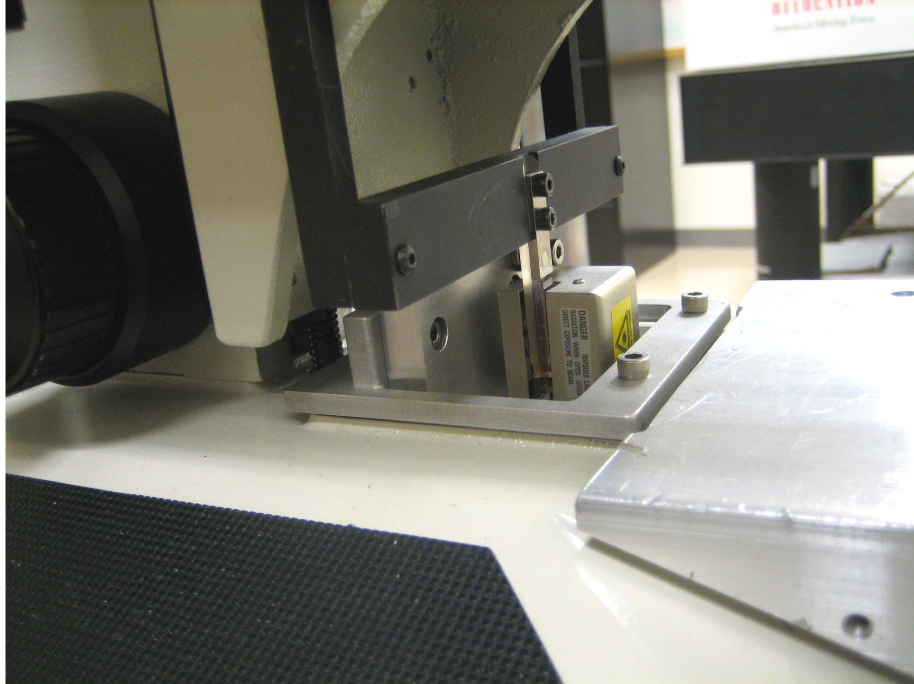

Figure 32. Sony laser scale for accurate positioning.

Aside from the Twyman-Green components, a secondary instrument, a Hewlett-Packard® 5528 heterodyne (two frequencies) displacement-measuring interferometer (DMI) is setup on a secondary breadboard (BB2) on a tripod that sits on a rubber-footed table. This instrument is required for completion of the initial alignment steps. A second breadboard (BB2) contains the DMI laser head, an imaging interferometer consisting of a flat reference mirror and a CCD, as well as a DMI beam fold mirror to redirect the beam down to BB1 and the test arm. Also, a DMI interferometer is attached to a slot in the turret of BB1. The DMI interferometer consists of a polarizing beam-splitter (PBS) and a flat reference mirror so that the DMI beam returns to the laserhead on the same path, while the laserhead detection option is set on the straightness setting.

As seen in Figure 33, the output beam from the dual frequency DMI laser source contains two polarizations with frequencies F1 and F2, and the beat frequency between

them is (F2 – F1). The polarizing beam-splitter reflects the light with frequency F1 into the reference path, and light with F2 passes through the splitter into the measurement path where it strikes the moving optical flat causing the frequency of the reflected beam to be phase-delayed and Doppler shifted by $\pm\ \delta F$. The reflected beam is then combined with the F1 light at the interferometer, and returned to the laser detector unit with a new beat frequency of (F2 – F1) $\pm\ \delta F$. Finally, high-resolution position sensing is made possible using a comparator device, which allows for stable measurements of signal phase. Deadpath error associated with environmental conditions over large distances can often be corrected and removed.

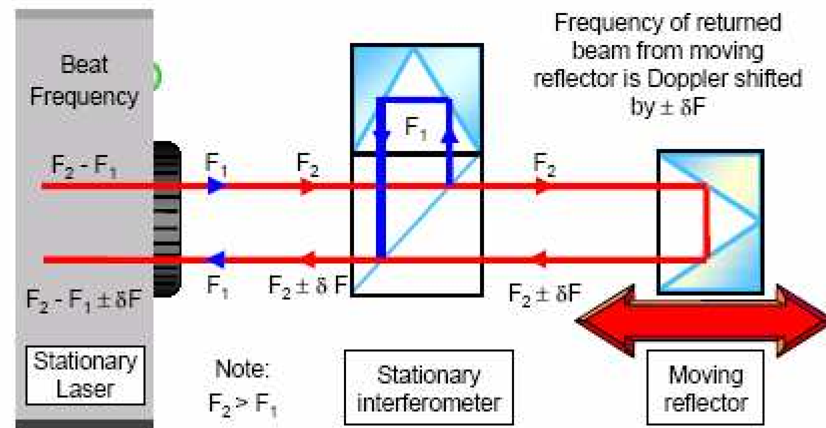

Figure 33. Typical heterodyne interferometer setup [41].

The overall alignment can be performed once the key MORTI components are in their approximate locations. The major alignment steps include the following: (1) mechanical alignment of the optical test flat to the x, y, z motions of the stage, (2) optical alignment of the imaging interferometer, (3) optical alignment of the DMI test beam to the z-motion of the stage (4) optical alignment of the DMI interferometer, (5) calibration of the displacement laser scale to the z motion of the stage, and (6) optical alignment of

the Twyman-Green interferometer setup. Co-linear alignment of the DMI test beam with the z-motion axis of the stage is crucial for reduction of abbé offset and cosine displacement errors.

Beginning with mechanical alignment to the stage motion, we assume that the vertical faces of the mechanical beam-splitter are perpendicular to the optical flat surface. First, we fix a mechanical indicator (1 μm resolution) to the vibration isolation table, and indicate with a mechanical indicator off of the x, y beam-splitter sides as the stage is translated along its x and y axes. We align the x, y vertical faces of the beam-splitter to the x, y motions of the stage by translating in the x, y directions while we execute small rotations of the optical flat in its assembly until the indicator reading stays constant. Next, we align the x, y vertical sides of the beam-splitter to the z motion as the stage is moved up and down. To do this, we tip and tilt the stage until the indicator reading is constant during z translation.

Once the beam-splitter on the OFA is parallel to the motion axis, the optical flat of the OFA is approximately perpendicular to the motion axis. The goal of the next step is to align the DMI beam to be perpendicular to the OFA. This is accomplished by first aligning a temporary 'imaging interferometer' to the OFA. The first step is to add a retro-reflector (or corner cube) to the OFA (acts as the imaging interferometer test arm) to reflect the DMI beam back along its initial path. Tipping and tilting the imaging interferometer's reference mirror to null the interference fringes from the two DMI beams, as seen by the CCD in the imaging interferometer, aligns the imaging interferometer reference mirror perpendicular to the DMI beam. This establishes a reference for the DMI beam's direction out of the laser head.

The next step is to effectively tip/tilt the DMI laserhead and imaging interferometer by tip/tilting the DMI fold mirror (see Figure 34) to align the DMI beam perpendicular to the OFA and therefore parallel to the motion axis of the stage. The first step is to remove the retro-reflector so that the DMI beam now reflects off of the optical test flat on the OFA, and swinging in the DMI interferometer in line with the beam (below BB1) so and wedge in the DMI beam splitter below BB1 is taken into account. We then tip/tilt the DMI fold mirror to null the fringes between the imaging interferometer reference beam (aligned to the laserhead) and the DMI beam reflecting from the OFA. Once the fringes are null, the DMI beam is effectively now parallel to the motion axis of the stage. Next we swing in the 20X objective lens into the beam in place of the DMI interferometer, and we use the location of the focus point to define our x, y origin (0, 0) for the system.

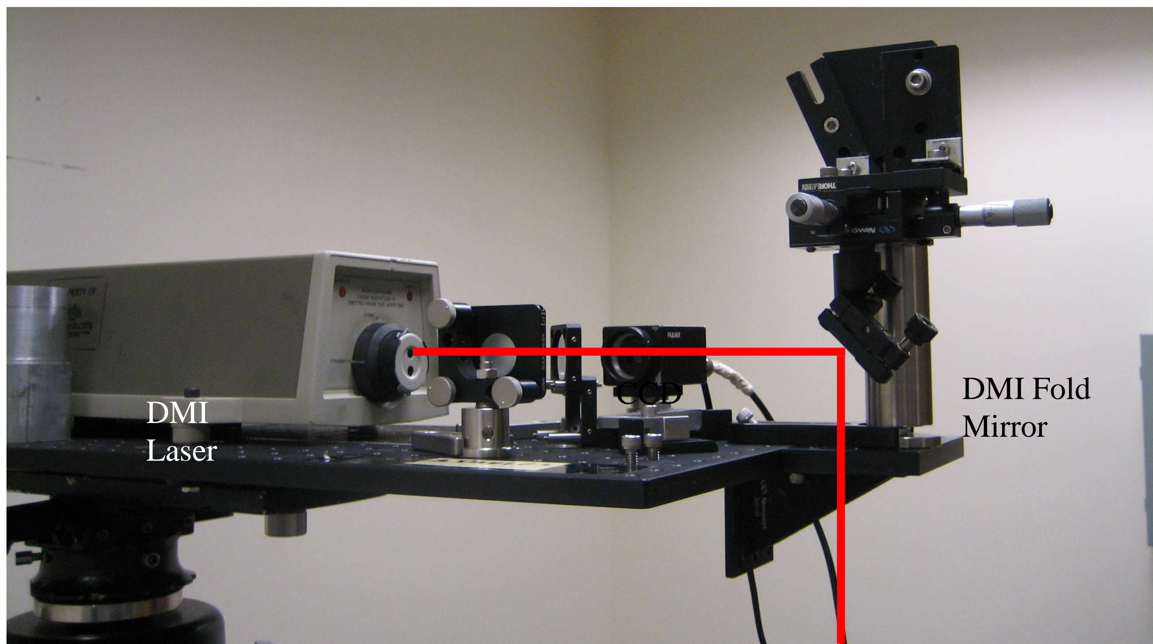

Figure 34. BB2 equipped with DMI laser source, optics and fold mirror.

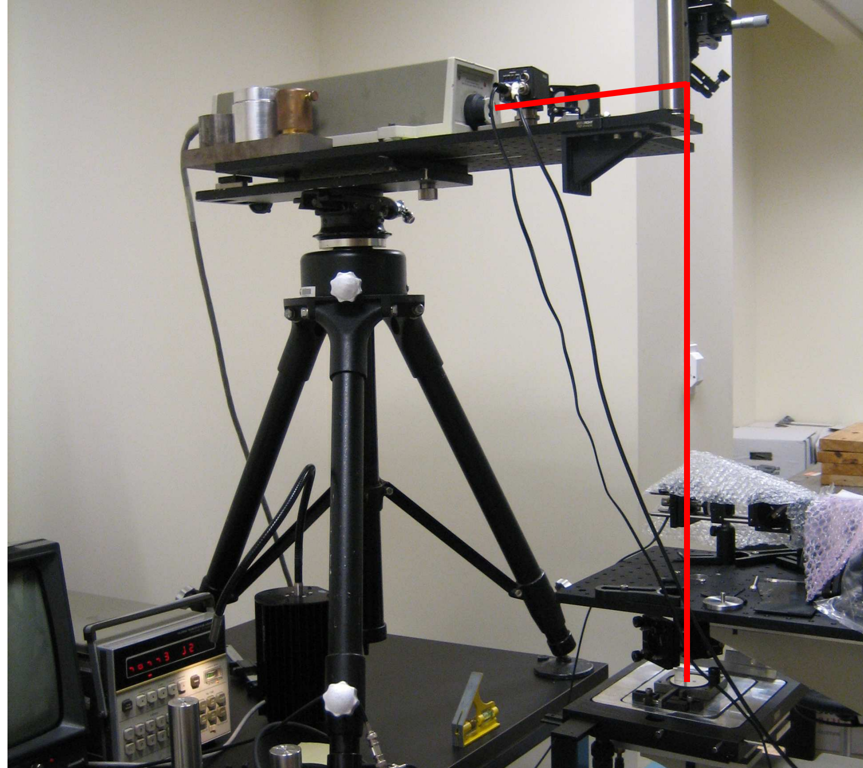

Figure 35. BB2 and tripod; directs beam to MORTI.

We are then ready for the next major step which is to define and calibrate the Sony laser scale by calibrating it against the DMI. This requires first aligning the DMI interferometer located beneath BB1. The DMI interferometer itself and its reference mirror must now be adjusted to get the DMI beam back into the input hole in the laser head and to maximize the splitting of the two polarized beams. The reference mirror angle controls the direction of the return DMI beam, and the entire DMI interferometer assembly is rotated around the optical axis to optimize the splitting of the two polarized beams. Once aligned, the DMI digital readout shows that the returning beam signal is strong and values reported by the DMI represent the vertical motion of the stage along the DMI beam and can be used to calibrate the Sony laserscale.

The Sony scale calibration involves moving the stage in z and recording the stage position using both the DMI and the displacement laser scale. Laser scale readings are displayed on a nearby computer using software known as e-counter. Calibration results are shown in Figure 36, where the red data represents using the fine stage translation knob, while the blue represents using the coarse translation knob. Taking the average of the slopes of the two linear lines yields our final calibration multiplication factor of 0.88881.

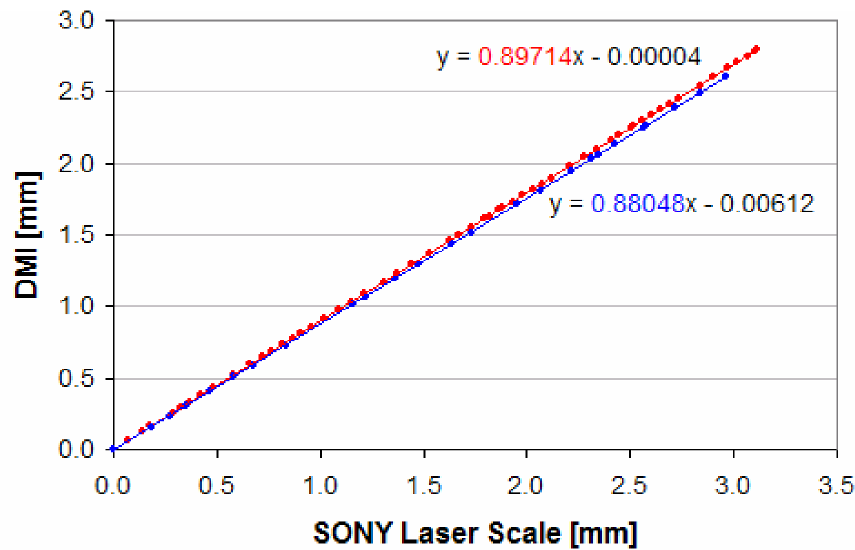

Figure 36. Calibration curves for Sony laser scale and DMI readings.

$$\text{(20)} \quad \textit{Actual “z” displacement} = \textit{(SONY reading)} * 0.88881$$

Once the scale is calibrated, we can align the Twyman-Green interferometer components on BB1. We begin by removing the DMI setup and BB2 to make room for the fiber He-Ne laser input arm of the Twyman-Green configuration.

Before this alignment begins, it is important to prepare the afocal lens pairs and optimize their position using an optical shear plate or a separate interferometer. We used a commercial Veeco® laser phase-shifting Fizeau interferometer for this alignment. We aligned a return mirror in front of the Veeco and then null the transmitted wavefront

through the afocal system by adjusting the distance between the two lenses. The FFMA is also aligned on the Veeco. This involves aligning the two fold mirrors approximately to the horizontal translation stage of the FFMA and to each other. A beam splitter is first mechanically attached to the front edge of the translation stage and the beamsplitter face then represents a surface approximately perpendicular to the translation axis and therefore can be used to align the translation axis to the Veeco interferometer. After nulling fringes off of the front face of this beam splitter, we then adjust the pitch and yaw of the mirrors to null those fringes which then further aligns the fold mirrors in the FFMA to 90 degrees to each other. Adding a small opaque card with a hole in it to the front of this setup, we translate the FFMA stage to check for motion of the spots as seen on the CCD. Rotating the mirrors until the spots stay still during stage translation is the final step. Improper alignment of this 90-degree prism-like apparatus (as seen in Figure 37) will cause the Twyman-Green beam to walk as interferometer focus is adjusted.

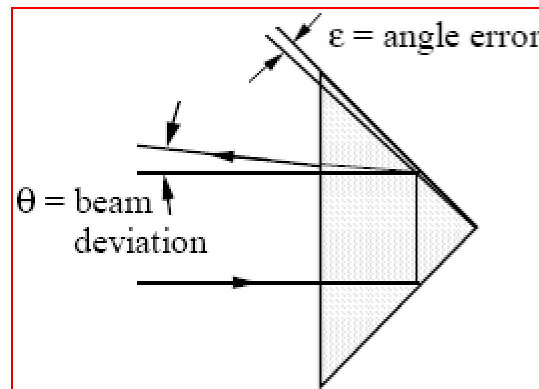

Figure 37. FFMA mirrors; focusing.

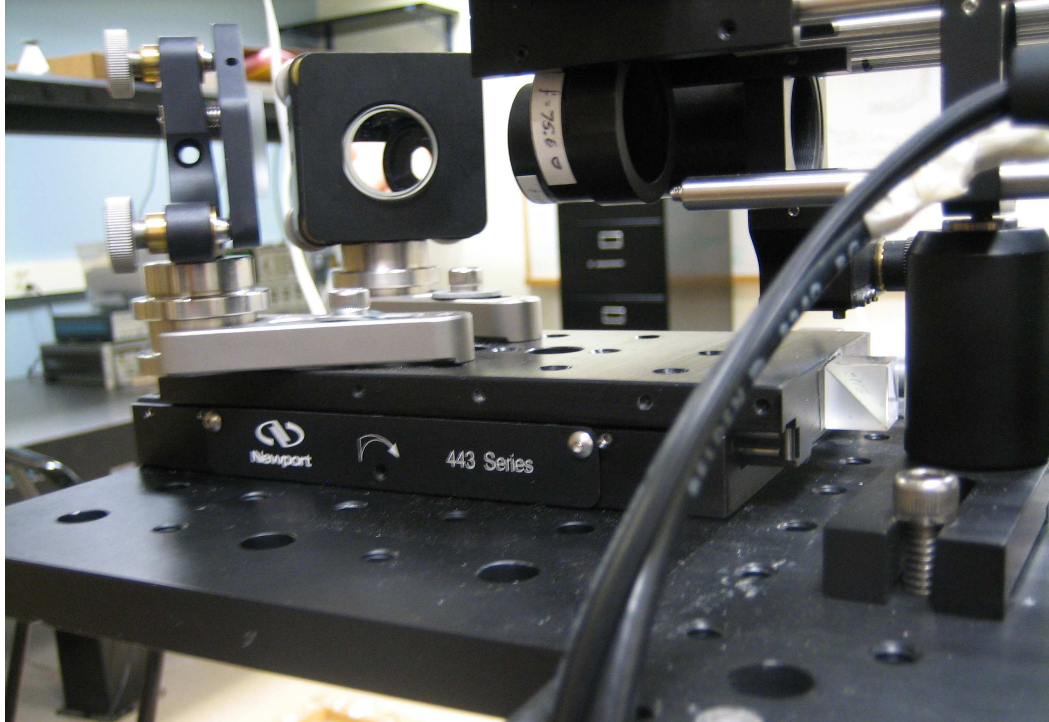

Figure 38. Actual FFMA with reference BS and 45 degree mirrors.

Having prepared the afocal systems and the FFMA, we are then ready to begin the Twyman-Green interferometer alignment. The first step is to mount the Twyman-Green input arm and the trinocular head on BB1, and translate in addition to tip and tilt so the beam is colinear with the z motion axis of the microscope stage and x, y centered on the focal point of the objective lens. Coarse alignment must be done first before beginning with the detailed alignment procedure. This step must include ensuring that the incoming beam fills the objective lens and is parallel with the axis of the objective. This is done by adjusting the xy position and angle of the objective using translation and tip/tilt stages that attach the objective to the underneath side of BB1. The detailed procedure is similar to the DMI alignment. First, after removing the objective lens and blocking M_{ref}, we adjust the direction of the incoming beam so that it reflects back on itself after hitting the

optical test flat on the OFA. We then put a retro reflector on the OFA and use the reflected beam to center the beam through the imaging system (FFMA and afocal systems) by setting the appropriate orientation of the beam-splitter (BS1). With the beam and imaging optics centered and effectively parallel to the motion axis, we replace Mref and orient it to null fringes between it and the optical test flat.

To summarize, we have made the Twyman-Green beam interferometrically parallel to the z motion. Also, Mref is perpendicular to the beam and our beam is centered well in the imaging leg. In addition, the FFMA mirrors are aligned so that the beam does not walk on the CCD upon focusing.

Also, it is important to note that the focal lengths and position of all imaging lenses as a part of the 4f system are pre-determined by performing a paraxial thin lens analysis in software (Excel) as seen in Figure 40. Using the spreadsheet, we are attempting to recreate the conditions for focusing on the test lens aperture given different size lenses. The thin lens equation allows for all parameters to be tabulated.

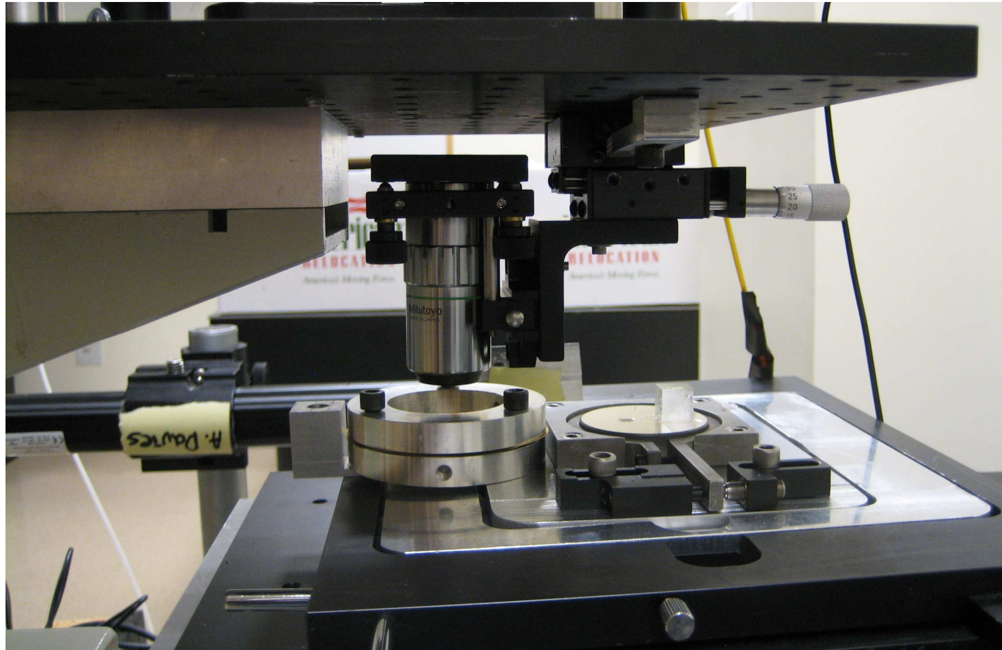

Figure 39. MORTI test arm with moveable objective lens.

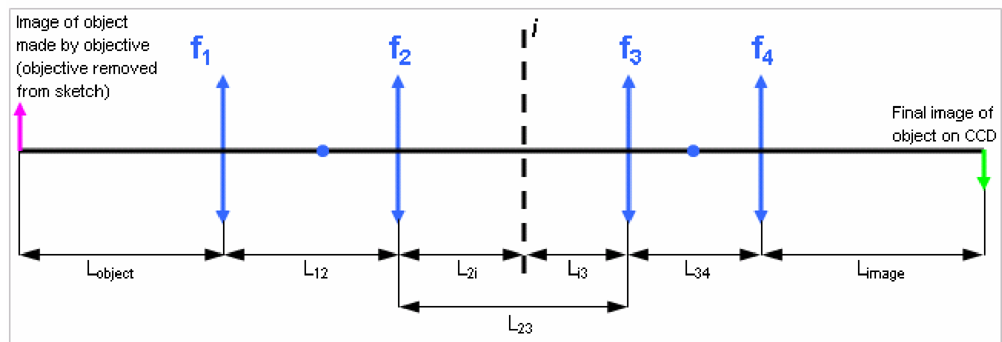

ROC	0.5	f_1	250		
$f_{objective}$	10	f_2	100		
$WD_{objective}$	20	f_3	75.6		
$NA_{objective}$	0.42	f_4	150		
L_{surf}	190	L_{12}	350	L_{1img}	578.9
L_{fixed}	250	L_{2i}	69.6	L_{2img}	69.6
L_{object}	440	L_{i3}	75.6		
$M_{objective}$	20.0	L_{23}	145.2	: min 125, max 255	
M_{12}	0.4	L_{34}	225.6		
M_{34}	2.0	L_{image}	150		
$M_{4lenses}$	0.8				
M_{total}	15.9				

Figure 40. Imaging system calculations.

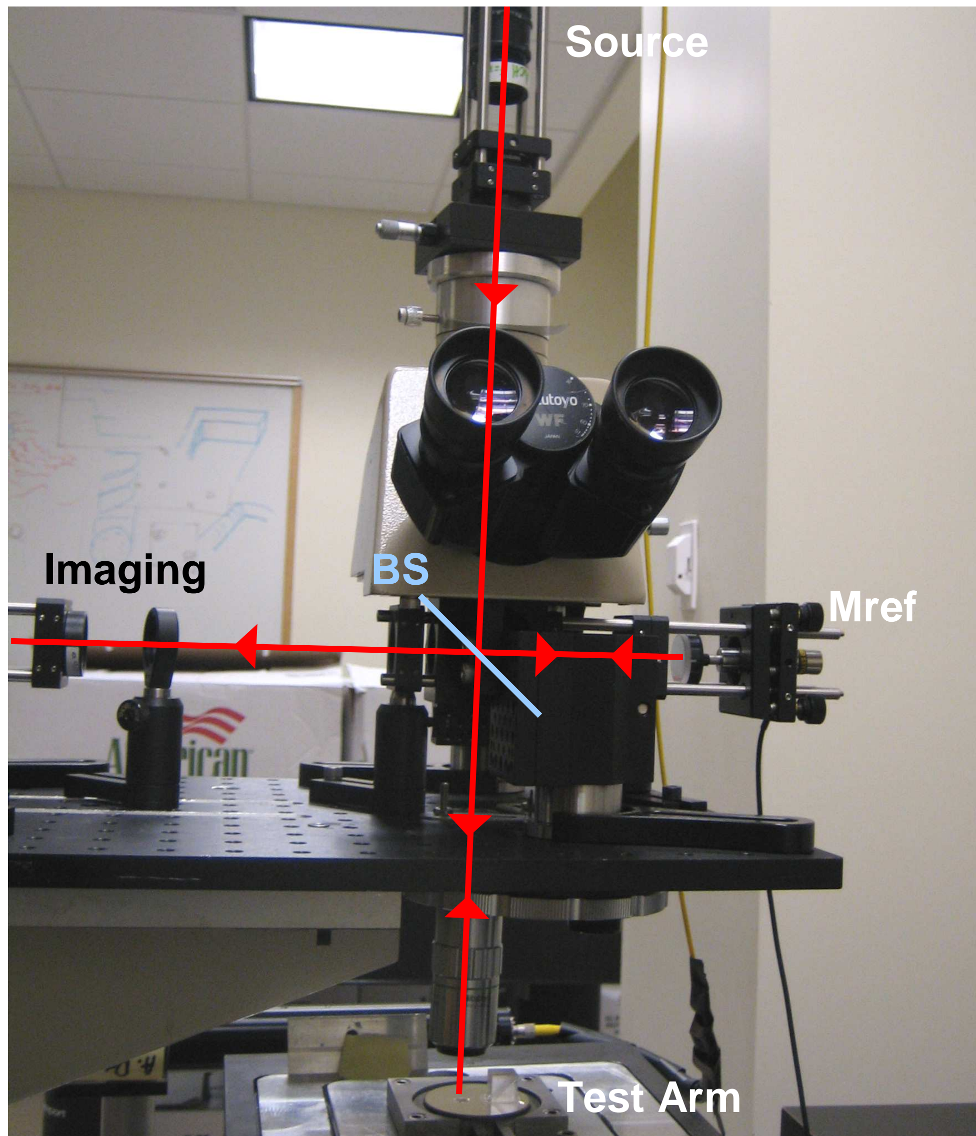

Figure 41. Twyman-Green setup.

Once assembled and aligned, the Twyman-Green interferometer is now ready for calibration, followed by measurements of opaque spherical parts. The overall system can be seen in Figure 42.

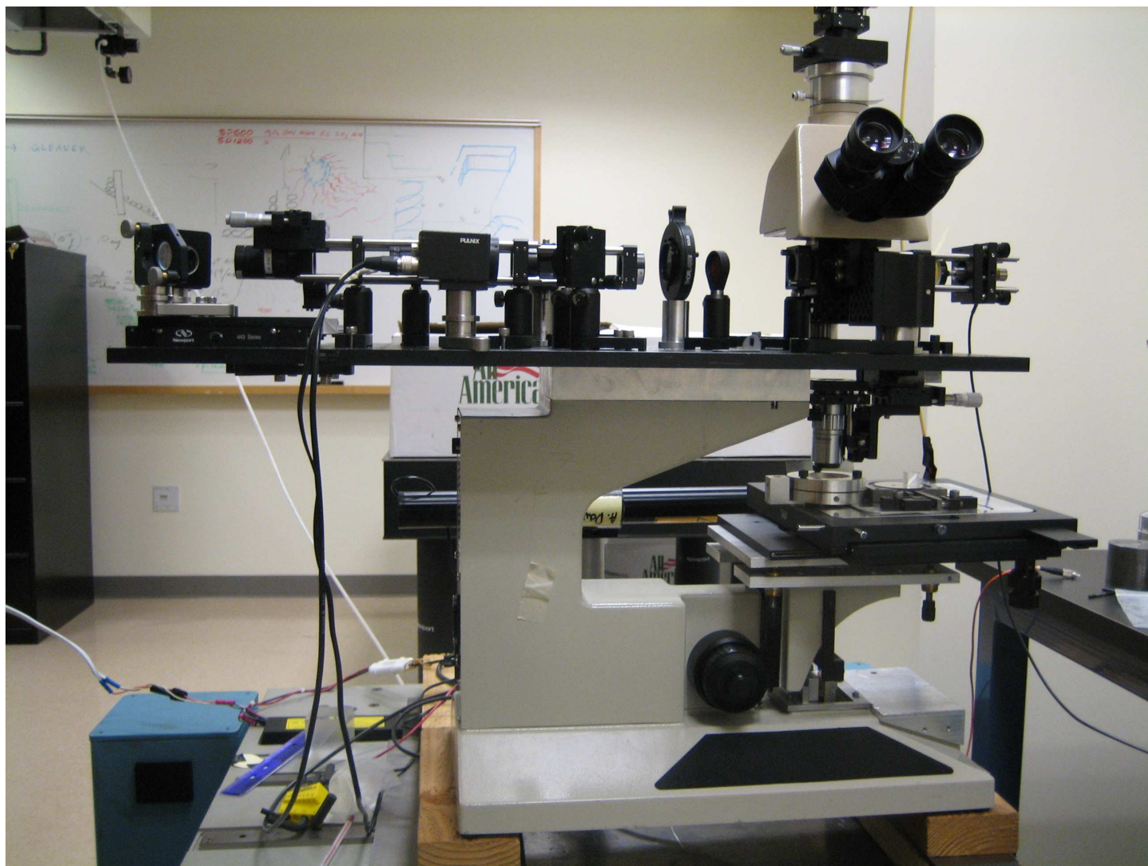

Figure 42. MORTI overview.

CHAPTER 4: SOFTWARE MODELING

4.1 Retrace Errors

A micro-refractive lens form error measurement is performed at the confocal position with the interferometer in reflection mode [34]. The wavefront in the interferometer reflecting from the test surface inherently has aberrations at some level, and reflection from an imperfect test surface causes further deviation. Consequently, the ray takes a different path back through the interferometer, thereby accumulating a different aberration. In general, this effect is referred to as a retrace error. In terms of the ray model for double-pass geometry, the function of an ideally spherical test surface is to return an incoming ray back upon itself so that it follows the same path back through the interferometer on the second pass as it did on the first. This happens exactly only when the incoming beam (the interferometer wavefront) is perfect, i.e. a spherical wavefront. But, as aberrations accumulate on the first pass, reflection off of the test surface leads to an angle change and the incoming and return rays are no longer coincident. When analyzing the resulting fringe pattern, it is no longer the case that we can divide the result by two to obtain the single-pass wavefront aberration. In general, the interferometer bias is a complicated function of the optical details of the instrument, and this effect significantly impacts measurements and calibration [42]. Ray-mapping (retrace) error introduces non-axially symmetric aberrations like coma and astigmatism in addition to axially symmetric aberrations like low-order spherical aberration [9].

Given that the actual interferometer cannot be modeled because detailed information of the optics and their configuration cannot be accurately known, we moved forward with a very simplistic model of the test arm of the interferometer to investigate the general trends and possible order of magnitude behavior. Modeling the retrace error phenomenon in the ray-tracing software, ZEMAX®, consisted of defining the test arm only of a Twyman-Green configuration, assuming the reference arm to be perfect. A paraxial lens is set as the aperture stop, while a Zernike phase surface is added to the diverger so aberrations to the wavefront (and therefore an interferometer bias) can be simulated. Aberrations can be defined on the Zernike surface in the ZEMAX 'Extra Data Editor' dialog box. The test surface is taken to be a perfect spherical, reflective object. ZEMAX traces rays through the diverger, then they reflect from the spherical test surface and propagate back through the diverger. The aperture of the second pass through the diverger is set to the same diameter as the aperture stop so rays are properly vignetted. A paraxial lens is then used to focus the light. The software can then evaluate the wavefront error (optical path difference (OPD) compared to a perfect wavefront) at the exit pupil of the system. This captures the wavefront at the aperture stop in the system, which is the last diverger in this case – this simulates focusing the interferometer on the aperture stop, as is done in the experiment. Standard ray-tracing in ZEMAX makes use of paraxial beam propagation and follows the laws of geometrical optics. Gaussian beam propagation makes use of advanced ZEMAX features, and is an expansion of paraxial optics that provides a more accurate model of coherent radiation and partially accounts for diffraction effects. However, for most optical systems and for our purposes, the paraxial model is adequate. Figure 43 depicts the ray-trace model, showing the angle

deviation which leads to the retrace error for a reasonably prescribed wavefront aberration and test lens radius for a simulated micro-optic measurement.

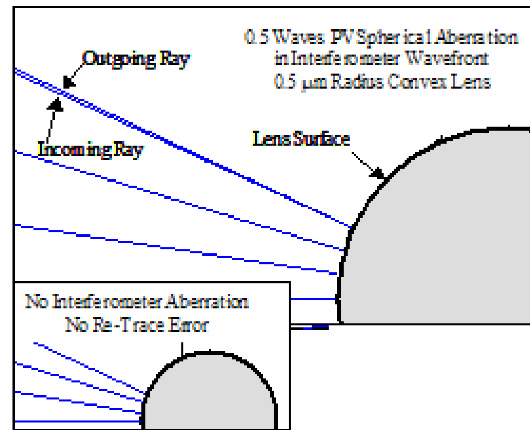

Figure 43. ZEMAX ray trace model of an aberrated interferometer wavefront reflecting from the surface of a perfect micro-sphere with a radius comparable to that of a micro-lens.

By using a perfectly aligned and perfect spherical surface as the spherical test surface in the simulation, the simulated measurement result is an exact measurement of the instrument bias. Simulated measurements of perfectly aligned, perfect lenses, show that the total instrument bias depends on the surface curvature of the test lens because of retrace errors, discussed above. The resulting interferometer bias changes dramatically with the test lens surface curvature and becomes significant in the micro-optic range. This is shown in Figure 44. The fact that retrace errors depend on the radius of the test part implies that when calibrating the instrument, even with a nominally perfect artifact, the calibration is valid only when measuring parts with the same radius as the calibration artifact. The ZEMAX simulation revealed that the retrace errors can become so extreme with poorly corrected interferometer optics and very small radii test parts that the cat's eye and confocal locations become ill-defined. While the results will be system dependent, in general the calibration will be insensitive to retrace errors only for large radius parts. Simulations show that for reasonable interferometer aberrations, the system

calibration can be modified by the retrace errors at the level of several percent in the micro-optic range. This indicates that the selection of the micro-sphere for self-calibration must be done with care for measurements of micro-lenses with demanding form tolerances.

An example of the potential order magnitude of the effect is shown in Figure 44 where λ/5 peak-to-valley (PV) of spherical aberration is added to an otherwise perfect (paraxial) microscope objective to simulate a realistic diffraction limited objective [43]. Reflection from the test lens and the subsequent retrace errors back through the objective lens lead to a total wavefront aberration that is not simply twice the aberration of a single pass. The simulation shows that if an instrument was, for example, calibrated with a large convex or concave radii artifact and then this calibration file used to correct a measurement of a very small radii micro-lens, the measurement result could be as much as 10% or more in error.

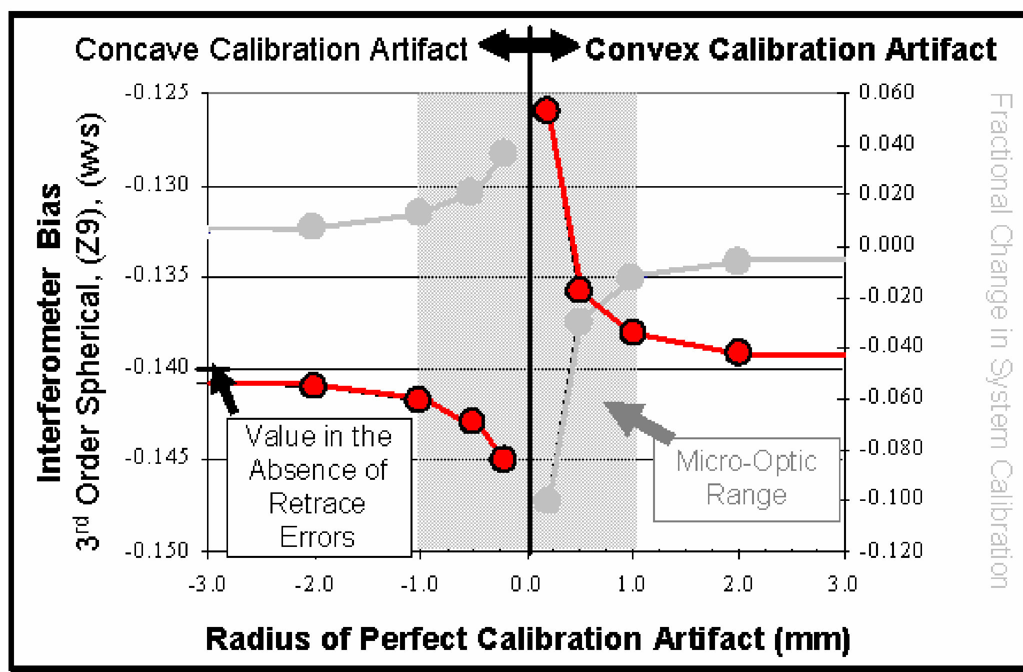

Figure 44. Simulated retrace error data for interferometer calibration with a perfect sphere [43].

Through simulation, we have shown that instrument biases in micro-interferometry depend strongly on the curvature of the part under test and this dependence can be significant in the sub-millimeter radius range. If the curvature changes, the wavefront takes a slightly different path back through the interferometer, picking up slightly different aberrations. Consequently, calibration must be done with care. Ideally, the calibration should be executed with a calibration artifact who's radius closely matches the radii of the test lenses. Meeting this requirement in order to reduce the impact of retrace errors, however, will never be completely realized given that radius measurements themselves have considerable ambiguities. This size-matching technique could also be impractical if measurements of lenses with largely different radii are desired. Given all of this knowledge, reducing the influence of retrace errors on interferometric form error measurements as stated above will only be approximately valid and future work is required in view of lessening their impact.

4.2 Artifact Misalignment

Recall that the random ball test (RBT) self-calibration technique is useful for isolating systematic wavefront biases to achieve low-uncertainty interferometric surface form measurements. In this technique, a series of sphere surface patch measurements are averaged, which leads to an estimate of the interferometer bias [34]. Previous work shows that the quality of the ball surface (rms of the form error on the ball) has a considerable effect on the rate of convergence of the test. Furthermore, sensitivity of the bias to test surface curvature motivated a more detailed investigation of misalignment during the RBT calibration. Misalignment in the centering of the ball appears as off-axis propagation back through the interferometer and introduces changes to the wavefront

aberration. Lateral misalignment of the ball causes tilt in the wavefront. Vertical misalignment leads to curvature (defocus) in the wavefront.

For example, the wavefront sensitivity to misalignment can be observed by intentionally misaligning the ball in x, y, and/or z. The tip, tilt, and defocus Zernike coefficients indicate the degree of misalignment. Plots of higher-order coefficients versus tip, tilt, and power coefficients reveal approximately linear relationships. The slopes of the lines indicate the sensitivity to misalignment. Perfect alignment during a RBT calibration is experimentally not possible, therefore the impact of these additional aberrations on the calibration procedure must be considered. To accomplish this task, we have developed a virtual model of the RBT using MATLAB® and ZEMAX. ZEMAX is used to simulate the retrace error consequences and MATLAB® is used to generate the misaligned and imperfect spherical test surface from which the wavefront reflects. The simulation is versatile, allowing for parameters such as sphericity, radius, numerical aperture (patch size), number of patches, and misalignment to be varied. It allows for a detailed investigation of the sensitivity of the RBT in a relatively short time period. MATLAB is at the forefront, where all coding and computational work is executed, while ZEMAX imports data and returns results to MATLAB for further calculation via a central dynamic data exchange (DDE) software interface [44,45].

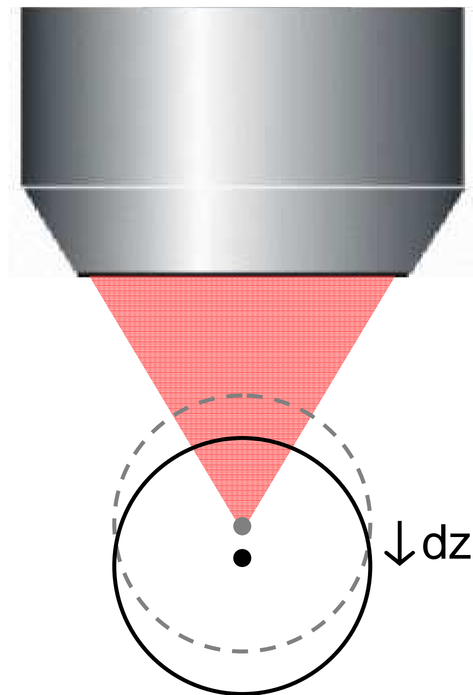

Figure 45. Example of calibration artifact misalignment from the confocal position, where a spherical beam from an objective lens ideally nests into the surface.

The basis for the model hinges on defining a sphere mathematically in terms of a set of spherical harmonic functions, and varying the amplitudes and the number of functions to adjust the form error on the sphere. Spherical harmonics are the angular part of an orthogonal set of solutions to Laplace's equation defined in a system of spherical coordinates [46]. The fact that any polynomial may be written in terms of Legendre polynomials allows us to use Legendre polynomials to represent our radial data. After determining the Legendre polynomials, we may substitute trigonometric arguments into the Legendre polynomials and obtain the spherical harmonic functions.

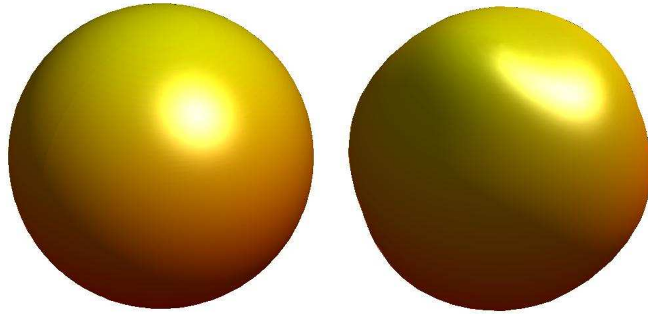

Figure 46. Spheres created by coding and spherical harmonic functions.

Hence, we have our spherical surface upon which patches can be chosen and averaged. An imperfect sphere is created simply by varying the number of harmonic functions and their multiplication constants (a_l^m coefficients). This is summarized in equation 14,

$$S(\theta,\phi)=\sum_{l,m}a_l^m Y_l^m(\theta,\phi)=\sum_{l,m}a_l^m\sqrt{\frac{2l+1}{4\pi}\frac{(l-m)!}{(l+m)!}}P_l^m(\cos\theta)e^{im\phi}, \tag{14}$$

where Y_l^m are the spherical harmonics and P_l^m are the associated Legendre polynomials [47]. Having defined our sphere, repeated random sampling of surface patches is then achieved by choosing a solid angle with random orientation on the sphere. Spherical coordinate equations facilitate this task, leading to a determination of sag data for each patch [48]. Sag, or *z*, data is a requirement for describing and importing custom surfaces in ZEMAX.

To simulate experimental conditions, misalignment of a patch can also be specified and added to the simulation. This is done by randomly choosing a combination of x, y, and z offsets of small magnitudes and modifying the orientation of the patch accordingly. The sag data is then mapped onto a uniform grid and written to a file which is sent to ZEMAX for interpretation. ZEMAX reads the data as a 'gridsag' surface, interpolates the data and generates a smooth custom surface from which the rays are

reflected. ZEMAX traces rays through the interferometer model to the surface, reflecting from the surface and heading back through the interferometer to a detector plane where the wavefront is analyzed and sent back to MATLAB for analysis. The DDE commands programmed in MATLAB allow for all data transfers between the two software packages, and finally the RBT averaging can be performed on the N wavefront matrices in MATLAB. ZEMAX contains a built-in DDE server permitting other Windows® applications, including MATLAB to access it. The DDE is an interprocess communication system built into the Windows operating system. It is a feature of Windows that allows two programs to share data or send commands directly to each other [49].

In our case, ZEMAX acts as the server while MATLAB is the client. Links are initiated in the client application and are manually programmed. One advantage of sharing data between programs is the ability to create custom surfaces for use in ray-trace models. Another advantage is that we can modify or acquire many ZEMAX parameters using MATLAB commands and unique MATLAB tools, like the random number generator to simulate random ball misalignment, matrix averaging for wavefront post-processing, and statistical functions like standard deviation to analyze calibration uncertainty. The same ZEMAX interferometer model is again used, but in this case, the test surface is taken to be an imperfect misaligned sphere patch generated in MATLAB.

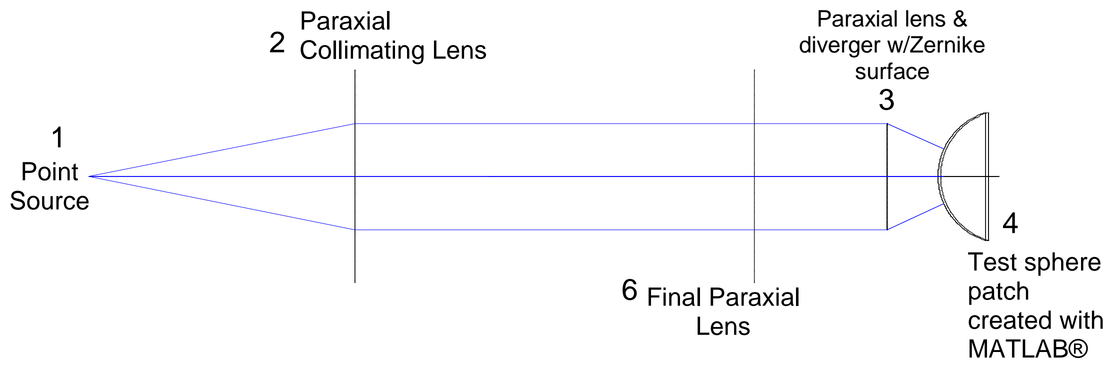

Figure 47. ZEMAX model of test arm of interferometer.

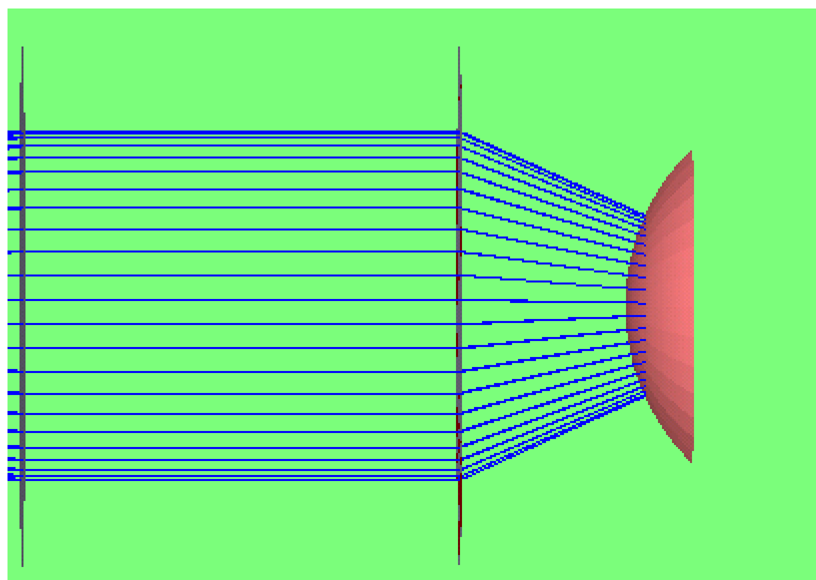

Figure 48. ZEMAX 3D model of test arm of interferometer.

Programming our unique random ball simulation required careful consideration before execution and frequent debugging throughout. Few literary sources documenting the DDE coding technique are available and none describe our particular application.

Having described the basis for the model, let us now move to a discussion of the major road blocks encountered in the programming. For example, when creating our sphere in terms of spherical harmonic functions, it was necessary to use spherical

coordinates, and hence have a grid that varied with radius and angle. However, ZEMAX can only interpret data contained in a uniform x-y grid. The solution was the 'griddata' function in MATLAB, but it also had requirements. In testing the function we discovered that 'griddata' was not robust when applied to large matrices with duplicate or near duplicate elements. This brought about the need for an additional MATLAB function called 'consolidator', which we modified for compatibility with our software version [50]. The 'consolidator' function solves interpolation problems by allowing a tolerance to be specified on how close two values need to be to be considered duplicates. Remedying the duplicate data points issue, unfolding the x, y, and z matrices into vectors and creating a uniform x-y grid with the 'meshgrid' command allowed the 'griddata' function to effectively convert spherical data into cartesian data. Writing the sag data to a file in the format specified by ZEMAX was tedious and required considerable syntax. Finally, specifying any base radius for the custom surface in ZEMAX yielded incorrect data. The answer was to simply set the radius of the 'gridsag' surface to infinity before sending custom data from MATLAB.

Lens Data Editor

Edit Solves Options Help

Surf	Type	Comment	Radius	Thickness	Glass	Semi-Diameter	Conic
OBJ	Standard		Infinity	100.000000		0.000000	0.000000
1	Paraxial			200.000000		30.000000 U	
STO*	Paraxial			0.000000		20.000000 U	
3*	Zernike Frin..		Infinity	18.999437 V		30.000000 U	0.000000
4*	Grid Sag		Infinity	-18.999437 P	MIRROR	19.000000 U	0.000000
5*	Zernike Frin..		Infinity	0.000000		30.000000 U	0.000000
6*	Paraxial			-50.000000		30.000000 U	
7	Paraxial			-100.000000		30.000000 U	
IMA	Standard		Infinity	-		51.653994	0.000000

Extra Data Editor

Edit Solves Tools Help

Surf	Type	Zernike 4	Zernike 5	Zernike 6	Zernike 7	Zernike 8	Zernike 9
OBJ	Standard						
1	Paraxial						
STO*	Paraxial						
3*	Zernike Frin..	0.000000	0.000000	0.000000	0.000000	0.000000	0.250000
4*	Standard						
5*	Zernike Frin..	0.000000 P	0.000000 P	0.000000 P	0.000000 P	0.000000 P	0.250000 P
6*	Paraxial						
7	Paraxial						
IMA	Standard						

Figure 49. ZEMAX data editors for prescribing variables and biases.

Having established data transfer, we then tested its limitations, starting with a large radius ball (R = 25 mm) where retrace errors would be negligible. We began by running one iteration with no test arm aberrations (i.e. a perfect system) and a perfect custom spherical patch, and expected to see a nearly flat output OPD wavefront map. To our surprise, the resulting map contained considerable residual aberration, on the order of 1 part in 10^2 waves rms (0.0110 waves). This was caused by interpolation problems in ZEMAX with treatment of the gridsurface. But this discovery in ZEMAX was useful. ZEMAX uses an iterative method to find the ray-surface intersection in the case of the ‘gridsag’ surfaces, and there seem to be convergence errors for custom surfaces with steep slopes. Consequently, ‘gridsag’ data should not be used to model surfaces of large sag, but rather to model small deviations from a standard surface. Setting the radius of curvature of the ‘gridsag’ surface to that of the best-fit sphere instead of infinity, and sending OPD sag data (small deviations normal to curved surface) instead, resulted in an output wavefront rms close to 1 part in 10^3 waves (0.000817 waves).

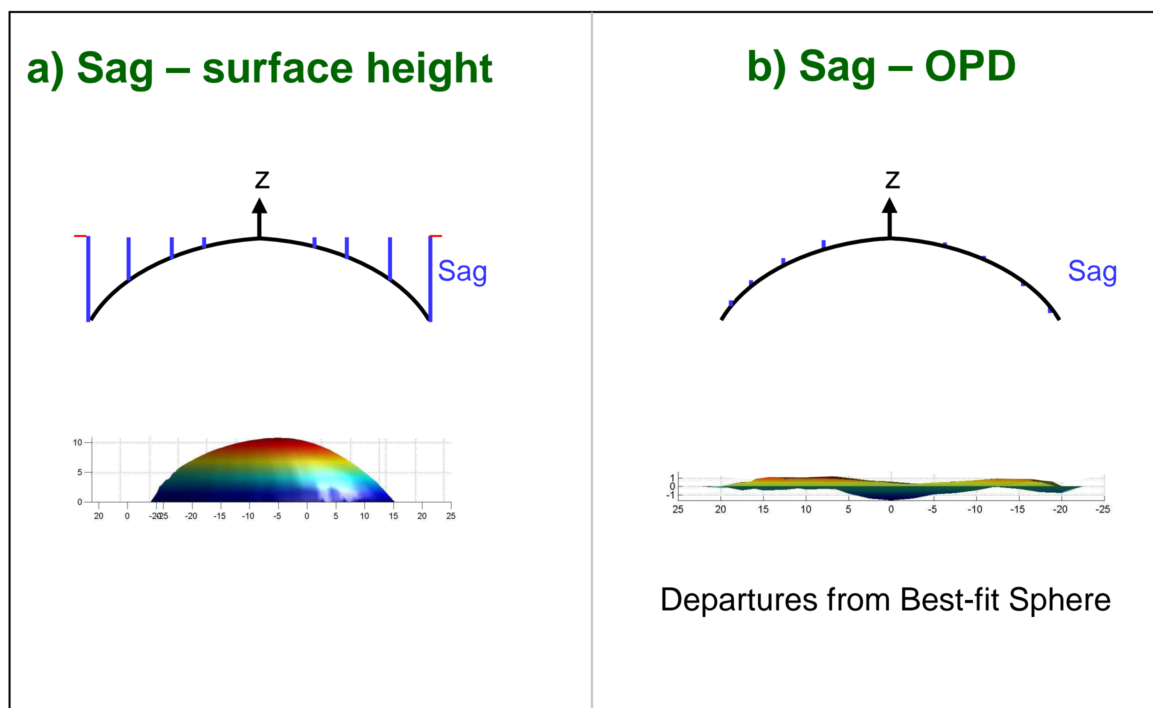

Figure 50. Different techniques for sending sag data to ZEMAX.

Increasing the grid density for the sag data description of the spherical patch from 101x101 to 201x201, and programming ZEMAX to perform bicubic instead of linear interpolation, further improved the rms results (as seen in Figure 51) to nearly 1 part in 10^5 waves (0.0000158 waves) without significantly reducing computational time. With bicubic interpolation, the value of a function at a point is computed as a weighted average of the nearest sixteen samples in a rectangular grid (a 4x4 array). The resulting output wavefront is flat to within the diffraction limit. Additional structure is still present in the map due to residual computational noise. This noise limit must be considered when drawing conclusions from the simulation results in the ultra-precision limit. It is also important to note that ZEMAX cautions that one should always expect some residual deformation with the 'gridsag' model. Using the 'gridsag' template was not intuitive, and in doing so, we required much assistance from the ZEMAX customer support help

desk. Perhaps it is not a coincidence that ZEMAX has recently made considerable changes to their 'gridsag' help file in their software manual.

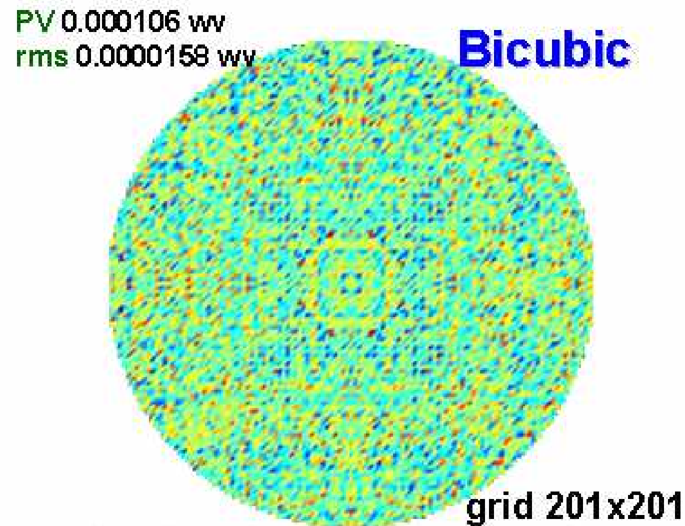

Figure 51. Map showing resulting rms values indicates the sensitivity of the simulation.

Prescribing an imperfect ball and increasing the number of iterations was the next step to confirming that the RBT was performing as expected. We chose a realistic rms form error of 1/5 of a wave (0.18 waves) for the ball and raised the number of iterations to N = 100. The resulting wavefront map had an rms residual value of 0.00171 waves. Next, we programmed 500 iterations and obtained an rms of 0.000350 waves. Finally, using N = 3000, the simulation ran for a couple of hours and revealed good results - a virtually flat map with residual rms of 0.0000691 waves. The result map for N = 3000 is seen in Figure 52.

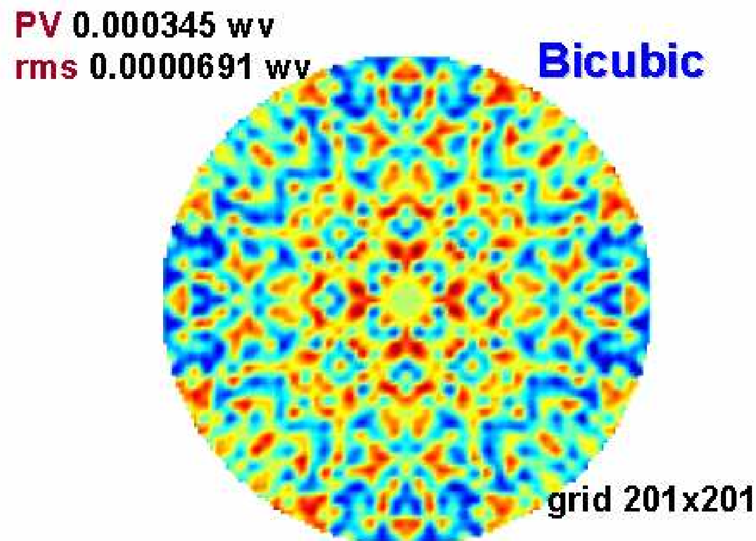

Figure 52. Map showing resulting rms values for a typical random ball test.

As previously mentioned, our desire to concentrate on the positioning/alignment of the calibration artifact was driven by the data trend that we observed in studying retrace errors. To summarize that study, we learned that the return angle of inherently misaligned rays depended greatly on the location at which they were reflected from the calibration sphere and the local slopes at those locations. We hypothesized that other calibration-artifact-related effects could play a significant role in affecting the system wavefront bias (i.e. the result of the RBT). Both systematic and random misalignments of the spherical calibration artifact were included in our study.

In an effort to simulate realistic experimental conditions, we focused on random (Gaussian distributed) misalignment of our artifact by large, and then small amounts (average = 0), in the positive and negative directions. The goal was to intentionally introduce defocus (optical axis misalignment) into our optical model. Initially we used the 25-millimeter-radius ball and the 0.18 waves rms ball error as before, and specified

0.25 waves of spherical aberration as our system bias in ZEMAX. The range was defined by the maximum possible displacement in millimeters of the ball that yielded 1/2 wave of defocus in the output OPD map. Later we tested misalignment that results in 1/10 wave of misalignment in the output OPD map. One-half wave in the OPD map corresponds to about 3 visible fringes in the interferogram, while 1/10 wave corresponds to about 1 fringe. For a large radius ball, 1/2 wave of defocus resulted in 0.2668 waves rms for the output wavefront, and 1/10 wave of defocus resulted in an rms of 0.0770 waves (assuming no system bias). Using MATLAB's random number generator, pseudorandom scalar values for displacement within the allowed ranges were drawn from a normal (Gaussian) distribution with a mean of zero.

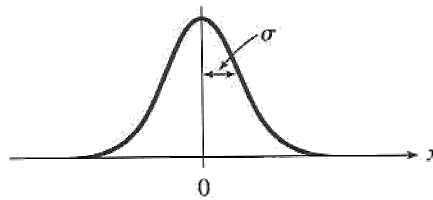

Figure 53. The Gauss function is bell-shaped and centered on $x = 0$; σ is the width, and is defined as the distance from the center of the curve to the point where the curvature changes sign.

We graphed the rms RBT results for both large and small amounts of calibration artifact misalignment, results obtained in the absence of misalignment, and those obtained in the absence of ball errors. For each case, the simulation was repeated 10 times for N values of 50, 100, 200, and 300, so that both a mean and standard deviation could be computed. The standard deviation observed for a specific value of N gives us uncertainty bars for our plots to carry out a more rigorous comparison with a model. Creath and Wyant showed, using statistical error analysis, that the standard deviation uncertainty (u_c) of the rms result of the RBT (the rms result is simply the rms value of the

final averaged surface) depends on the rms of the form error on the calibration artifact and decreases as the inverse of the square root of the number of patches averaged [51]; or

$$(21) \qquad u_c = \frac{\sigma_{ball}}{\sqrt{N}}.$$

We plotted the rms result versus $1/\sqrt{N}$ for each case outlined above, and observed that each case described a nearly linear trend with varying slope. One can see that as N increases, the rms of the RBT result approaches the actual system bias rms (B = 0.2215 waves) that we prescribed by adding 0.25 waves of spherical aberration into our ZEMAX model. We also observed that both misalignment and ball form error impact the apparent linearity of the data.

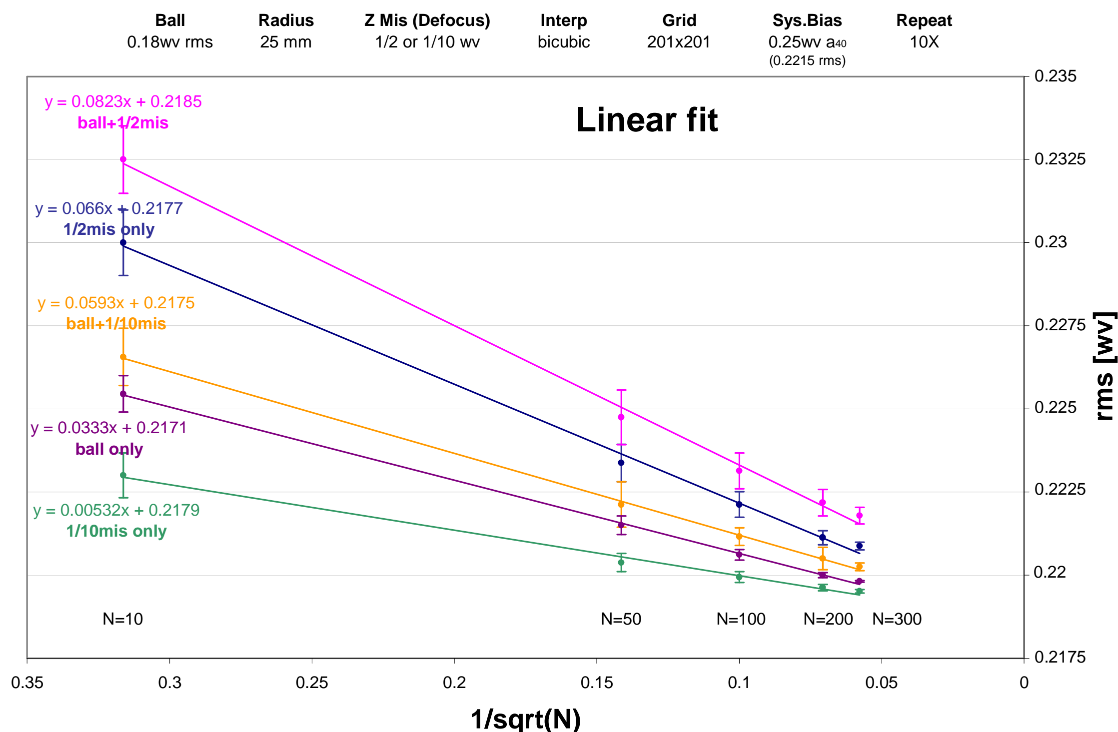

Figure 54. R = 25 mm; plot of rms versus the inverse square root of the number of maps averaged (N). Plot shows resulting rms values converging to the actual system bias for various test conditions in apparent linear fashion. Each data point is the average of ten measurements. The

term 'ball' implies 0.18 wv rms form error on ball, '1/2mis' implies misaligning the ball by ½ wave along the optical axis, and '1/10mis' is 1/10 wave of misalignment.

We began with a postulation that the data was linear when plotted versus $1/\sqrt{N}$:

$$(22) \qquad \sigma_{bias} = \frac{A}{\sqrt{N}} + B \ ,$$

where the slope, *A*, of the line is approximately equal to some combination of σ_{mis} and σ_{ball} and *B* is the system bias in the limit of large *N*. This model appears consistent with the simulated data with uncertainty bars, however, there is a systematic difference between the simulated data and the linear model that suggests the model is only approximate. We looked to a theoretical analysis to investigate the relationship in more detail.

Based on the concepts surrounding the RBT, we know that an estimate of the instrument bias map can be generated by averaging *N* surface form measurements of a smooth calibration ball. The ball surface used to do the averaging does not need to be extremely spherical, but the more spherical it is, the fewer measurements are needed for the average. Once the estimate of the instrument bias map is obtained, it can then be subtracted from subsequent measurements of a test lens surface.

We begin with the reasonable assumption that one measurement in the collection of *N* measurements can be written as [51]:

(23) *single meas(x)*$_i$ = *actual ball form error(x)*$_i$ + *act. ball misalignment(x)*$_i$ + *act. instr. bias(x)*

or

$$(24) \qquad meas(x)_i = ball(x)_i + mis(x)_i + bias(x)_{actual} \ .$$

This equation is for a single pixel x on the *ith* surface map where i varies from 1 to N. The instrument bias estimate $bias(x)_{estimate}$ is given by

$$(25)\ bias(x)_{estimate} = \langle meas(x)_i \rangle_i = \frac{1}{N}\sum_{i=1}^{N} meas(x)_i = \frac{1}{N}\sum_{i=1}^{N}\left[ball(x)_i + mis(x)_i + bias(x)_{actual}\right]$$

where each pixel x on the ball map is averaged over N separate measurements of the surface. Performing this averaging on each pixel allows us to build up a surface map of our bias estimate. We need to connect this bias estimate with the rms of the resulting bias estimate which is what is plotted in Figure 54 versus N. Thus, we begin by calculating the variance of the data over the collection of pixels on this averaged map. This can be written as

$$(26)\quad \left\langle bias(x)^2_{estimate} \right\rangle_x = \left\langle \left[\frac{1}{N}\sum_{i=1}^{N}\left[ball(x)_i + mis(x)_i + bias(x)_{actual}\right]\right]^2 \right\rangle_x ,$$

but this time, the angle brackets indicate an average over x (all the pixels on one map), and we have assumed that all the variables have zero mean in x. Distributing the average over N through to each term and carrying out the square multiplication, we obtain the following:

$$(27)\quad \left\langle bias(x)^2_{estimate} \right\rangle_x = \Bigg\langle \Bigg[\left(\frac{1}{N}\sum_{i=1}^{N} ball(x)_i\right)^2 + \left(\frac{1}{N}\sum_{i=1}^{N} mis(x)_i\right)^2 + \left(\frac{1}{N}\sum_{i=1}^{N} bias(x)_{actual}\right)^2 +$$

$$\cancel{2\left(\frac{1}{N}\sum_{i=1}^{N} ball(x)_i\right)\left(\frac{1}{N}\sum_{i=1}^{N} mis(x)_i\right)} + \cancel{2\left(\frac{1}{N}\sum_{i=1}^{N} ball(x)_i\right)\left(\frac{1}{N}\sum_{i=1}^{N} bias(x)_{actual}\right)} +$$

$$+ \cancel{2\left(\frac{1}{N}\sum_{i=1}^{N} mis(x)_i\right)\left(\frac{1}{N}\sum_{i=1}^{N} bias(x)_{actual}\right)} \Bigg] \Bigg\rangle_x .$$

The ball surface error contributions and misalignments are independent, uncorrelated, and identically distributed. Consequently, cross terms resulting from the squaring operation

are uncorrelated, likely small, and therefore ignored. This follows because it is equally likely to have positive and negative average contributions from the misalignment and the ball contribution on individual pixels. Next, given that the system bias does not vary between the *N* maps, the variance equation reduces to the following:

$$\text{(28)} \quad \left\langle bias(x)^2_{estimate} \right\rangle_x = \left\langle \left[\frac{1}{N} \sum_{i=1}^{N} ball(x)_i \right]^2 \right\rangle_x + \left\langle \left[\frac{1}{N} \sum_{i=1}^{N} mis(x)_i \right]^2 \right\rangle_x + \left\langle bias(x)^2_{actual} \right\rangle_x$$

Again, the ball surface error contributions and misalignments are uncorrelated between the *N* measurements, with equally-likely positive and negative values for each measurement, therefore the cross-terms of these squaring operations also lead to negligible cross terms and we have

$$\text{(29)} \quad \left\langle bias(x)^2_{estimate} \right\rangle_x = \frac{1}{N^2} \sum_{i=1}^{N} \left\langle ball(x)^2 \right\rangle_x + \frac{1}{N^2} \sum_{i=1}^{N} \left\langle mis(x)^2 \right\rangle_x + \left\langle bias(x)^2_{actual} \right\rangle_x$$

or

$$\text{(30)} \quad \left\langle bias(x)^2_{estimate} \right\rangle_x = \frac{1}{N} \sigma^2_{ball} + \frac{1}{N} \sigma^2_{mis} + \sigma^2_{bias_actual} \; ,$$

where the σ^2 terms are defined to be the expected variance over all pixels for a single measurement. Re-writing in terms of rms, we obtain the following for the rms result of the RBT:

$$\text{(31)} \quad \sigma_{bias_estimate} = \sqrt{\left(\frac{\sigma_{ball}}{\sqrt{N}} \right)^2 + \left(\frac{\sigma_{mis}}{\sqrt{N}} \right)^2 + \sigma^2_{bias_actual}} \; ,$$

or

$$\text{(32)} \quad \sigma_{bias_estimate} = \sqrt{\left(\frac{\sigma^2_{ball} + \sigma^2_{mis}}{N} \right) + \sigma^2_{bias_actual}} \; .$$

The σ_{ball} term can be estimated in the simulation, it is simply the rms of the ball form errors. To estimate σ_{mis} for the simulation, we prescribe a perfect ball, specify a system bias and choose a misalignment of 1 sigma, and after one ray-trace iteration we read-off the resulting rms of the output wavefront and use this value as an estimate of our σ_{mis}.

Equation 32 for the rms result of the RBT reveals a non-linear relationship between $\sigma_{bias_estimate}$ and *N*. We now return to our simulated rms RBT result data and compare it to this model. To do this, we performed a chi-square minimization to the model by finding the best-fit variables σ_{ball}, σ_{mis} and σ_{bias_actual} in equation 32 for the data. The best-fit model curves are shown in Figure 55. The best-fit model parameters are close to our estimated model parameters (estimated from the simulation input parameters).

We carried out a chi-square test to more rigorously investigate the goodness of the fit. In general, the X^2 test evaluates statistically significant differences between proportions for two or more groups in a data set. Thus, the chi-square statistic is the sum of the square of the distances of the simulated data points from the model curve, divided by the predicted standard deviation at each value of *N*,

$$(33) \qquad \chi^2 = \sum_{i=1}^{k} \frac{(y_i - y)^2}{\sigma_i^2}.$$

The X^2 statistic indicates the likelihood that our model (Equation 32) provides a good fit to our simulated (or later experimentally) data, given the uncertainty in the data. If the model is correct then on average each term in the sum of equation 33 is one. Since each curve corresponds to 5 data points (for 5 values of *N*), and we are estimating two

parameters, the calculated χ^2 value may be tested against the chi-square distribution with

$$(34) \quad k - 1 - p = (5 - 1) - 2 = 2 \text{ degrees of freedom} .$$

For this distribution, the critical value for a 0.05 significance level is 5.99.

We have simulated RBT rms result values for the large radius case (case I: R = 25 mm; lower curves in Figure 55), as well as the micro-optic case (case II: R = 1 mm; upper curves in Figure 55). Across the board, the simulation converged to a higher overall system bias rms value for the case where a 1 mm radius ball was used. The data points correspond to RBT rms results, while the curved lines represent the fit to the model. Model fit variables and the actual simulated data are also listed in Table 3.

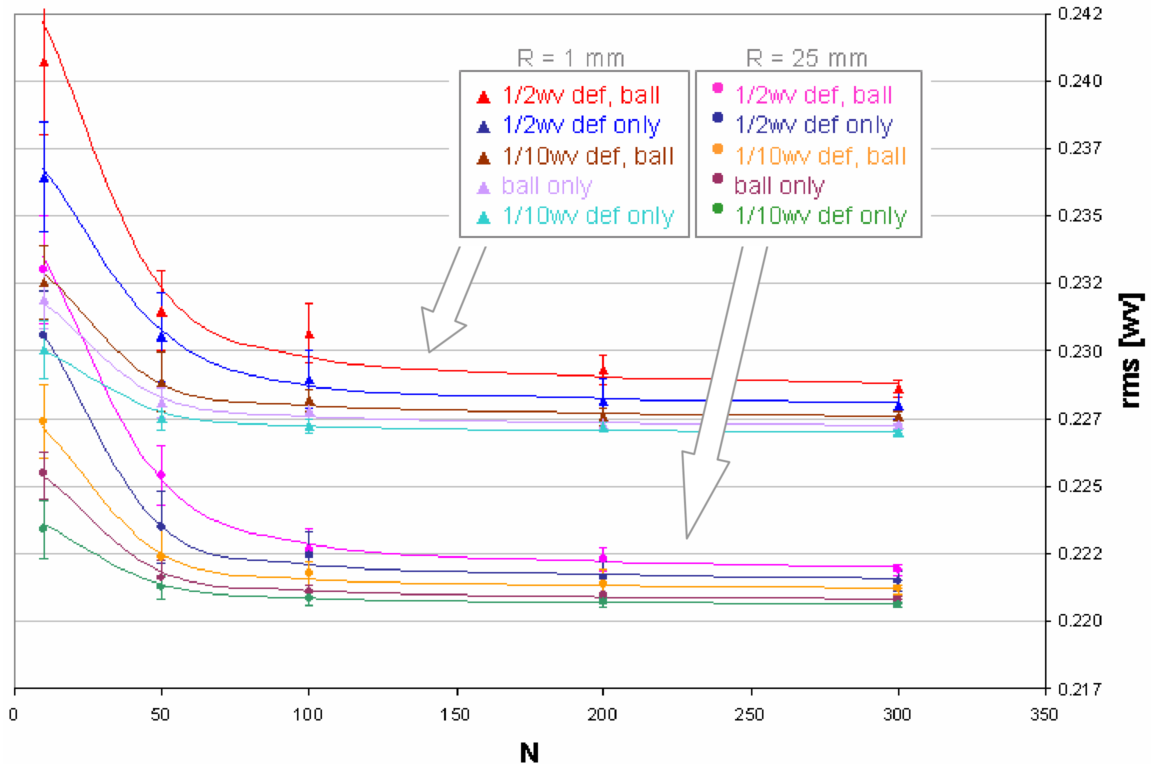

Figure 55. Chi-square minimization of mean values to the model, plotting rms RBT result versus number of maps averaged, *N*. The term '1/2wv def' implies misaligning the ball by max ½ wave along the optical axis, '1/10wv def' implies max 1/10 wave misalignment and 'ball' implies 0.18 waves rms surface form on the ball.

		misalignment		ball surface		system bias		chi square
		rms mis sim data	rms mis fit	rms ball sim data	rms ball fit	rms bias sim data	rms bias fit	
1 mm	1/2 wv def, ball	0.2677	0.2515	0.1800	0.1728	0.2279	0.2254	2.08
	1/2 wv def only	0.2677	0.2604	0.0000	2.5E-08	0.2279	0.2266	1.14
	1/10 wv def, ball	0.0784	0.0719	0.1800	0.1743	0.2279	0.2273	1.53
	ball only	0.0000	-7.3E-08	0.1800	0.1797	0.2279	0.2269	1.66
	1/10 wv def only	0.0784	0.0748	0.0000	-1.4E-07	0.2279	0.2278	0.95
25 mm	1/2 wv def, ball	0.2668	0.2567	0.1800	0.1828	0.2215	0.2220	1.39
	1/2 wv def only	0.2668	0.2599	0.0000	2.6E-09	0.2215	0.2201	1.22
	1/10 wv def, ball	0.0770	0.0752	0.1800	0.1822	0.2215	0.2205	1.58
	ball only	0.0000	-2.9E-08	0.1800	0.1813	0.2215	0.2207	1.13
	1/10 wv def only	0.0770	0.0763	0.0000	1.6E-08	0.2215	0.2211	1.44

Table 3. Model fit variables compared with actual simulated values; chi square statistic for each case; rms values in waves. The term '½ wv def' implies a max ball misalignment of ½ wave along the optical axis, '1/10 wv def' implies max 1/10 wave misalignment and 'ball' implies 0.18 wv rms form error on the ball. The term 'sim data' refers to a predicted rms value, while 'fit' implies the (actual) resulting rms value following minimization.

Our chi square value for each case is less than 5.99, supporting the use of this model at the current level of uncertainty in our simulation.

Evidently, the actual system bias rms (convergence of the curves) changes considerably as we move from a large radius ball to a 1mm radius ball. Based on the retrace error simulation, we expect even more change as we select radii less than 1 mm. For the 1 mm case, the functions converge to a bias of 0.2279 waves rms, while the 25 mm curves approach 0.2215 waves rms. It can also be interesting to re-write equation 32 and graph the mean squared (ms) data as follows:

$$(35) \qquad \sigma^2_{bias_estimate} = \left(\sigma^2_{ball} + \sigma^2_{mis}\right)\frac{1}{N} + \sigma^2_{bias_actual} \quad .$$

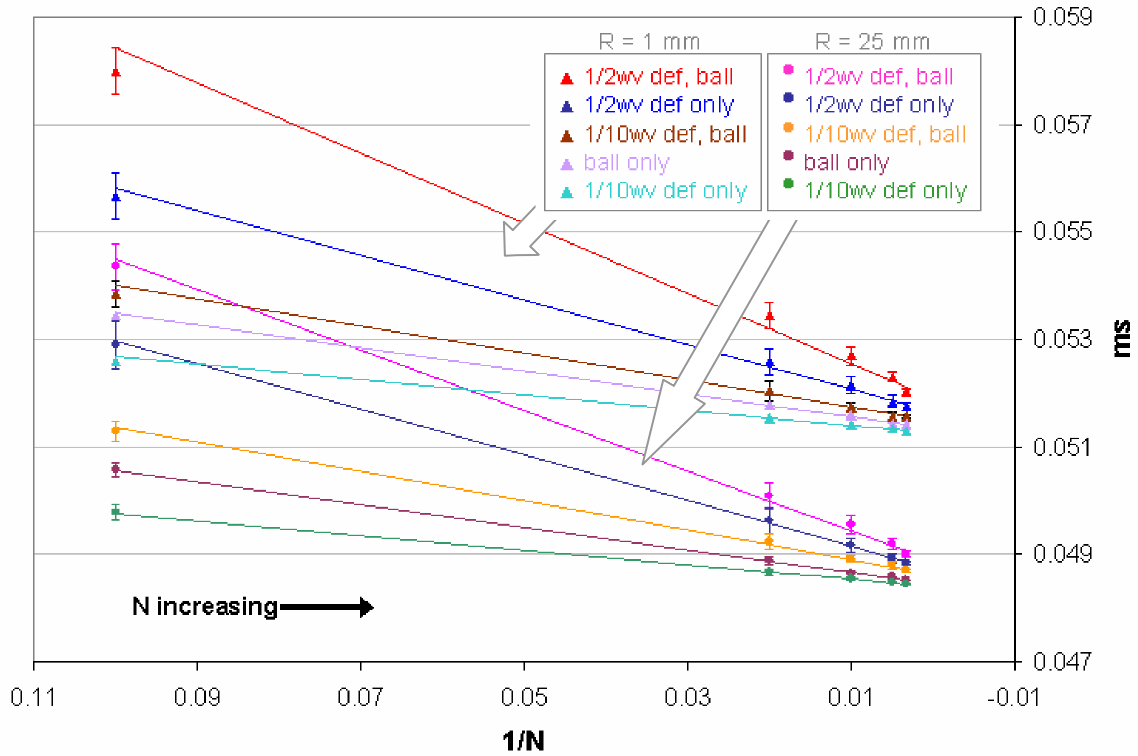

Figure 56. Chi-square minimization to the model for mean values; assuming y is ms and x is 1/*N*. The term '½ wv def' implies a max ball misalignment of ½ wave along the optical axis, '1/10 wv def' implies max 1/10 wave misalignment and 'ball' implies 0.18 wv rms form error on the ball.

Steeper slopes mean that it takes longer (averaging more maps) to approach the actual bias result. Here, the square of the actual system bias rms changes strongly with misalignment for the smaller radius ball. The linear convergence slopes appear similar in comparing the 25 mm case to the 1 mm case, however the overall increase in slope from the bottom curve to the top curve was greater for the 1 mm ball (case II). The relative increase of the bias value between cases can also be noted, and considering $N = 100$ for the *½ wave misalignment + ball* line versus the *ball only* line, case I revealed a percent increase of 0.7 percent while case II showed an increase of 1.3 percent. The largest deviation from the model is observed when simulating the 1 mm ball and the largest

amounts of misalignment. Given the severity of the retrace error effect in the micro-optic range (high surface curvature), it is not surprising that our simulated data begins to deviate from the model. An exponential increase in system bias for radii less than 1 mm could yield unpredictable results given our chosen model. More work is needed to clarify the nature of the departure from the model for smaller radii.

In summary, based on the model, using the best quality ball and least misalignment will result in the need for fewer measurements to approach the best estimate of the system bias. Assuming that most available calibration balls will be of medium quality (as prescribed in the simulation), the data also reveals that decreasing the ball misalignment from ½ to 1/10 wave reduces the required number of measurements (N) by approximately one third to achieve the same estimate.

Based on the error-propagation equation, we can also find the uncertainty in the "averaged" estimate by describing the standard deviation at each pixel [30]:

(36)

$$\sigma_{bias_estimate} = \sqrt{\left(\frac{\partial\langle meas(x)_i\rangle_x}{\partial ball(x)_i}\sigma_{ball}\right)^2 + \left(\frac{\partial\langle meas(x)_i\rangle_x}{\partial mis(x)_i}\sigma_{mis}\right)^2 + \left(\frac{\partial\langle meas(x)_i\rangle_x}{\partial bias(x)_{actual}}\sigma_{bias_actual}\right)^2}$$

where the angle brackets again indicate an average over x. The ball measurements are still assumed to be uncorrelated and identically distributed. Also, all of the partial derivatives give the same result ($1/N$), the summation yields a factor of N and the actual instrument bias is unchanged for each measurement (i.e. the $bias(x)_{actual}$ term drops off) yielding the uncertainty result (u_c),

$$u_c = \sqrt{N\left(\frac{1}{N}\sigma_{ball}\right)^2 + N\left(\frac{1}{N}\sigma_{mis}\right)^2} \quad (37)$$

or

$$(38) \qquad u_c = \sqrt{N \frac{1}{N^2}\left(\sigma_{ball}^2 + \sigma_{mis}^2\right)} = \sqrt{\frac{\sigma_{ball}^2 + \sigma_{mis}^2}{N}} \ .$$

Hence, the uncertainty equation can be rewritten in terms of standard deviation (or rms),

$$(39) \qquad u_c = \frac{\sqrt{\sigma_{ball}^2 + \sigma_{mis}^2}}{\sqrt{N}} \ ,$$

where σ_{ball} is the rms of the form error on the calibration ball, and σ_{mis} is the rms of the ball misalignment. Note that this equation does not depend on the specific probability distribution of the individual random variables.

Also, a standard deviation based pixel-by-pixel uncertainty map for a given RBT calibration can be computed as seen in Figure 57.

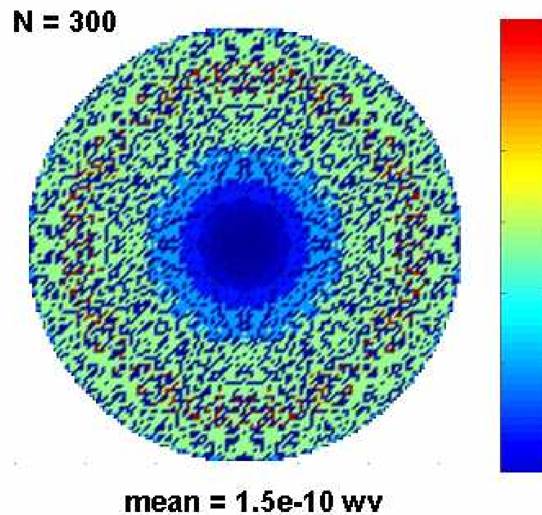

Figure 57. RBT simulation uncertainty map for an average of 300 maps using a 0.18 wv rms ball form error and 1/10 wv of defocus misalignment.

The uncertainty map for an average of 300 maps using an imperfect ball, a maximum of 1/10 wave of defocus misalignment and 0.25 waves of spherical aberration (system bias), reveals some residual spherical aberration. Given that positively and negatively defocused spherical aberration maps appear as the inverse of each other, we can conclude that applying random amounts of z misalignment to the simulated RBT and inputting spherical aberration as the system bias, lead to a near-zero mean misalignment result and residual spherical aberration. Figure 58 illustrates positively and negatively defocused interferograms in the presence of spherical aberration.

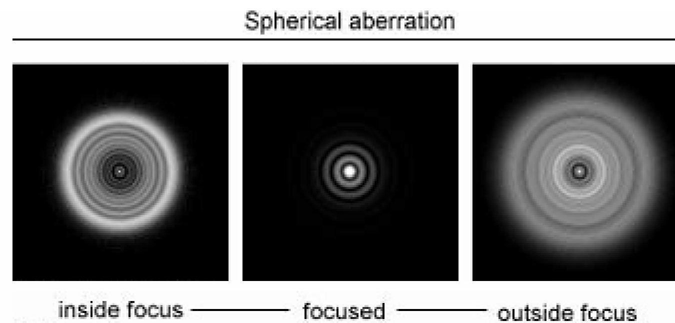

Figure 58. Spherical aberration and defocus [36].

In a physical experiment, we would expect more variation in the uncertainty map, given that a real-life calibration would be subject to other noise sources.

We also examined alignment sensitivity of the model by executing a systematic misalignment test, and discovered that we could essentially predict the residual aberrations in the result of a random ball test with a simple initial alignment-sensitivity test. To demonstrate this, we vary defocus (a_{20}) in the simulation over a range and plot the resulting spherical aberration (a_{40}). The resulting plot, as seen in Figure 59, describes a linear relationship and equation that we use to predict a_{40}. Using a perfect ball (R = 25 mm), no system bias, N = 60 and a maximum magnitude of ½ wave of random

misalignment in the z-direction (along the optical axis), we ran an RBT for comparison. The RBT reveals a residual a_{20} value of -0.0352 waves and an a_{40} of 0.0004 waves. Using the equation defined by the systematic misalignment, we insert -0.0352 waves for a_{20} (or 'x') and obtain a residual a_{40} (or 'y') of 0.0003 waves. Hence, an alignment sensitivity test is effective in predicting residual system aberrations due to misalignment contributions without the need for repeated averaging by the RBT simulation.

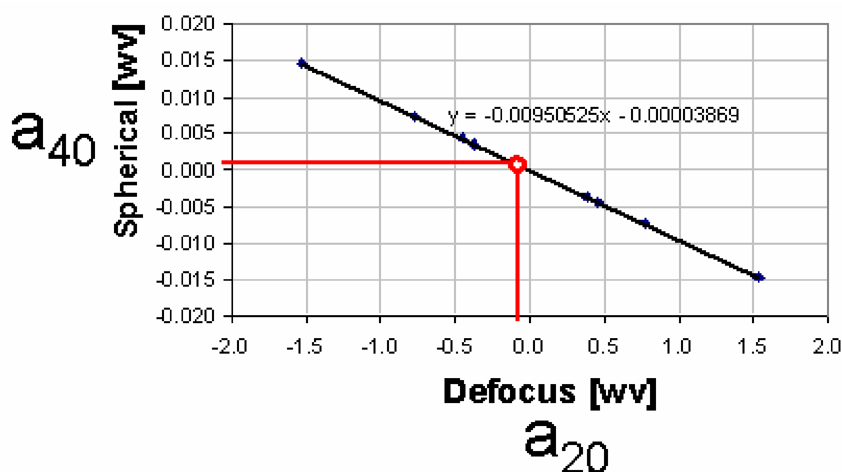

Figure 59. Plot of spherical aberration versus defocus for a systematic misalignment test for R = 25mm.

Furthermore, the systematic misalignment test can also be applied to predict the residual rms wavefront bias of the optical system, as seen in Figure 60. Prescribing B = 0.2215 waves of rms bias to our ZEMAX model, we again vary defocus (a_{20}) in a controlled fashion over a range and, this time, plot the residual rms. While the relationship is not linear, we can still arrive at a relatively unbiased prediction of the rms error. The red line indicates that for perfect alignment, the rms residual is equal to the added system bias. Realistically, in an experimental setting, the rms bias value for

perfect alignment includes ball and system bias, and consequently, isolation of the system bias is impossible without RBT averaging.

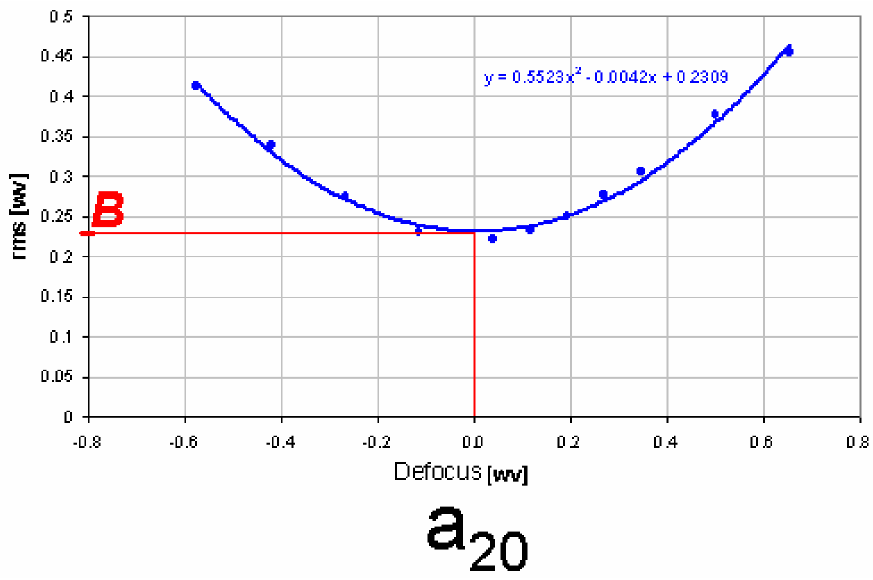

Figure 60. Plot of the resulting rms versus defocus for alignment sensitivity test of R = 25 mm.

CHAPTER 5: EXPERIMENTAL SETUP AND RESULTS

5.1 Retrace Error Effect

The RBT exploits the symmetry properties of a micro-sphere, resulting in a low-uncertainty estimate of the instrument biases of MORTI. By measuring a collection of random patches on the surface of this spherical calibration artifact and then averaging the results, the contributions from the sphere go to zero leaving only the systematic biases due to the instrument. Careful selection of this spherical calibration artifact is required, however. It is important to select a calibration ball with a high enough surface quality so as to end up with the desired calibration uncertainty. Accordingly, we tested several 1 mm balls and chose the one with the lowest RMS form error so as to minimize the number of measurements required. The surface finish and form errors are strongly dependent on the ball material and grade. Poor surface finish causes data dropout in the measurements and must be avoided. We used the highest grade (“3”, rms form error = 100 nm = 0.15 wv) of hardened stainless steel micro-sphere for our random ball tests. Small pits in the surface led to some data dropout, but bad pixels were not propagated through the average and it yielded acceptable results. It is also important to use an opaque micro-sphere, particularly for a phase-shifting interferometer calibration, to avoid stray light reflections from the back surface of the sphere. All of the micro-spheres were obtained through the *Bal-tec*™ company, and balls of varying radii can be seen in Figure 61.

Figure 61. 440-steel micro-spheres; radii 0.5 – 3 mm [52].

Random re-positioning of the ball between measurements is another crucial aspect. The key is to randomly bump for re-orientation and then replace the micro-sphere in its original measurement position. To do this, we developed a simple fixture that consists of a sandwiched sheet of brass between two large aluminum washers. A small indentation in the center of the sheet provided a reproducible position for the micro-sphere. A small puff of air easily displaced the ball, causing it to roll around inside the fixture before returning to its original center position. Interference fringes re-appear after the ball settles and little realignment is necessary. The room temperature is kept close to 21°C throughout the data gathering process.

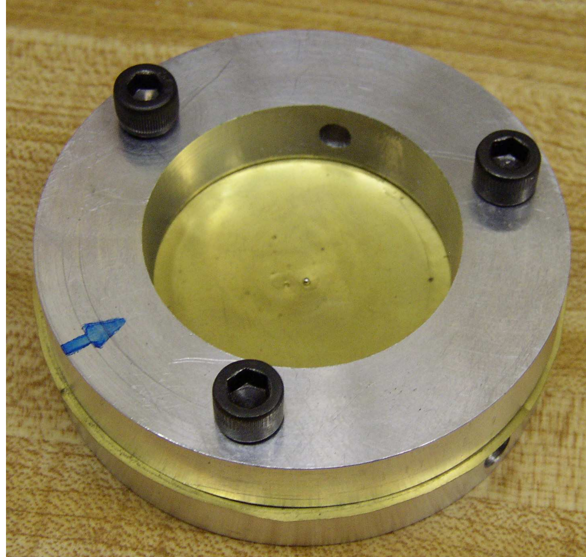

Figure 62. Random ball re-orientation fixture.

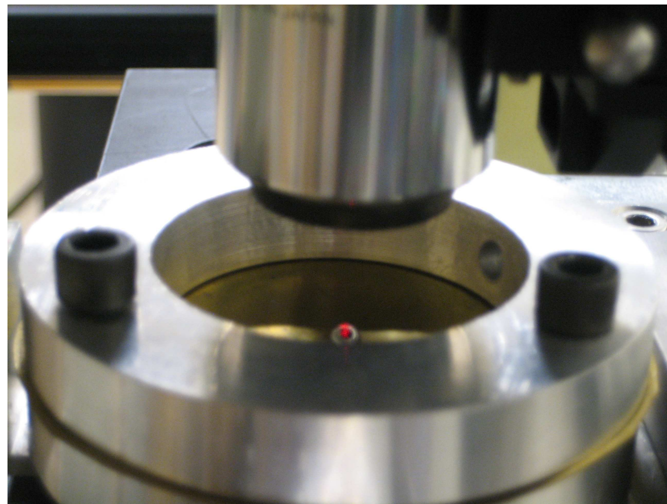

Figure 63. He-Ne beam reflecting from the micro-sphere when positioned at the confocal location.

Recall that in interferometry, a circular and/or tilted fringe pattern is present when the spherical test surface is not perfectly aligned, while only straight fringes are present when testing a nominally flat surface that is slightly misaligned. For the simple case of straight fringes,

$$(40) \qquad height_error = \left(\frac{\lambda}{2}\right)\left(\frac{\Delta}{S}\right) ,$$

where λ is the inspection wavelength, Δ is half the fringe width and *S* is the fringe-center spacing.

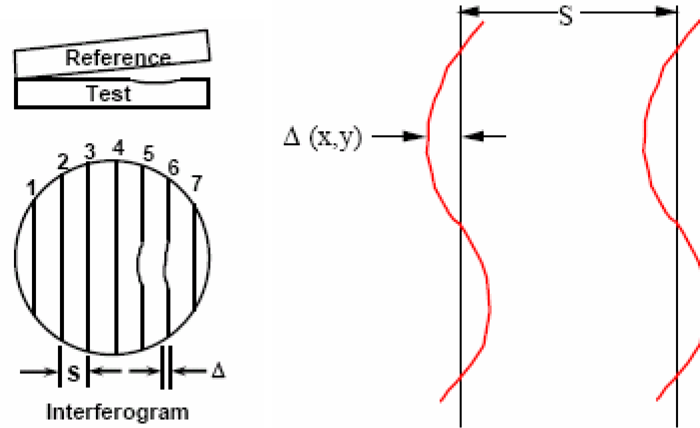

Figure 64. Fizeau fringes.

In our experiment, phase-shifting is used instead of directly calculating fringe deviations. By shifting the phase in increments of π/2 and gathering a few frames of intensity data, we can accurately calculate the height error for a given x, y location using a previously chosen algorithm as follows:

$$(41) \qquad \phi(x,y) = \tan^{-1}\left[\frac{I_4(x,y) - I_2(x,y)}{I_1(x,y) - I_3(x,y)}\right]$$

and

$$(42) \qquad height_error(x,y) = \frac{\lambda}{4\pi}\phi(x,y) ,$$

where ϕ is the phase [35]. Calibration of the phase-shifting device is also important and was tested before beginning the experiments. Obtaining good surface measurements also

requires occasionally adjusting the light intensity to avoid over-saturation, and varying the modulation threshold in software. The He-Ne laser that we are using has a very high spatial and temporal coherence, and allows for good contrast and visibility of fringes. The modulation threshold determines the contrast required for a pixel to be considered valid in the data analysis. To gather the most data in our instrument we set the modulation threshold below 1% in most cases.

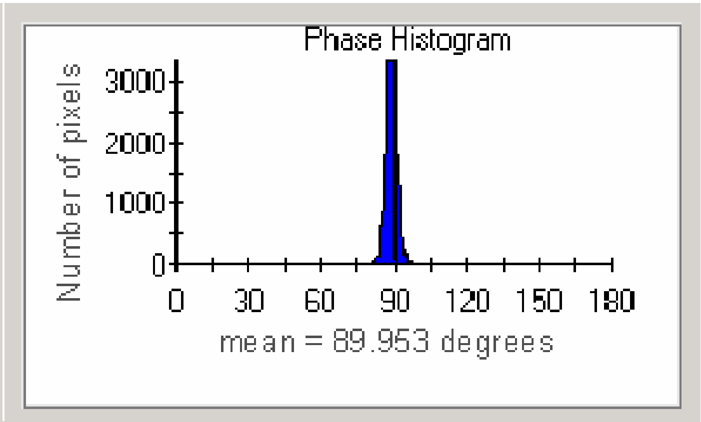

Figure 65. Phase plot obtained during PZT calibration.

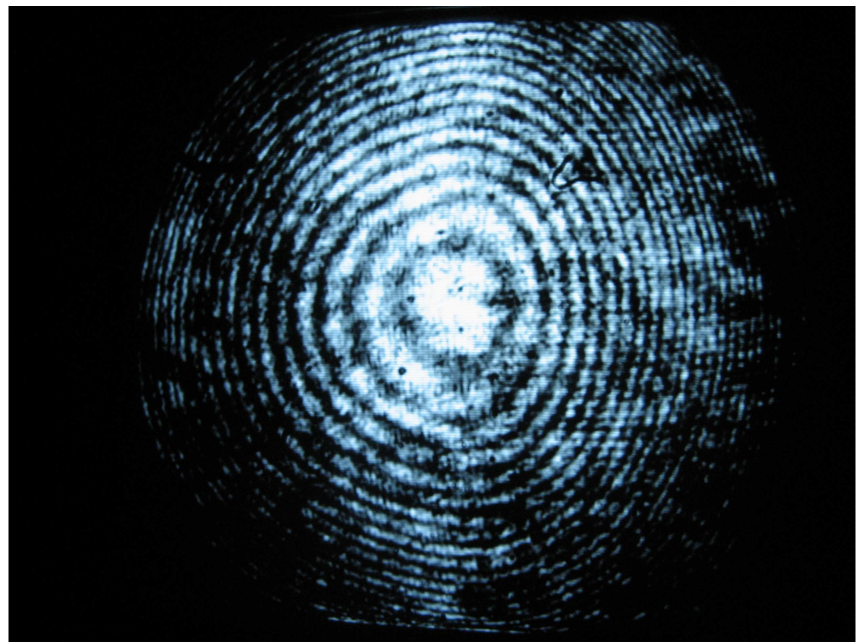

Figure 66. Actual circular fringe pattern from micro-sphere surface.

Following Phase I of construction and alignment of MORTI, initial self-calibration tests were performed using two micro-spheres with different radii. Figure 67 illustrates the RBT calibration result that was obtained using a 1 mm radius sphere, while Figure 68 is the result using a 0.5 mm sphere. As predicted by the simulations, the peak-to-valley instrument wavefront bias is higher for the sphere with the smaller radius. A difference of approximately 300 nm was observed between the two results. The RMS values are 50 nm and 97 nm, respectively. The wavefront maps in Figures 67 and 68 indicate our best estimate of the bias in our instrument.

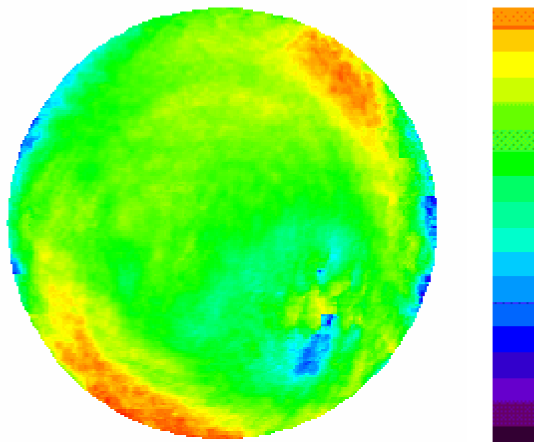

Figure 67. Phase I experimental RBT system bias result using 1 mm radius micro-sphere (PV = 361 nm = 0.57 wv).

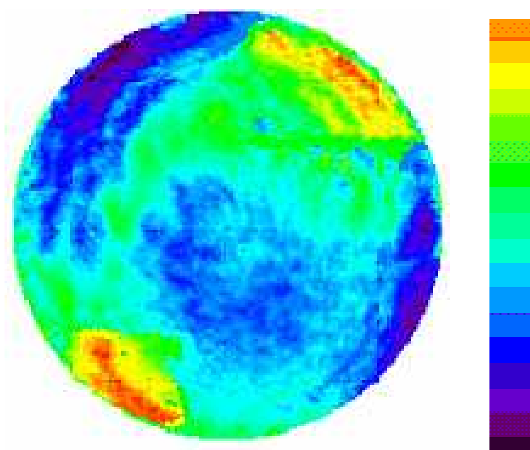

Figure 68. Phase I experimental RBT system bias result using a 0.5 mm radius micro-sphere (PV = 553 nm = 0.87 wv).

These experimental results support the statement that retrace errors significantly affect form error self-calibration at the micro-optic level. Furthermore, calibration should be performed with an artifact of similar radius to that of the micro-lens to be tested. Some measurements traditionally used for precision metrology of large-scale components can be simply extended to the micro regime; however the properties or systems that can be measured are limited and measurement uncertainties are often inadequate. For a qualitative assessment of the RBT wavefront bias, we can fit the data to Zernike polynomials which emphasizes the low spatial frequency contributions, as seen in Figures 69 and 70.

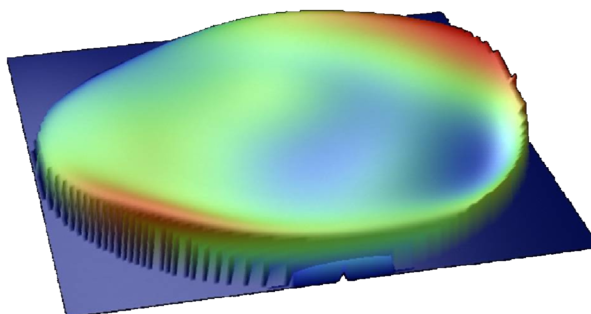

Figure 69. Experimental RBT result Zernike generation for R = 1 mm.

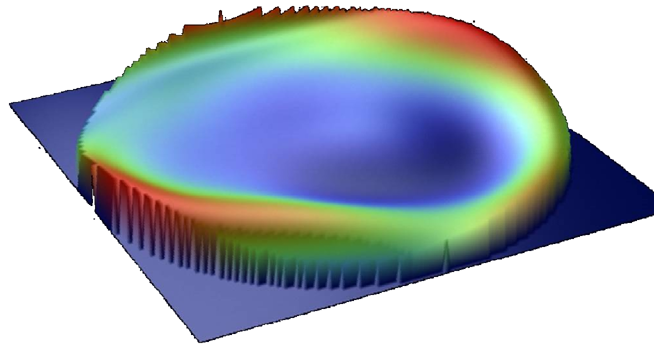

Figure 70. Experimental RBT result Zernike generation for R = 0.5 mm.

The dominant aberrations are more visible in these images, and judging by the maps, coma and astigmatism appear to dominate. Coma is diagnosed based on examining the central region of the maps, and observing that, overall, one half of the map appears high (green) while the other appears low (blue). This aberration is encountered with off-axis propagation through an optical system, which occurs when the optical system is out-of-alignment. Examining the edge regions of the maps, the two high-sloping regions (red) coupled with the pair of low regions (green) show the presence of astigmatism. Recall that astigmatism is said to be present if an optical system is not axisymmetric, either due to an error in the shape of the optical surfaces or to non-optimal alignment of the components. A faint circular pattern in the maps also implies the presence of some spherical aberration in the system. Comparing one map to the other, the aberrations appear to be more extreme for the case where the smaller radius ball was used. For further diagnosing, one could also examine the coefficients of the Zernikes to identify the major players in the aberration map.

The retrace errors and their sensitivity to surface curvature obviously impact the system bias. Retrace errors will also impact radius of curvature measurements [43]. Radius measurements require the identification of an interferometric null position when the lens under test is at two positions - the confocal position where the radius of curvature of the test lens coincides with the focus of the spherical wavefront exiting the interferometer and the cat's eye position where the wavefront retro-reflects from the surface of the lens. Aberrations in the interferometer and retrace errors introduce a bias in the apparent location of these two positions. The same simple ray-trace simulation can be used to explore the order of magnitude of these effects. Again, errors in the measurement become significant in the micro-optic regime.

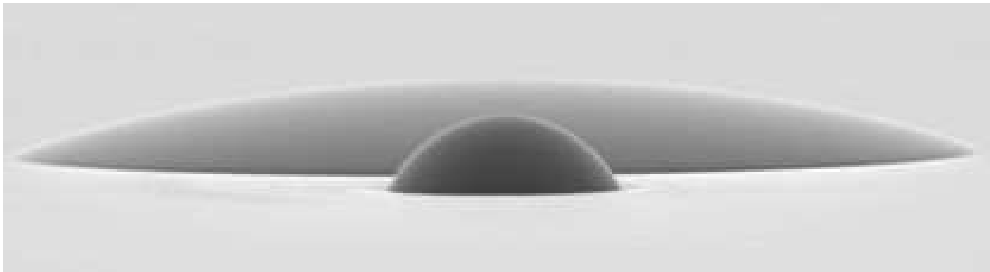

Figure 71. SEM photo of micro-lenses of various ROC [53].

5.2 Effects of Misalignment on MORTI

There are many parameter combinations that can be tested with our simulation. We chose a set of parameters to emphasize the dependence of calibration on misalignment during the RBT and on test surface curvature. Previous published work on the RBT only considers the effect of the ball form error on the convergence rate of the calibration procedure [34]. Our simulation demonstrates that misalignment of the ball

along the optical axis as small as 1/10 wave has a significant effect on the calibration result, even when simulating a perfect spherical artifact. During Phase II of alignment and calibration of MORTI, we demonstrate the misalignment effect by experimentally calibrating the instrument again using a 1 mm radius ball and a 0.5 mm radius ball. We then compare observed trends without simulation results.

For the Phase II calibration, we record the rms bias results and plot this as the number of patch measurements is increased. Each random average of *N* measurements was repeated 10 times to estimate error bars for our analysis. Also, the experimental data is fit to our rms model (Equation 32) using a chi-square minimization process. We include the error bars for this fit analysis to assess the quality of the fit. In the future, we recommend repeating the test to tighten the error bars and arrive at a more rigorous evaluation of the fit to the data.

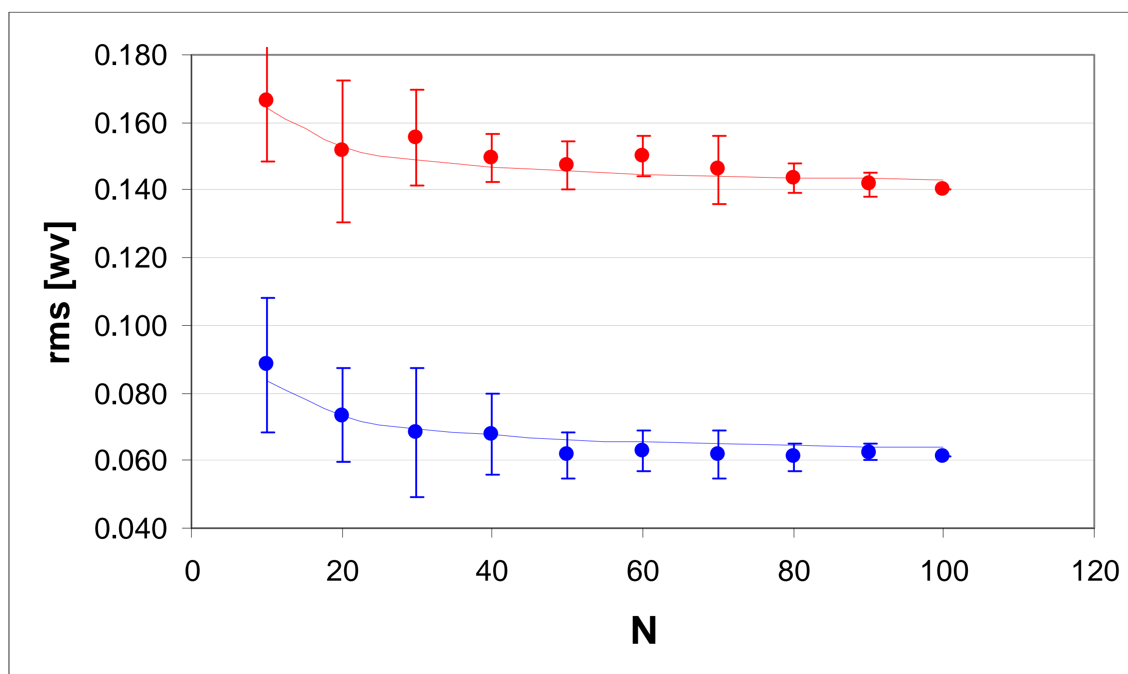

Figure 72. Phase II RBT data for MORTI with 0.5 (red points) and 1 mm (blue points) radii balls.

The fit variables for the experimental data are listed in Table 4. Initial guesses for σ_{ball} and σ_{mis} based on experimental data were used as the starting fit parameter values for the chi-square minimization process. To estimate the rms of the form error on the ball, σ_{ball}, we subtract any two patch measurements to give σ_{diff}. The system bias is the same in any two measurements and therefore cancels with the subtraction, leaving an RMS value that is on average $\sqrt{2}\,\sigma_{ball}$. We can also take several difference maps and average the results to improve the estimate for σ_{ball}. The estimate of σ_{ball} is then

$$\sigma_{ball} = \frac{\langle \sigma_{diff} \rangle}{\sqrt{2}} \quad . \tag{43}$$

The initial estimate for σ_{mis} is based on the decision that, in nulling the fringes for the confocal measurement, we will allow no more than one visible fringe (which translates to 1/10 wave of defocus misalignment) to be visible. We estimate that this results in approximately 0.1 waves rms after the measurement is taken. This is more difficult to clearly estimate compared to the rms of the ball. The variable σ_{bias_actual} is estimated by taking the rms result of the average of all 100 maps.

	misalignment		ball surface		system bias		
	rms mis exp	rms mis fit	rms ball exp	rms ball fit	rms bias exp	rms bias fit	chi square
R = 0.5 mm **1/10 wv def, ball**	0.1000	0.1165	0.1650	0.´757	0.1405	0.1431	8.14
R = 1 mm **1/10 wv def, ball**	0.1000	0.0910	0.1650	0.´625	0.0315	0.0638	3.85

Table 4. Model fit variables compared with experimental variables; chi square statistic for each case; rms values in waves.

After minimization, the chi square values both fall below the critical value of 14.07 for a 5% significance level and 7 degrees of freedom and the best-fit parameter values are quite close to the independent experimental estimates. Technically, the degrees of freedom may be less here because all the data is drawn from the same set of 100 measurements for different *N* values. This could potentially affect the statistical analysis, and should be studied in future work. Therefore, to the level of our current measurement uncertainties, the fit and therefore model appear to adequately describe the experimental calibration dependence on both misalignment and ball form errors.

As predicted by the simulation and seen in the calibration of MORTI on Phase I, the smaller radius ball results in a different system bias. Also, on average, the error in the knowledge of the best system bias estimate for N = 10 compared with N = 100, increased from 0.02 to 0.03 as the ball size was increased. Figure 73 and 74 are RBT calibration results for both cases, R = 1 mm and R = 0.5 mm.

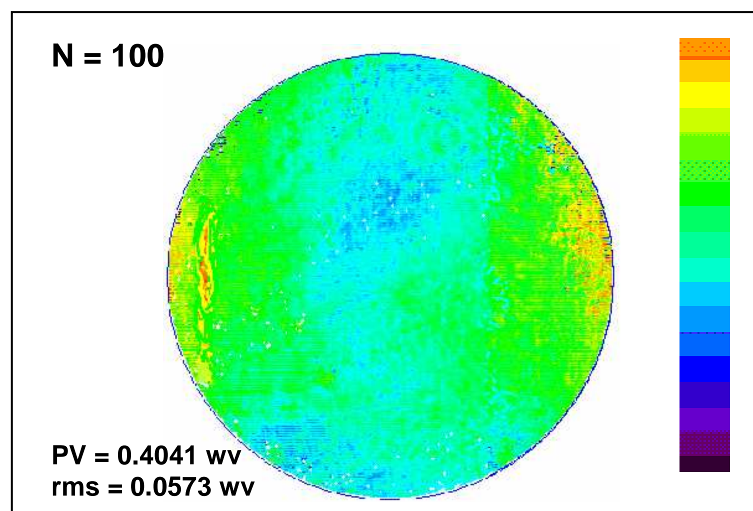

Figure 73. Phase II experimental RBT result for R = 1 mm on MORTI (PV = 256 nm, rms = 36 nm).

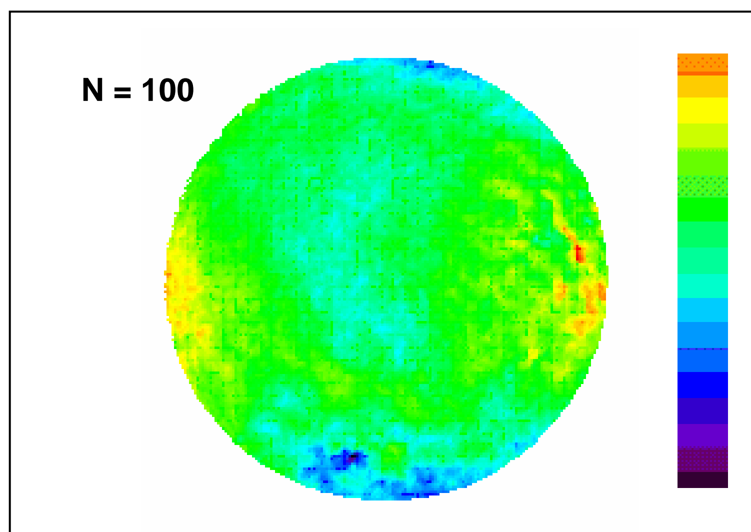

Figure 74. Phase II experimental RBT result for R = 0.5 mm on MORTI (PV = 431 nm, rms = 113 nm).

Several changes to MORTI were made between Phases I and II to improve the quality of the optics and the alignment. For Phase II, the resulting RBT maps again reveal astigmatism as well as some coma aberration, and, as expected, the overall PV and rms values are higher for the smaller radius ball due to retrace errors in testing micro-spheres.

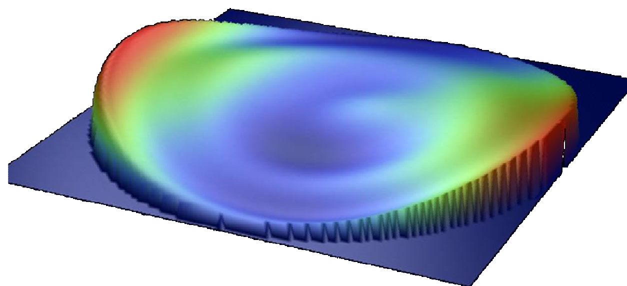

Figure 75. Phase II experimental RBT result Zernike generation for R = 1 mm.

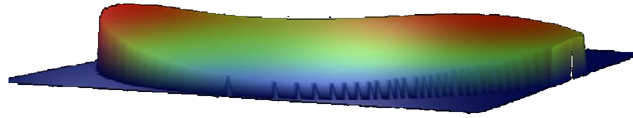

Figure 76. Phase II experimental RBT result Zernike generation for R = 0.5 mm.

Examining these RBT result maps more closely, one can observe that non-axially symmetric aberrations still dominate the system bias, but to a lesser extent than with the Phase I calibrations. Recall that ray-mapping errors are mainly to blame for this type of aberration (coma and astigmatism); therefore MORTI may again be exhibiting beam alignment issues such as light entering and exiting lenses off axis. We expect that spherical aberration would be the dominant aberration caused by the high-quality Mitutoyo objective lens. While spherical aberration is present, it is not dominant and this suggests the system bias is limited by misalignment of the instrument itself, rather than a fundamental limitation from the quality of the objective. It is therefore likely that MORTI's bias can be further reduced through improved alignment.

As in the simulation, we can compute a pixel-by-pixel uncertainty map for our experimental RBT on MORTI. Using N = 100 and the R = 0.5 mm ball, our uncertainty map is seen in Figure 77.

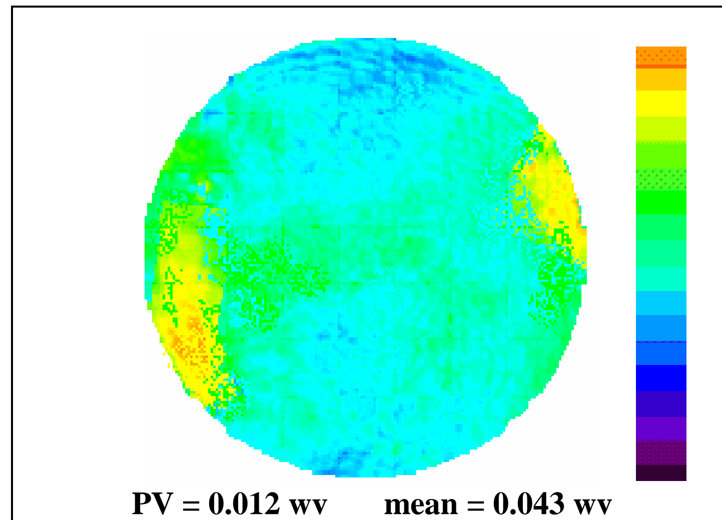

Figure 77. Uncertainty map for R = 0.5 mm on MORTI.

The map shows a mean uncertainty level over the dataset of 0.043 waves (27 nm) and a variation in the uncertainty around this mean with a PV of 0.012 waves (7.9 nm). We find that the uncertainty shows a spatial variation characteristic of astigmatism, as was present in the RBT wavefront bias map. Examining the Zernike polynomials for this uncertainty map shows a small contribution of spherical aberration and coma as well. We can consider either residual ball or misalignment as causes for the spatial variation in uncertainty. If the ball contribution to each patch measurement is truly random, a residual ball contribution would be the same for every pixel, leading to a flat uncertainty map. This may not be true for the misalignment contribution, however. To appreciate this, consider for example only the presence of added spherical aberration with misalignment. Spherical aberration has nodes and antinodes at specific locations. As the amount of spherical aberration randomly varies from random misalignment, the variation at the node locations would be identically zero while the variation would be a maximum at the antinode locations.

The sensitivity of the instrument bias to test part misalignment can be experimentally evaluated by recording measurements as the test part is systematically misaligned. We can then plot, for example, the rms map value versus the Zernike defocus coefficient (a measure of optical axis misalignment). In such a plot, the rms values include contributions from misalignment *and* the form error of the calibration ball. But the shift in rms with misalignment reflects the misalignment dependence. Future work is required to isolate the instrument bias rms from the ball contribution for this type of experimental misalignment test. Ideally, the low point of the curve would correspond to the actual system bias of the instrument, given a perfect calibration artifact.

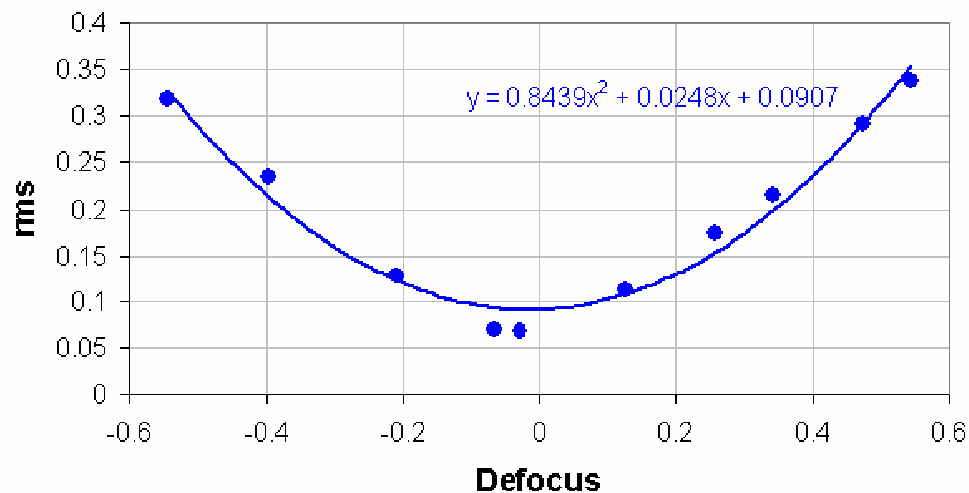

Figure 78. Actual systematic misalignment on MORTI for 1 mm ball

One can also plot Zernike coefficients for the higher order aberrations versus defocus, as shown with the spherical aberration versus defocus shown in Figure 79. This allows for a more detailed assessment and is useful for comparing MORTI to other interferometers.

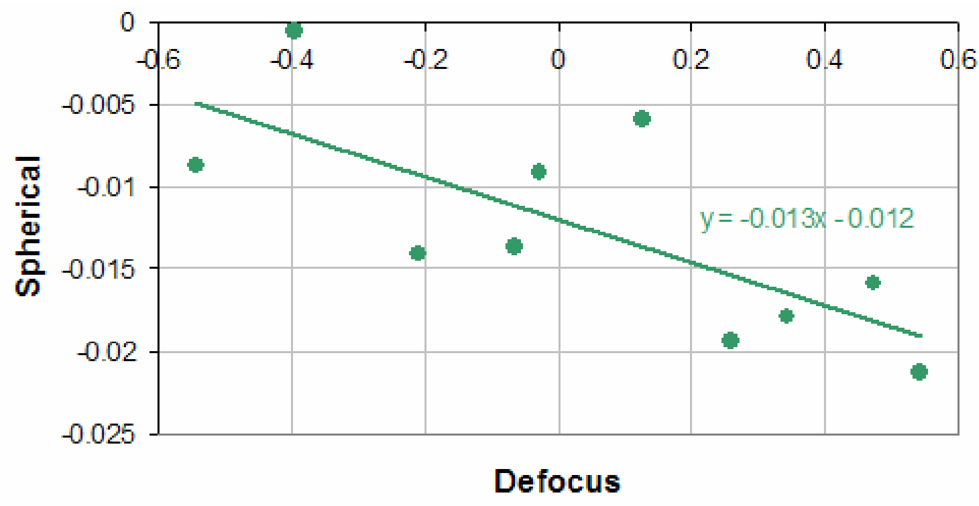

Figure 79. Actual systematic misalignment: defocus versus spherical

Comparing this data with that obtained using a 25 mm ball on the XCALIBIR interferometer from the National Institute of Standards and Technology (NIST) lab, MORTI shows promising results [54]. The slope of a linear fit to the data represents the sensitivity of the interferometer to misalignment. The slope for spherical aberration versus defocus for the XCALIBIR was 0.023, indicating that our custom instrument is less sensitive to optical axis misalignment.

CHAPTER 6: DISCUSSION

In this section, we present several disjoint but noteworthy comments with the purpose of completing (1) an interpretive discussion of how the simulated models performed in comparison with the physical experiments and how our custom instrument performed compared with similar instruments; (2) an argument as to what the various calibration trends convey in light of other optical measurement technologies, how their presence will impact future metrology, and what their drawbacks are; and (3) thoughtful recommendations for implementation of a highly effective RBT calibration technique.

Through simulation, our goal was to gain insight as to which variables are most important to the calibration process, and later verify this in the experiment. The underlying objective was to imitate the internal processes and not merely the results of the RBT. For one, we have demonstrated that retrace errors play a significant role in contributing to the instrument bias for small (less than 1 mm) radii spheres. The simulation plainly showed that for small radii parts, the retrace errors become extremely sensitive to the ball curvature. In extreme cases, retrace errors cause the confocal location to be ill-defined. The calibration ball size must be chosen with care, given the characteristics of the part to be measured. Also, a fixture to hold the ball and a means of random re-orientation must be considered. If care is not taken, the ball could settle into a non-random motion pattern and lead to sampling of the ball surface with a non-uniform

probability density and hence an undesirable bias in the calibration. In future studies, it would be interesting to see how much smaller (nano) calibration balls affect the RBT, but finding smaller balls may be a challenge. One thing is certain, the measurement and inspection of miniature parts will continue to demand new approaches and new technologies in the coming years.

We would have liked to run the RBT calibration experimentally on our custom interferometer repeatedly and ramp up the number of measurements averaged to observe data trends and understand how some variables influence specific phenomena. However, given time constraints, we chose to focus on the importance of ball size and the impact of misalignment, as these had not been studied and we expected them to be important for micro-optics metrology. In the future, it would be beneficial to automate the random ball re-orientation process to average more surface measurements. It is conceivable that the lengthy process of manual calibration may influence the operator to make too few measurements and compromise the calibration, and automation would eliminate this possibility. Previous research involved setting a large ball on a three-point mount and rotating it manually between measurements. This technique is not advisable, as the operator is required to touch the ball and this causes a change in temperature of the ball and possible surface contamination with dust or residue.

Having created and tested our customized RBT simulation model to study misalignment, it became apparent that on top of the susceptibility to retrace errors for small optics, the effectiveness of the RBT is dependent upon several pre-defined system parameters. Clearly, the RBT result will be different for every set of test conditions and recall that we derived the following equation for the rms result of the RBT:

$$(32) \qquad \sigma_{bias_estimate} = \sqrt{\left(\frac{\sigma_{ball}^2 + \sigma_{mis}^2}{N}\right) + \sigma_{bias_actual}^2} \ .$$

Evidently, the rms result of the RBT depends on the rms of the form error of the calibration ball, the rms of the positional z-misalignment of the ball and the number of measurements taken. This relationship shows that fewer measurements are required if σ_{ball} and σ_{mis} are small. Some researchers would argue that removing the defocus (z-displacement) aberration term from each map before averaging eliminates the misalignment contribution. Of course, residual defocus, tip, and tilt in the averaged map represents the amount of pure residual misalignment, but these are not the only consequences of misalignment. Higher order aberrations result from misalignment and these are not removed by simply removing the low-order misalignment Zernike terms. Also, future work is necessary to examine the effects of other misalignment terms such as x-tilt and y-tilt, and how x, y and z positional errors interact.

The question then becomes, how many measurements should be averaged to leave a sufficiently low uncertainty in wavefront bias calibration? In a paper by Ulf Griessman, he suggests that the number of measurements should be large enough so the calibration uncertainty is less than the rms repeatability of the measurement where the ball remains fixed [55]. This certainly is a reasonable target. To estimate repeatability, we take a number of form measurements in a short period of time with the ball in the same orientation, plot the results for the rms of the maps and take the standard deviation of the data. We found that during our experiment, the rms repeatability of MORTI was about 0.002405 waves (~1.5 nm). Comparing MORTI with an in-house Wyko RTI 4100 laser interferometer, we found its rms repeatability was 0.002867 waves (~1.8 nm).

Based on these figures and the simulation values for the RBT (we calculated the difference between the estimated bias for various N and the actual prescribed bias), we recommend collecting at least 100 maps for averaging, but 150 to 200 would be ideal, if time permits. For N = 100, the rms uncertainty in the system bias is 0.002265 waves, while for N = 200, the rms uncertainty is 0.0009 waves. The repeatability data for MORTI and the Veeco are seen in Figures 80 and 81. Given the RBT data from MORTI, we can calculate the difference between the RBT results for various N (choose N = 60 here) and the absolute best estimate value we have (N = 100), for the two different radii cases and estimate an rms uncertainty in the system bias for N = 60 of 0.0054 waves.

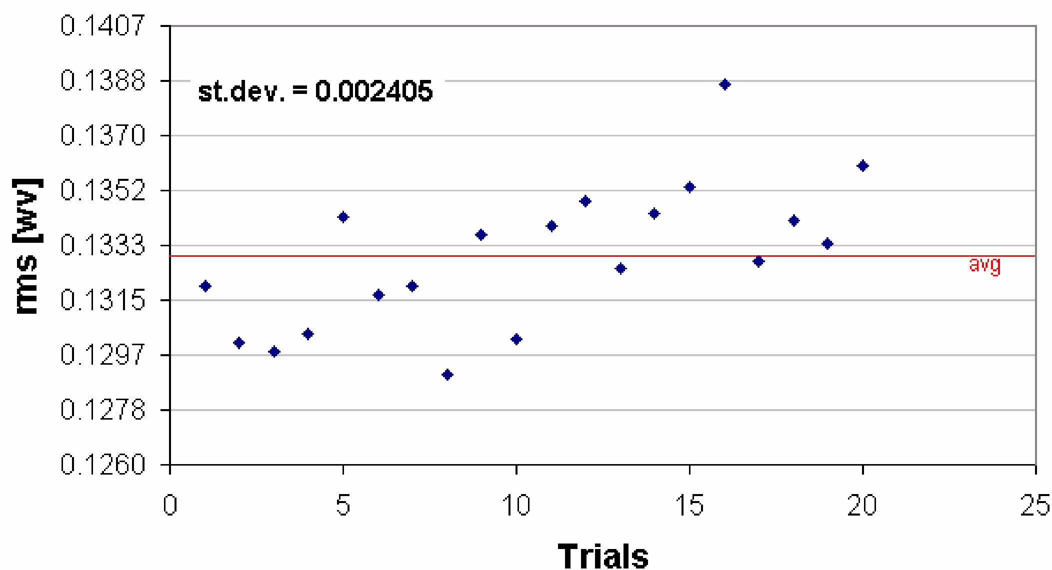

Figure 80. MORTI repeatability.

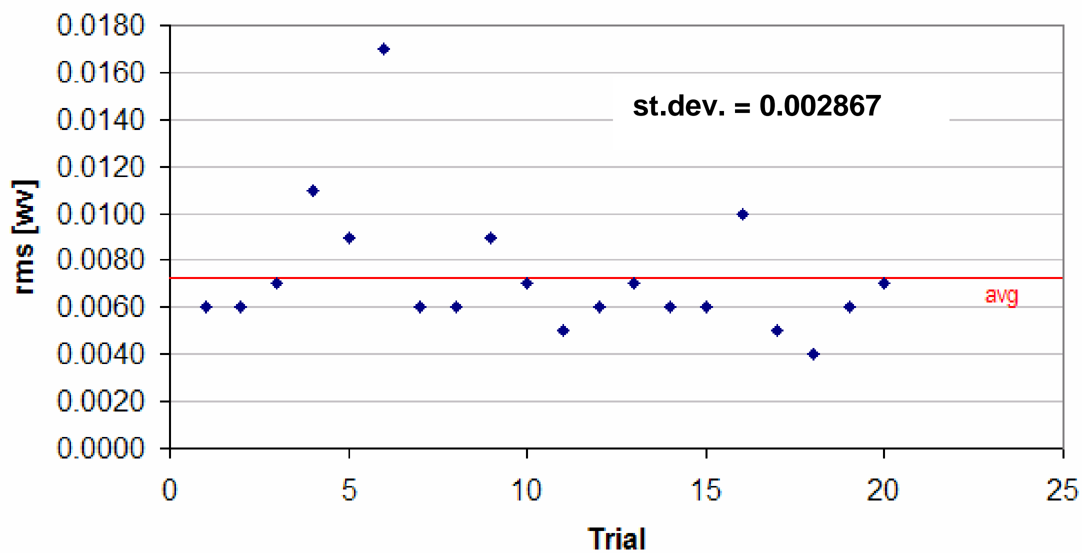

Figure 81. Wyko repeatability.

Figure 82. Wyko RTI 4100 laser Fizeau interferometer.

Traditionally, RBT theory considers the behavior at one pixel and shows that the convergence follows a simple $1/\sqrt{N}$ description. Plotting *rms* vs *N*, our research, and previous work, have shown that the convergence curve deviates from the $1/\sqrt{N}$ behavior as we approach large *N* values. In the past, this was not fully explained, but given our data and our derivation of Equation 32, we can shed light on the tendencies of the random averaging convergence.

Comparing our most recent system bias data from MORTI with that from two commercial interferometers, MORTI was as good or better. Previously, we calibrated a Zygo® Micro-LUPI phase-shifting interferometer and a Zygo NewView 5000 scanning white light interferometer (SWLI) using the RBT technique (R = 1 mm). We found that the Micro-LUPI has a system bias PV value of 211 nm, while the SWLI exhibited a PV of 390 nm for N = 100. RBT results obtained using a 1 mm radius ball on MORTI totaled 361 nm. The NewView 5000 and the Micro-LUPI are pictured in Figures 83 and 84.

Figure 83. Zygo scanning white light interferometer.

Figure 84. Zygo Micro-LUPI phase-shifting interferometer [56].

Caution is implied when using such non-common path interferometers, as the reference and test beams follow widely separated paths and are, hence, differently affected by mechanical vibrations and temperature fluctuations. If the effects are large enough, the fringe pattern can become unstable and measurements will not be possible. Mechanical vibrations and turbulent air flow introduce significant problems for most interferometric test methods. The problem is that data is taken sequentially over a relatively long time period. Commercial interferometers can take four or five frames of data to compute a phase map, which means that the interference pattern must remain stable for almost 200 milliseconds. Using faster cameras, measurements can be made with almost any magnitude of vibration or air turbulence. Although MORTI is isolated from vibration via an air floatation table, its structure is large enough that low-frequency, high-amplitude vibrations could be present. However, in our case, vibration and turbulence effects were minimal and did not disrupt the phase-shifter calibration process. A number of vibration-tolerant phase-shifting solutions have been developed by other

researchers, including gathering four frames on four detectors, gathering four frames on one detector, random data acquisition and active vibration compensation [57].

Given our demonstration of the RBT and its limiting cases, we believe strongly that the technique is as effective and more easily implemented than other absolute calibration techniques such as the N-Position test, particularly for calibrating an instrument for micro-optics metrology. The N-position test requires accurate test part rotation about the test part center and this would be difficult to implement on a microscale. In contrast, random re-orientation of a small ball is not very difficult.

In future research, we anticipate the need to study the role of the NA more closely. The NA of the objective affects the solid angle of the measurement (the patch size) and a smaller NA will measure smaller patch sizes. For typical form errors on a ball surface where the largest form errors correspond to longer spatial wavelengths, this likely will cause the ball to behave as though it is of higher quality. Also, NA will affect the size of the measurement patch on the ball, which in turn would likely affect the convergence rate of the RBT to the system bias value.

Another subject of future study is how surface waviness and roughness affect a phase-shifting optical form measurement. Previous research has confirmed that these two frequency components will limit the accuracy of form measurements, but it would be interesting to quantify the effect for our type of system. We have seen how surface roughness (with its deep pits) can cause data dropout as light is not reflected back to the detector. Also, the contribution of x and y misalignment to the RBT remains to be investigated.

Overall, we believe that the techniques developed in this research assist manufacturers in identifying and collecting quantitative data on large and small test parts, both during and after the manufacturing process. This contribution to the development of new non-contact testing procedures will improve quality and reduce cost in industry. The continuous advancement of tools and concepts fueled by the demands of the marketplace require advances in faster and more accurate metrology. With growing options in terms of scanning speed, accuracy, and measurement size, manufacturers will be able to select a solution that is tailored to their needs.

CHAPTER 7: CONCLUSIONS

Lenses are probably the most widely used optical elements and micro-interferometry is the best approach for measuring many micro-refractives, however, the component size makes the measurements susceptible to systematic biases. Micro-refractive lenses are critical components in many devices, yet characterization remains challenging. Micro-interferometry is the best measurement approach and was pioneered in the mid 1990's by Schwider's group in Germany [58] and Hutley's group in the U.K. [59]. In micro-interferometry, interferometer biases can be of the same magnitude or greater than the deviations on the micro-lens under test; therefore, a rigorous calibration and estimated uncertainty is necessary. In simple terms, interferometer calibration means removing instrument wavefront biases before measuring a test piece, much like clearing out a calculator before beginning computations.

We have developed calibration methods for micro-interferometry to improve form error and reduce measurement uncertainty. Our ultimate goal was to contribute to the advancement of surface metrology for process control and quality assurance of the manufacture of high-end optical lenses. Much of this research is based on mathematical modeling, computer simulation, statistical estimation of measurements, while experimental techniques also play a major role.

Micro-lenses are discrete or array-based spheres, aspheres and other optics used in a wealth of applications, including focusing light into fibers for optical networking [60]. Despite advances in various metrology tools, interferometry remains the method of choice for measurements of optical surfaces, including refractive micro-lenses. There is also significant demand for fast and precise non-contact 3-D profile measurements in product design, industrial manufacturing, commercial multimedia, and information technology fields. Phase-shifting interferometers measure the surface height of very smooth, continuous surfaces with nanometer resolution.

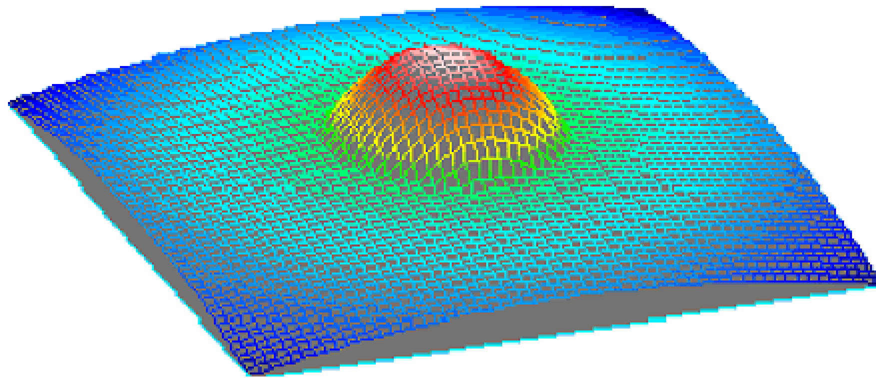

Figure 85. Result of an interferometric micro-lens height profile measurement [61].

With the goal of optimizing the micro-lens measurement calibration, we performed a rigorous study of the random ball test (RBT) in theory and practice. Our first conclusions are that the calibration result changes with calibration artifact surface quality and misalignment, and the effect worsens when testing micro-optics (radius less than 1 mm) due to retrace errors. Translational misalignment away from null, along the optical axis as small as 1/10 wave has a direct effect on the convergence of the calibration result, even when simulating a perfect spherical artifact. The curvature of the artifact

leads to retrace errors, which are aberrations caused by the specific path the rays take back through the interferometer following reflection from the test artifact.

The RBT self-calibration technique averages a series of surface subapertures on a medium quality micro-sphere to identify the interferometer biases that can later be subtracted from any individual measurement. By measuring a collection of random patches on the surface of a sphere, and then averaging the results, the contributions from the ball go to zero leaving only the systematic biases due to the instrument. Our spherical surface is inspected for surface form errors (deviation from the best-fit sphere) by making its center of curvature coincident with the focus of the objective lens. A self-centering element holder contains the spherical calibration artifact. An investigation into the dependence of test part radius and misalignment on micro-lens form-error-measuring interferometer wavefront bias data have been conducted both experimentally and by software simulation. A comprehensive geometric ray-trace software simulation was created to closely model the test arm of the physical system and this allowed us to study all factors impacting the calibration. Results clearly indicate that the retrace error increases with test lens surface curvature. The fact that retrace errors depend on the radius of the test part implies that when calibrating the instrument even with a perfect artifact, the calibration is nominally valid only when measuring parts with the same approximate radius as the calibration artifact.

As previously mentioned, the RBT is a random averaging technique applied to a collection of circular patches on the surface of a medium quality sphere that replaces the micro-lens under test. Each interferometric measurement of a patch contains information on the form error on the ball and also a bias due to the wavefront traveling through the

imperfect instrument. The basis for our simulation hinged on defining a sphere mathematically in terms of a set of spherical harmonic functions, and varying the amplitudes and the number of functions to adjust the form error on the sphere. Spherical harmonics indicate that the average of all the deviations on the surface of a ball (sphere) is zero; therefore the result of averaging many patches yields the wavefront bias due to our instrument, with some uncertainty related to the number and size (NA) of patches averaged. The RBT eliminates the need for an expensive high-quality concave calibration artifact, such as those used to calibrate commercial optical profilers. The RBT takes more time than calibration with a high-quality artifact, but reduces uncertainty compared with calibrating by a single measurement of a high-quality artifact. The biggest advantage of using RBT is overcoming a lack of availability of traditional high quality artifacts for a range of micro-lens ROC in accounting for retrace errors. It is much easier to buy a collection of balls of different radii.

Clearly, the RBT result will be different for every set of test conditions and we derived the following equation for the rms result of the RBT given z misalignment:

$$\sigma_{bias_estimate} = \sqrt{\left(\frac{\sigma_{ball}^2 + \sigma_{mis}^2}{N}\right) + \sigma_{bias_actual}^2} \quad (32)$$

We found that the rms result of the RBT depends on the rms of the form error of the calibration ball, the rms of the positional z-misalignment of the ball and the number of measurements taken. This relationship shows that fewer measurements are required if σ_{ball} and σ_{mis} are small. Based on the model, using the best quality ball surface and the least amount of misalignment (best null) will result in the need for fewer measurements to approach the best estimate of the system bias. Assuming that most purchasable

calibration balls will be of medium quality (as prescribed in the simulation), the data reveals that decreasing the ball misalignment from ½ to 1/10 wave, reduces the required number of measurements (*N*) by approximately one-third to achieve the same estimate. Furthermore, a systematic misalignment test can be applied to predict the residual rms wavefront bias of a simulated optical system, but more work is required before this can be applied in practice.

We validated the trends observed in the simulation by carrying out calibration procedures on our custom designed micro-interferomter, MORTI. MORTI stands for micro-optic reflection and transmission interferometer (MORTI) and is built from a Mitutoyo microscope body and fiber laser input. The flexible and compact micro-interferometer that can be used to measure form and transmitted wavefront errors, as well as radius of curvature. Following optical alignment of all components, the instrument is calibrated using the RBT. Results of the calibration indicating MORTI system bias were as good if not better when compared with other commercial interferometric instruments. Repeatability also compared well.

More and more, instrumentation is being sought to improve measurements of the conformity of parts to their tolerances and detect defects directly on the manufacturing line [62]. Metrology enables manufacturers to boost operating efficiencies and production yields gathering quantitative data on part defects, both during and following the manufacturing process. The shrinking of high-tech gadgets is ever-present, and as parts continue to shrink and become increasingly complicated, micro- and nano-metrology will take on a greater role [63, 64]. We believe that isolating systematic wavefront biases to achieve low-uncertainty surface form measurements will help

advance optical metrology, and will assist future efforts of other researchers in this field. Furthermore, self-calibration could be useful if applied to removing the discrepancies in other measurements such as transmission measurements of lens arrays, or even contact lenses.

REFERENCES

1. P.K. Rastogi, Editor*, Optical measurement techniques and applications*, Artech House, London, 10-23, 88-99, 341-342 (1997).

2. Suss Micro-Optics, http://www.suss-microoptics.com

3. Analog Devices Inc., http://www.analog.com

4. K. Iga, Y. Kokubun and M. Oikawa, *Fundamentals of Microoptics: Distributed-Index, Microlens, and Stacked Planar Optics*, Academic Press/Ohm, Tokyo, 1–3 (1984).

5. A.A. Bettiol, T. C. Sum, F.C. Cheong, C.H. Sow, S. Venugopal Rao, J.A. van Kan, E.J. Teo, K. Ansari, F. Watt, "A progress review of proton beam writing applications in microphotonics," *Nuclear Instruments and Methods in Physics Research* **B** 231, 364–371 (2005).

6. J. D. Briers, "Interferometric optical testing: an interlaboratory comparison," *Journal of Optics A: Pure & Applied Optics* **1** 1, 1–14 (1999).

7. P. E. Murphy, T. G. Brown and D. T. Moore, "Measurement and calibration of interferometric imaging aberrations," *Appl. Opt.* **39**, 6421–6429 (2000).

8. Frije University Belgium, http://www.vub.ac.be/english

9. Robert Smythe, "Measure for measure," *SPIE's Oemagazine*, 34–36 (2004).

10. Marc Tricard, Greg Forbes and Paul Murphy, "Subaperture metrology technologies extend capabilities in optics manufacturing," in Optical Fabrication, Testing, and Metrology II, *Proc. SPIE* **5965**, A. Duparre, R. Geyl, L. Wang, Eds., 100–110 (2005).

11. C. Evans and R. Kestner, "Test optics error removal," *Appl. Opt.* **35**, 1015–1021 (1996).

12. B. F. Oreb, D. I. Farrant, C. J. Walsh, G. Forbes and P. S. Fairman, "Calibration of a 300-mm-aperture phase-shifting fizeau interferometer," *Appl. Opt.* **39**, 5161–5171 (2000).

13. D. J. Whitehouse, "Some theoretical aspects of error separation techniques in surface metrology," *J. Phys.* **E** 9, 531–536 (1976).

14. Paul E. Murphy, Jon Fleig, Greg Forbes and Paul Dumas, "Novel method for computing reference wave error in optical surface metrology," in Optifab 2003,

Proc. SPIE **TD02**, W. C. Czajkowski, T. Dohi, H. Lauth, H. M. Pollicove, Eds., 138–140 (2003).

15. A. E. Jensen, "Absolute calibration method for Twyman-Green wavefront testing interferometers," *J. Opt. Soc. Am.* **63**, 1313A (1973).

16. D. J. Whitehouse, *Handbook of Surface and Nanometrology*, Institute of Physics, 1–26 (2003).

17. J. Schwider and O. Falkenstörfer, "Twyman-Green interferometer for testing microspheres," *Opt. Eng.* **34**, 2972–2975 (1995).

18. Taylor Hobson Ltd., http://www.taylor-hobson.com

19. D.J. Whitehouse, *Surfaces and Their Measurement*, Hermes Penton Ltd., London, 187–215 (2002).

20. Wei Gao, Xue-Feng Qiang and Satoshi Kiyono, “Self-calibration of lateral non-linearities of an optical interference microscope,” *Measurement* **34** 3, 245–253 (2003).

21. P. Hariharan, *Optical Interferometry*, 2nd ed., Academic Press, San Diego, USA, 11–17 (2003).

22. E. Hecht, *Optics*, 4th ed., Addison-Wesley Publishing Co., San Francisco, CA, USA, 281–320, 385–438 (2002).

23. Wikipedia, “Interference,” http://en.wikipedia.org

24. James Millerd, Neal Brock, John Hayes, Brad Kimbrough, Michael North-Morris and James Wyant, “Vibration insensitive interferometry,” in ICSO Sixth International Conference on Space Optics (2006).

25. J. E. Greivenkamp and J. H. Bruning, "Phase shifting interferometers," in *Optical Shop Testing*, 2nd ed., D. Malacara, Ed., Wiley & Sons, New York, 501–598 (1992).

26. Y.-Y. Cheng, and J. C. Wyant, "Phase-shifter calibration in phase-shifting interferometry," *App. Opt.* **24**, 3049–3052 (1985).

27. http://www.answers.com

28. Michael A. Gauvin and Edward R. Freniere, “Reducing stray light in opto-mechanical systems,” Lambda Research Corporation, http://boojum.as.arizona.edu/~jill

29. Takashi Kaneko, Atsushi Yamamoto, Takaharu Idogaki and Tadashi Hattori, “Dynamic focusing lens for expanding depth of focus of optical microscope,” in 7th International Symposium on Micro Machine and Human Science (1996).

30. John Taylor, *An introduction to error anaylsis: the study of uncertainties in physical measurements*, 2nd ed., University Science Books, Sausalito, CA, USA, 121–148, (1997).

31. Southeastern Louisiana University – Physics Department, http://www.phys.selu.edu

32. R. E. Parks, C. J. Evans and L. Shao, “Calibration of interferometer transmission spheres,” in Optical Fabrication and Testing Workshop, *OSA Technical Digest Series* **12**, 80–83 (1998).

33. M. Raugh, “Absolute two-dimensional sub-micron metrology for electron beam lithography: A theory of calibration with applications,” *Precision Engineering* 7 1, 3–13 (1985).

34. N. Gardner and A. Davies, “Self-calibration for microrefractive lens measurements,” *Opt. Eng.* **45** 3, 033603 (2006).

35. James C. Wyant, “Zernike polynomials and phase-shifting interferometry,” http://wyant.optics.arizona.edu

36. Wikipedia, "Spherical aberration," http://en.wikipedia.org

37. Melles Griot Inc., http://www.mellesgriot.com

38. Wikipedia, “Coma (optics),” http://en.wikipedia.org

39. http://www.photonics.com

40. Wikipedia, "Aberration in optical systems," http://en.wikipedia.org

41. Mark Chapman, “Heterodyne and homodyne interferometry,” Renishaw plc., http://www.renishaw.com

42. Angela D. Davies and Brent C. Bergner, “Improving metrology for micro-optics manufacturing,” in 48th Ann. Int. Symp. on Optical Science and Technology, Gradient Index, Miniature, and Diffractive Optical Systems III, *Proc. SPIE* **5177**, 67–81 (2003).

43. Neil Gardner and Angela Davies, “Retrace error evaluation on a figure-measuring interferometer,” Proceedings of the SPIE 50th Annual International Symposium

on Optics and Photonics, Optical Manufacturing and Testing VI Conference, San Diego, August (2005).

44. D. Griffith, “How to talk to ZEMAX from MATLAB,” http://www.ZEMAX.com

45. Mathworks Inc., “Dynamic Data Exchange,” http://www.mathworks.com

46. G. B. Arfken and H. J. Weber, *Mathematical Methods for Physicists*, 5th ed., Academic Press, New York, 771–807 (1985).

47. E. W. Weisstein, “Spherical Harmonics,” http://mathworld.wolfram.com

48. J. E. Marsden and A. J. Tromba, *Vector Calculus*, 2nd ed., W. H. Freeman and Company, New York, 40–60 (1981).

49. TALtech Instrumental Software Solutions, http://www.taltech.com

50. John D’Errico, “Consolidator,” http://www.mathworks.com

51. K. Creath and J. C. Wyant, “Absolute measurement of surface roughness,” *Appl. Opt.* **29**, 3823–3827 (1990).

52. Bal-tec, http://www.precisionballs.com

53. Micralenses™, http://www.micralyne.com

54. Angela Davies, private communication

55. Ulf Griesmann, Quandou Wang, Johannes Soons and Remi Carakos, “A simple ball averager for reference sphere calibrations,” in Optical Manufacturing and Testing VI, *Proc. SPIE* **5869**, H. Philip Stahl, Ed., 189-196 (2005).

56. MicroLUPI 2000, http://www.omnitek.com.br

57. J. Hayes, "Dynamic interferometry handles vibration," in *Laser Focus World*, 109-113 (2002).

58. H. Sickinger, J. Schwider, and B. Manzke, "Fiber based Mach-Zehnder interferometer for measuring wave aberrations of microlenses," *Optik* **110**, 239–243 (1999).

59. M. C. Hutley, “Refractive lenslet arrays,” in *Micro-Optics: Elements, Systems, and Applications*, H. P. Herzig, Ed., Taylor and Francis, Philadelphia, 127–152 (1998).

60. Tsuguo Kohno, Takanori Yazawa, Daigo Saito and Shinichi Kohno, "Figure error control for diamond turning by in-process measurement," *Precision Engineering* **29**, 391–395 (2005).

61. T. Peschel, "Production of polymer microlenses and arrays by the piezo pressure head procedure," http://www.microoptical-systems.com

62. Mike Richman, "The future of metrology," Quality Digest, http://www.qualitydigest.com/may05/articles/04_article.shtml

63. Joseph M. Geary, Marty Yoo and Guojun Si, "Retrace error: a case study," in Interferometry: Surface Characterization and Testing, *Proc. SPIE* **1776**, Katherine Creath, John E. Greivenkamp, Eds., 98–105 (1992).

64. Sung-Keun Lee, Kwang-Cheol Lee and Seung S Lee, "A simple method for microlens fabrication by the modified LIGA process," *J. Micromech. Microeng.* **12**, 334–340 (2002).

APPENDIX

The following pages contain the detailed MATLAB code generated for simulating the random ball test.

```
%Create a sphere with low-frequency surface form errors using
%spherical harmonic functions. Randomly re-orient the sphere and pick
%a random patch. Remove a best-fit sphere from the data to isolate form
%errors only. Describe sag data for the patch and send to Zemax.

 clear all
 close all

 %time start
 TIC
 %Initiate Link
 zDDEInit
 %Define matrix sizes
 zavg = zeros(128);
 W = zeros(128);
 psum = zeros(128);
 %name = num2str(N);
 %eval(['p' name ' = zeros(128);'])

%%%%%%%%%%%%%%%%%%%%%%%%%%%%%%%%%%%%%%%%%%%%%%%%%%%%%%%%%%%%%%%%%%%%%%%

 %Number of patches to pick and send to Zemax in a loop
  N = 1;
 %Define sphere base size
  R = 25;
 %Define IRREGULAR SPHERE harmonic parameters & multiplication constant
  degree = 6;
  order = 1;
  M = .008;  %used for ref sphere too
 %Define grid sizes
  sg = 201; %spherical coordinate grid (should be denser than gg)
  gg = 101; %griddata grid...MUST ALSO CHANGE line 327

%%%%%%%%%%%%%%%%%%%%%%%%%%%%%%%%%%%%%%%%%%%%%%%%%%%%%%%%%%%%%%%%%%%%%%%

for i=1:N

wW = zeros(128);

% Create a grid in spherical coordinates
delta = pi/(sg-1);
theta = 0 : delta : pi; % altitude
phi = 0 : 2*delta : 2*pi; % azimuth
[phi,theta] = meshgrid(phi,theta);
```

```
% Calculate the harmonic functions
Ymn = legendre(degree,cos(theta(:,1)));
Ymn = Ymn(order+1,:)';
yy = Ymn;
for kk = 2: size(theta,1)
    yy = [yy Ymn];
end;
yy = yy.*cos(order*phi);
order = max(max(abs(yy)));
rho = R + M*yy/order;

% Apply spherical coordinate equations
r = rho.*sin(theta);
x = r.*cos(phi);
y = r.*sin(phi);
z = rho.*cos(theta);
%v = x.^2 + y.^2 + z.^2;

%% Rotate sphere to new random angle
alpha = rand*pi;
beta = rand*pi;
gamma = rand*pi;

% define the rotation matrix
a = [1 0 0;0 cos(alpha) sin(alpha);0 -sin(alpha) cos(alpha)]*[cos(beta)
0 -sin(beta);0 1 0;sin(beta) 0 cos(beta)]*[cos(gamma) sin(gamma) 0;-
sin(gamma) cos(gamma) 0;0 0 1];

for i=1:sg
  for j=1:sg
  a = [a(1,1) a(1,2) a(1,3);a(2,1) a(2,2) a(2,3);a(3,1) a(3,2) a(3,3)];
% result of above long equation
  b = [x(i,j);y(i,j);z(i,j)]; % want to rotate all x's, y's and z's
        A = a*b; % do the rotation of every (x,y,z) point
        x(i,j) = A(1,1);
        y(i,j) = A(2,1);
        z(i,j) = A(3,1);
  end
end

% Exclude data
maxz = 0.564112 * R;
nodata = find(z <= maxz); %finds indices where z <= maxz
z(nodata) = 0.564112 * R;  %uses those indices
x(nodata) = 0.564112*R;
y(nodata) = 0.564112*R;
C = min(z);
B = sort(C);
d = max(B);
z = z - d;
z(isnan(z)) = 0;

%------------------------------------------------------------------
```

```
%Use griddata to change to a uniform grid

% Fit data to an evenly spaced Cartesian grid to prepare it for
exporting to Zemax
xprime = x';
yprime = y';
zprime = z';
newx = xprime(:);
newy = yprime(:);
newz = zprime(:);
[XI YI] = meshgrid(-R:((2*R)/(gg-1)):R, -R:((2*R)/(gg-1)):R);
%[newxnewy,newz] =
consolidator11d([newx(:),newy(:)],newz(:),'mean',1.e-12);
%newx=newxnewy(:,1);
%newy=newxnewy(:,2);
ZI = griddata(newx,newy,newz,XI,YI);
ZI(isnan(ZI)) = 0;

%------------------------------------------------------------------
% Create a reference sphere

%Define REFERENCE SPHERE harmonic function parameters
 degree = 1;
 order = 0;

deltar = pi/(sg-1);
thetar = 0 : deltar : pi; % altitude
phir = 0 : 2*deltar : 2*pi; % azimuth
[phir,thetar] = meshgrid(phir,thetar);

% Calculate the harmonic functions
Ymnr = legendre(degree,cos(theta(:,1)));
Ymnr = Ymnr(order+1,:)';
yyr = Ymnr;
for kkr = 2: size(thetar,1)
    yyr = [yyr Ymnr];
end;
yyr = yyr.*cos(order*phir);
order = max(max(abs(yyr)));
rhor = R + M*yyr/order;

% Apply spherical coordinate equations
rr = rhor.*sin(theta);
xr = rr.*cos(phi);
yr = rr.*sin(phi);
zr = rhor.*cos(theta);
%v = x.^2 + y.^2 + z.^2;

% Exclude data
maxzr = 0.564112 * R;
nodata = find(zr <= maxzr); %finds indices where z <= maxz
zr(nodata) = 0.564112 * R;  %uses those indices
xr(nodata) = 0.564112*R;
yr(nodata) = 0.564112*R;
C = min(zr);
```

```
B = sort(C);
d = max(B);
zr = zr - d;
zr(isnan(zr)) = 0;

%-----------------------------------------
%Again, use griddata to change to a uniform grid

% Fit data to an evenly spaced Cartesian grid to prepare it for
exporting to Zemax
xrprime = xr';
yrprime = yr';
zrprime = zr';
newxr = xrprime(:);
newyr = yrprime(:);
newzr = zrprime(:);
[XIr YIr] = meshgrid(-R:((2*R)/(gg-1)):R, -R:((2*R)/(gg-1)):R);
%[newxnewy,newz] =
consolidator11d([newx(:),newy(:)],newz(:),'mean',1.e-12);
%newx=newxnewy(:,1);
%newy=newxnewy(:,2);
ZIr = griddata(newxr,newyr,newzr,XIr,YIr);
ZIr(isnan(ZIr)) = 0;

zfinal = ZIr - ZI;
%zfinal = -ZI;
%zfinal = zeros(501);
%clf
%figure
%surf(XIr,YIr,zfinal)
%shading interp
%axis equal
%light
%lighting phong
%view(-126,36)
%rotate3d
%titstr5 = ['best fit sphere removed'];
%title(titstr5)

%---------------------------------------------------
% Write gridsag file, then send to zemax
% Write to ASCII file (.dat)
%

% STEP 1. Open file, or create new file, for writing; discard existing
contents, if any
fid = fopen('C:\Program Files\ZEMAX\Samples\NEWgridSAGform.DAT','wt');

% STEP 2. Write to the file: 1st, write seven values for the header
line, then enter down to next line
% fprintf(fid,'401 401 0.125 0.125 0 0 0\n') % Width/pts = 10/100 = 0.1
   fprintf(fid,'201 201 0.25 0.25 0 0 0\n')

% STEP 3. Write all remaining entries (nx*ny)
   %for iii = 1:size(zfinal,1)
```

```
    %   for jjj = 1:size(zfinal,2)
     %    fprintf(fid,'%f %f %f %f
0\n',zfinal(iii,jjj));%,dzdx(iii,jjj),-dzdy(iii,jjj),-
d2zdydx(iii,jjj));
     % end
     %end
%    fprintf(fid,'%f 0 0 0 0\n',z);

% STEP 3. Write all remaining entries (nx*ny)
  fprintf(fid,'%7.4f 0 0 0\n',zfinal); %7.4

% STEP 4. Close the file
   status = fclose(fid);

% DDE Commands   (don't forget to open Zemax !!!!!!!!!!!!!!!!!!!!)
%

% Initiate Link
  %zDDEInit
  %zSetSurfaceData(4, 52, 5)
  %zPushLens(10)

%% Create random misalignment of the gridsag surface (max 1/2 wave)

   %rz = rand;
   %g = -0.003;
   %h = 0.003;
   %distz = 19 + g + (h-g)*rz;  %defocus; %distance from objective lens
to surface

   dx = 0;
   dy = 0;
   distz = 30;

% Send grid data to Zemax
  zImportExtraData(4, 'C:\Program
Files\ZEMAX\Samples\NEWgridSAGform.DAT')
% Send the misalignment
  zSetSurfaceData(4, 52, dx)    % Can also use zGetSurfaceData to check
  zSetSurfaceData(4, 53, dy)
  zSetSurfaceData(3, 3, distz)

  zPushLens(10)

% User Input
%u = input(' Acceptable? Y/N [Y] : ','s');
%if isempty(u)
%    u = 'Y';
%else
%    u = 'N';
%end
%if u == 'Y';
%----------------------------------------------------------------------
---------------------------
```

```
% Send data back to Matlab, after all N maps have returned to Matlab,
Average the data
% Make text file from wavefront map
  zGetTextFile('file2','Wfm','FOO.cfg',0)
% Read text file into Matlab and put data in a matrix called p
  % ReadZemaxWaveMap('C:Documents and Settings\Neil
Gardner\Desktop\Project\Zemax\file1')
  wm = ReadZemaxWaveMap('C:\Program Files\ZEMAX\Samples\file2');
% Gather wavefront data in matlab, and average

%A = wm.data;
wW = wm.data;
W = W + wW;
%name = num2str(i);
%eval(['p' name ' = A - zcalib;'])
%eval(['p' name ' = A;'])
%psum = psum + wm.data;
end

if u == 'N';
    N = N-1;
end

end

%for i=1:N
%name = num2str(i);
%eval(['psum = psum + p' name ';'])
%end

zavg = W./N;
%zavg = psum./N;
%zavg = zavg - zcalib;

%--------------------
% Estimate Zernikes

%zfinal = mask_circle(zfinal,[33,33],31); % mask (matrix,center,radius)
zavg = mask_circle(zavg,[65,65],62); % mask (matrix,center,radius)
vsize = size(zavg);
[mr,ma] = zern_radius_angle(vsize,[65,62],62);
[zernparameters,rmserror,standarddevs,tstatistics,probabilities] =
zern_estim(zavg,mr,ma,[1:36]);

[x_vect,y_vect]=get_xy(zavg,1);
% Zernike terms Removal
zavg=rmterms(x_vect,y_vect,zavg,[0 0 0 0 0],36);
% 5 zernike terms in bracket:   [tilt power astig coma spherical]

vsize = size(zavg);
[mr,ma] = zern_radius_angle(vsize,[65,65],62);
[zernparameters,rmserror,standarddevs,tstatistics,probabilities] =
zern_estim(zavg,mr,ma,[1:36])

%off = offset/N
```

```
a = max(zavg);
b = sort(a);
pk = max(b);
c = min(zavg);
d = sort(c);
val = min(d);
pktoval = pk - val;
%RMS
%zavg(isnan(zavg)) = 0;
B = zavg;
B = B(finite(B));
rms = sqrt(mean(B.^2));

%figure
pcolor(zavg)
%colormap(gray)
axis equal
shading interp
colorbar('vert')
%c=camlight

titlenum3 = num2str(rms);
titlenum4 = num2str(pktoval);
titlenum = num2str(N);
%titlenum2 = num2str(NA);
titstr6 = ['RBT Avg of ' titlenum ' wavefront maps, PV = ' titlenum4 '
wvs, RMS = ' titlenum3 ' wvs', ];
%titstr = ['RBT Average of ' titlenum ' wavefront maps of a perfect
sphere, NA = ' titlenum2 ' , waves'];
title(titstr6)


TOC
```